A CRYOGENIC DETECTOR
FOR SUBMILLIMETRE ASTRONOMY

BRADLEY GUSTAV GOM

B. Sc. Physics, University of Lethbridge, 1997

A Thesis
Submitted to the Council on Graduate Studies
of the University of Lethbridge
in Partial Fulfilment of the
Requirements for the Degree

MASTER OF SCIENCE

LETHBRIDGE, ALBERTA
MARCH, 1999

Abstract

Over the last several years, a submillimetre astronomical polarizing Fourier Transform Spectrometer (FTS) has been developed for use at the James Clerk Maxwell Telescope (JCMT) located atop Mauna Kea, Hawaii. A new liquid ^{3}He cooled dual polarization detector system has been carefully designed for use with this FTS to eliminate noise problems encountered with UKT14, the JCMT facility bolometric detector.

The objective of this thesis is to evaluate and optimize the performance of the new detector system. The design of the detector system is discussed, and the noise performance of the system is evaluated. The system performance is determined from photometric, classical V-I, and spectroscopic measurements.

Compared to UKT14, the intrinsic bolometer noise is reduced by a factor of ~ 2. More importantly, the *spectral* signal to noise ratio is improved by a factor of ~ 10 due to the elimination of electrical pickup and microphonic noise in the detector signal.

Acknowledgements

Naturally, I thank David for providing me the opportunity of undertaking this project, and for his enthusiasm and interest along the way. There are several people who must also be acknowledged for their assistance during the various stages of this project:

Technical Support Crew:

Prof. Alan Clark -for the much appreciated help during the observing runs.

Greg Tompkins -for technical support during and after the data collection, and for creating a certain element of mystery during the cryogen cycling test runs.

Academic Support:

Dr. Wayne Holland -for his generous assistance on and off the telescope, and for answering the questions of a neophyte.

Prof. Peter Ade -who is responsible for creating most of nifty components in the detector, and who is a definitive source of knowledge on the topic of bolometers.

Financial and Logistical Support:

NSERC and NRC -which provided grant money so that I could eat, and so that I could fly to Hawaii. Without the funding from these agencies, I would not have been able to ever see the detector in person.

The JCMT is operated by the Observatories, on behalf of the U. K. Particle Physics and Astronomy Research Council, the Netherlands Organisation for Pure Research, and the National Research Council of Canada.

Table of Contents

List of Tables

List of Figures

List of Abbreviations

Abbreviations used in this thesis are explained where they are first encountered in the text, and are listed below for clarity.

EMI : Electro-Magnetic Interference; a noise voltage induced in the detector signal by external electromagnetic fields.

FTS : Fourier Transform Spectrometer. The specific spectrometer used with this detector system is the one described by Naylor et. al., "Polarizing Fourier transform spectrometer for astronomical spectroscopy at submillimeter and mid-infrared wavelengths", *Proc. SPIE*, **2198**, 703-714, 1994.

IDL : Interactive Data Language; the high level graphical programming language used for writing the analysis code necessary for this thesis. Distributed by Research Systems, Inc., 4990 Pearl East Circle, Boulder, Colorado, 80301, USA.

JCMT : The James Clerk Maxwell Telescope on Mauna Kea, where the detector system currently resides. Joint Astronomy Centre, 660 North A'ohoku Place, University Park, Hilo, Hawaii, 96720, USA.

JFET : Junction Field Effect Transistor, used for their low intrinsic noise levels and extremely large input impedance.

NEP : The Noise Equivalent Power of a detector, defined to be the root mean square incident radiant power level required to produce a detector signal with a signal to noise ratio of unity in a one second integration.

QMW : Queen Mary and Westfield College, University of London, Mile End Road, London, E1 4NS, UK. The initial design and construction of the detector system was performed in cooperation with Dr. Peter Ade at the QMW.

RFI : Radio Frequency Interference; a noise voltage induced in the detector signal by external high frequency electromagnetic fields.

S/N : The Signal-to-Noise ratio, defined as the root mean square detector signal divided by the root mean square detector noise level, in a one second integration.

V-I : Refers to the Voltage-Current characteristics of an electronic device. For a bolometer, the behaviour of the detector voltage as a function of bias current is used to characterize the bolometer performance.

Chapter 1
Introduction

1.1 Basic Astronomy

While astronomical imaging tells us about the morphology of the universe, modern astrophysics owes its existence to spectroscopy, in the sense that the bulk of our current knowledge of the composition and physical properties of the universe can only be determined from spectroscopic observations. Spectra tell us about the identity and physical state of the constituent atoms, molecules and ions (both atomic and molecular) in astronomical sources ranging from planetary atmospheres to the interstellar medium, and also about the dynamics of large scale systems such as galaxies.

Until the middle of this century, only the region of the electromagnetic spectrum between the near-ultraviolet and near-infrared was accessible to astronomers. Observations at wavelengths longer than the near-infrared were not feasible due in part to the attenuating nature of the earth's atmosphere at these wavelengths, and in part to the lack of detectors sensitive to long wavelength radiation. The advent of microwave and radar technologies, developed during the second world war, opened up a new window for radio astronomy in the millimetre to metre wavelength range. This region is rich in spectral lines from the rotational transitions of various molecular species, and fine structure atomic and ionic transitions. In addition, the blackbody radiation from interstellar dust in star forming regions, the synchrotron radiation from galactic cores and supernovae remnants, and the peak of the blackbody spectrum from the cosmic microwave background (CMB), can also be detected in this region.

The most recent advances in infrared astronomy have come from observations made in the submillimetre wavelength range, which is roughly between 0.3 and 1 millimetre. As a result of the high degree of technical difficulty involved in observing at these wavelengths, which is due in part to the complex instrumentation that pushes the limits of both optical and microwave technologies, and in part to the partial and variable transmission of the atmosphere, this region has become the last frontier in ground-based observational astronomy. The principal atmospheric absorber at these wavelengths is water vapour. Since water vapour has many strong absorption lines in the submillimetre region, there are only a few useful atmospheric transmission windows, even for high altitude telescopes. The main atmospheric windows of interest are centred at roughly 350, 450, 600, 750, 850, and 1300 μm. The shorter wavelength windows are

particularly sensitive to fluctuations in atmospheric water vapour abundance, and are therefore the most challenging for astronomical observations.

In the last two decades, large telescopes have been built specifically for millimetre-submillimetre astronomy. These telescopes, such as the 15 metre James Clerk Maxwell Telescope (JCMT) and the 10.4 metre Caltech Submillimetre Observatory (CSO) on Mauna Kea, Hawaii, are located at dry, high altitude sites in order to minimize the attenuation by the atmosphere. The recent development of powerful submillimetre telescopes has been complemented by advances in instrumentation and detector technology.

1.2 Spectroscopic Instruments

Detectors used for far-infrared spectroscopy can be classified as either coherent or incoherent detectors. Coherent detectors make use of heterodyne technology that was first developed for radio and microwave applications. In this type of detector, the incident radiation is mixed with that from a local oscillator. The combined signal (the intermediate frequency, or IF) is then detected with a nonlinear detector, usually a diode. The IF signal is in the radio frequency range, and can be filtered, amplified, and spectroscopically analysed using existing radio techniques. Heterodyne detectors have very high resolving powers ($\lambda/\Delta\lambda \geq 10^6$), but suffer from narrow bandwidth since they use waveguides and cavities that, once built, cannot be readily tuned over a large frequency range.

Unlike heterodyne detectors, incoherent detectors are essentially energy detectors that do not, by themselves, preserve any information about the frequency or phase of the incident radiation. As a result, spectroscopic measurements require some means of encoding the spectral information in the incident radiation before it reaches the detector. This spectral encoding is typically performed by an interferometer, where phase changes are introduced between separate beams of the incident radiation in order to create interference, which is then recorded by the detector and decoded to reconstruct the source spectrum. The details of the process depend on the type of interferometer used.

The most popular interferometer for far-infrared spectroscopy is the Fourier Transform Spectrometer (FTS), classically known as the Michelson interferometer. A schematic of a basic FTS is shown in Figure 1.1. The radiation from the source is collimated by a lens, L_1, and passes through a beam splitter. Half of the incident radiation (the reflected beam) is thereby directed to a fixed mirror, which reflects the radiation back

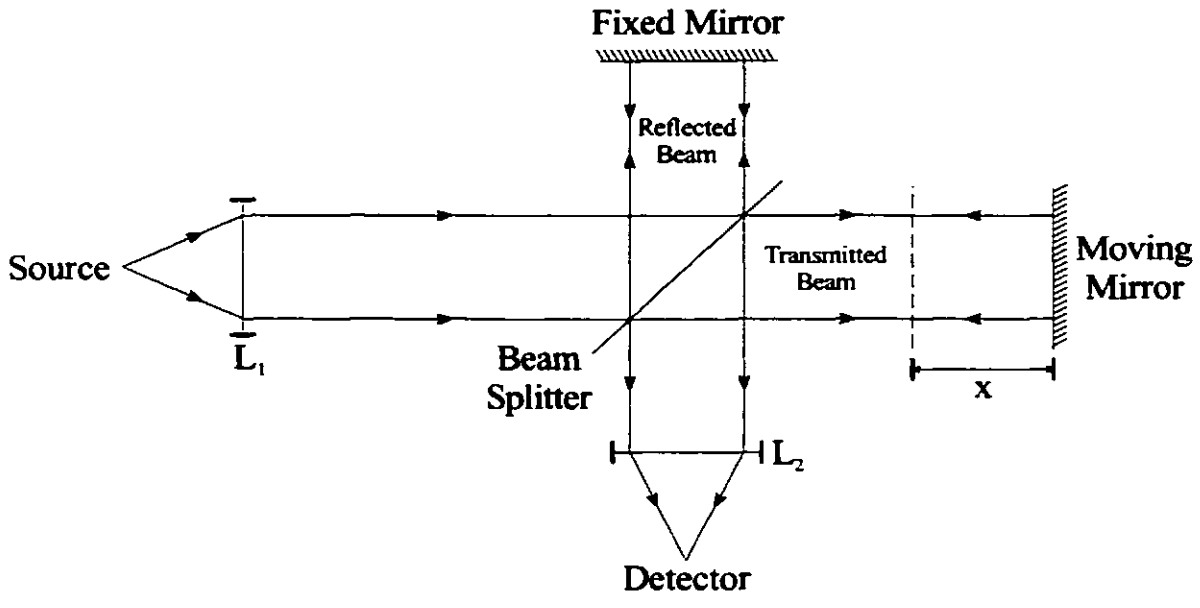

Figure 1.1 : Optical schematic of a simplified Fourier transform spectrometer.

through the beam splitter and through another lens, L_2, which focuses the radiation (1/4 of the incident radiation) onto the detector. The other half of the incident radiation (the transmitted beam) passes through the beam splitter to a moving mirror, is reflected back to the beam splitter, partially reflected (1/4 of the incident radiation) to L_2 and focussed onto the detector. The two beams interfere with each other constructively or destructively according to the difference in optical path length and the intensities of the various frequency components emitted by the source. For example, when the moving mirror is positioned at x = 0, the path lengths travelled by the reflected and transmitted beams are identical, and there will be maximum constructive interference. As the moving mirror is displaced by a distance x, the path travelled by the transmitted beam is made longer than that of the reflected beam by 2x. The signal recorded as the path difference between the transmitted and reflected beams is varied is referred to as an interferogram, and represents the Fourier cosine transform of the spectrum of the source. The source spectrum is reconstructed mathematically by calculating the inverse Fourier transform of the interferogram. A polarizing FTS uses the same principles, but the optics are more complicated since they provide polarization encoding of the incident radiation.

1.3 Incoherent Detectors

Incoherent detectors can be classified as either quantum (photon) or thermal detectors. Quantum detectors make use of the change in electrical current flowing through a photoconductor as incident photons raise electrons into the conduction band. This type of detector can detect individual photons if the photon energy is larger than the band gap energy of the semiconductor crystal, which is referred to as the photoelectric threshold. The photoelectric threshold of current photoconductors limits their use to wavelengths shorter than ~ 200 μm [1]. Thermal detectors, on the other hand, measure the change in resistance of a thermistor in response to heating from absorbed radiation. Thermal detectors are known more specifically as bolometers (from the Greek *bole*, meaning ray), and are sensitive to any radiation that can be absorbed by the detecting element and converted to heat.

Bolometers can be made of any material having a resistivity that changes as a function of temperature. While historically, metal films and carbon chips were used, modern bolometers are typically constructed from semiconductors doped with various elements in order to produce the desired temperature coefficient of resistance at the desired operating temperature. Typical examples are Ge:In:Sb and Ge:Ga, which have resistivities that are strong functions of temperature, and are usually operated at temperatures of 0.3 K or below.

Three primary factors must be considered in the design of a bolometric detector for use with a FTS: Firstly, the total power falling on the bolometer (from the signal and background) affects the sensitivity of the detector, so care must be taken in the optical design to minimize background power loading, while maximizing the coupling efficiency to the source. Secondly, a FTS that produces an interferogram in a time, t, produces a modulated signal with a frequency that is inversely proportional to t. Typically, the FTS scan time is selected to produce a modulation frequency faster than the highest frequency fluctuations in atmospheric transmission, which are in the order of ~ 10 Hz. Therefore, the detector frequency response must be fast enough to accommodate the signal modulation frequencies between approximately 10 and 100 Hz. Finally, the intrinsic noise produced by a bolometer element decreases with operating temperature, so the bolometer must be operated at the coldest temperature that is practical to maintain, usually in the 0.3 to 0.1 K range.

The fundamental limit to the noise performance of a detector is the statistical noise produced by quantum fluctuations in the incident radiation. The theory describing this background photon noise is presented in Chapter 5, although we use the results here. Since photon noise occurs naturally in radiation from any blackbody source, the background photon noise level is defined by the sum of the contributions from each emitting element between the source and the detector, added in quadrature. The atmosphere and telescope, therefore, both contribute to the total photon noise, since they are blackbody (or more precisely, greybody) sources with given temperatures and emissivities. Figure 1.2 shows the background photon noise equivalent power (NEP) falling on the bolometer element, calculated as a function of astronomical source temperature and atmospheric water vapour abundance, in units of millimetres precipitable water vapour (PWV), for the 450 μm transmission window. The data in the figure include the photon NEP from the source, atmosphere, and the telescope primary mirror, each of which are modelled as blackbody radiators of specific temperature and emissivity. The full radiative transfer of the photon NEP was calculated using the transmission efficiencies of the atmosphere (as a function of water vapour abundance) and telescope (~ 90 %), and the throughput of the 15 m, f/35 JCMT. It can be seen in the figure that the atmospheric photon noise dominates when the water vapour abundance is greater than ~ 2 mm PWV. As the column abundance of water vapour in the atmosphere increases, the signal (and photon noise) from the source is attenuated, and the emission (and photon noise) from the atmosphere increases. It must be recognized that this increase in photon NEP with water vapour content is accompanied by a large decrease in the signal-to-noise ratio, due to the attenuation of

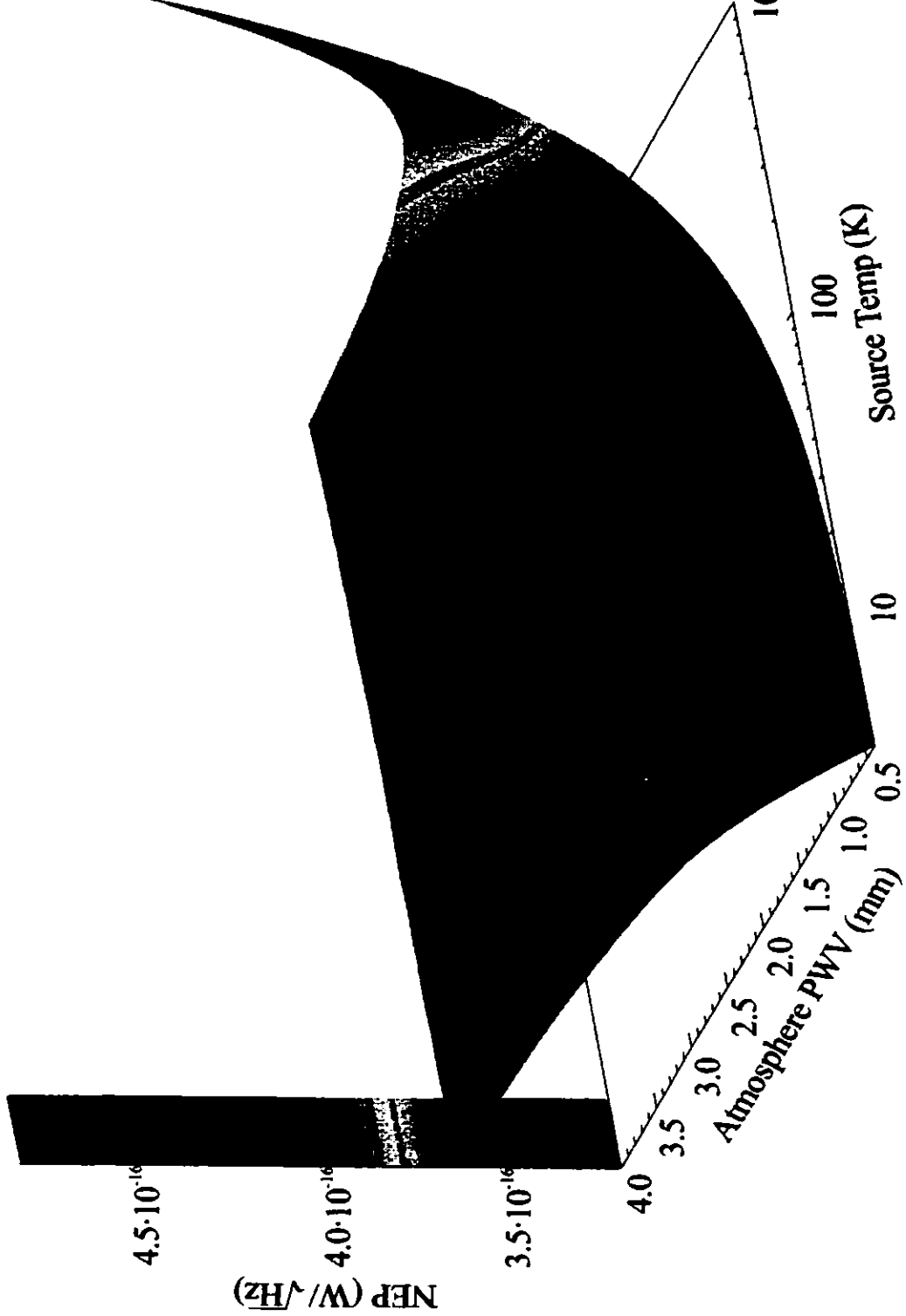

Figure 1.2 : Total photon NEP produced by an astronomical source, the atmosphere, and the telescope primary mirror, as a function of source temperature and atmospheric precipitable water vapour level (PWV), calculated for the 450 μm window.

source signal, and observations can only be made when the atmospheric water vapour levels are below ~ 0.5 mm PWV. The total photon NEP represents the lowest possible noise level that can be achieved by a detector, since this source of noise is signal related and cannot be eliminated. An ideal detector will have low enough intrinsic noise to allow background photon noise limited operation.

Prior to 1997, broadband submillimetre spectroscopy at the JCMT was performed using the facility bolometric detector, UKT14. The UKT14 system was designed for photometric observations, and uses a pumped ^{3}He cooled, Ge:In:Sb composite bolometer. While the intrinsic sensitivity and noise performance of UKT14 is adequate for photometric measurements, the intrinsic NEP of ~ 10^{-15} $W/\sqrt{Hz}$ is significantly higher than the photon noise limit (see Figure 1.2). The UKT14 system was also found to exhibit excessive microphonic sensitivity and electrical pickup, which makes it unsuitable for use with a high resolution FTS.

This thesis describes the construction, performance, and optimization of a liquid ^{3}He cooled, dual polarization, Ge:Ga, composite bolometer detector system designed specifically for use with a high resolution polarizing FTS. Considerable care was taken during the design of the detector system to overcome the problems encountered with UKT14. It is shown that the detector succeeds in outperforming its predecessor, and is currently the best detector of its type in use on a ground based telescope. Minimum NEPs of ~ $4 \cdot 10^{-16}$ $W/\sqrt{Hz}$ are measured, which represent nearly photon noise limited performance. In Chapter 2, the construction of the composite bolometer units, and the theory of the electrothermal behaviour of these bolometers is presented. In Chapter 3, the general design of the integrated detector system, and the novel differential electronics system that essentially eliminates electrical pickup in the detector signal is discussed. Chapter 4 contains a description of the closed-cycle cryogenic system that enables the detector to be easily and reliably cooled to its operating temperature of 0.3 K. The control software is also presented in this chapter, which was written to provide automated operation of the cryogenic cooling cycle. Chapter 5 contains the main focus of the thesis: the analysis of the system test results, collected during observing runs in May of 1997 and 1998. A summary of the system performance is given at the end of Chapter 5. Finally, a software appendix is included after Chapter 5 that contains the cryogenic cycling software code, as well as some of the more significant data analysis code discussed in Chapter 5.

[1] Lena, P., *Observational Astrophysics*, Springer-Verlag, New York, Ed. M. Harwit, R. Kippenhalm, J. P. Zahn, 1988.

Chapter 2

Bolometer Construction and Theory

2.1 Introduction

The twin composite Ge:Ga bolometers used in the detector system were manufactured at Queen Mary and Westfield College, University of London (QMW) [1]. Bolometers of this type find extensive use as sensitive detectors of far infrared radiation, and have been described previously by several authors [2,3,4]. In this chapter, the key features of the bolometer construction are described, and the general theory of bolometer operation is presented. The theoretical equations developed in this chapter will be used for analysing the V-I data in Chapter 5. In the following discussion, a distinction is made between the detector system, consisting of the entire dewar and its contents, the actual bolometer elements, and the two bolometer units each consisting of a composite bolometer element and the associated support structure mounted in an integrating cavity.

2.2 Bolometer Unit Construction

Composite semiconductor bolometers generally consist of a small resistive element, with a large temperature coefficient of resistance, mounted to a dielectric substrate. The dielectric substrate serves as the main absorber of the incident radiation, while the semiconductor element serves as the thermometer that measures the temperature fluctuations of the substrate. As we will show, the frequency response of a bolometer is increased as the heat capacity is reduced. Thus it is advantageous to use a dielectric with low specific heat for the large surface area element which absorbs the radiation, and to make the bolometer crystal, with its intrinsically high specific heat, as small as possible. To ensure that the temperature measured by the bolometer element closely follows the fluctuations in the incident radiation, the thermal conductivity of the substrate must also be as high as possible.

Figure 2.1a shows the general design of the composite bolometers used in this detector. Table 2.1 gives the physical dimensions and heat capacities of the various bolometer components,as measured by QMW [1]. Each bolometer consists of a small rectangular nuclear transmutation doped (NTD) Ge:Ga bolometer element (Haller semiconductor #13 [5]) mounted on a thin sapphire disc. The surface of the substrate opposite to the incident radiation is coated with a 0.1 μm thick Bismuth metal film in order to improve its absorption efficiency [2]. The bolometer is suspended in an integrating cavity by two Pyrex rods that provide stiff

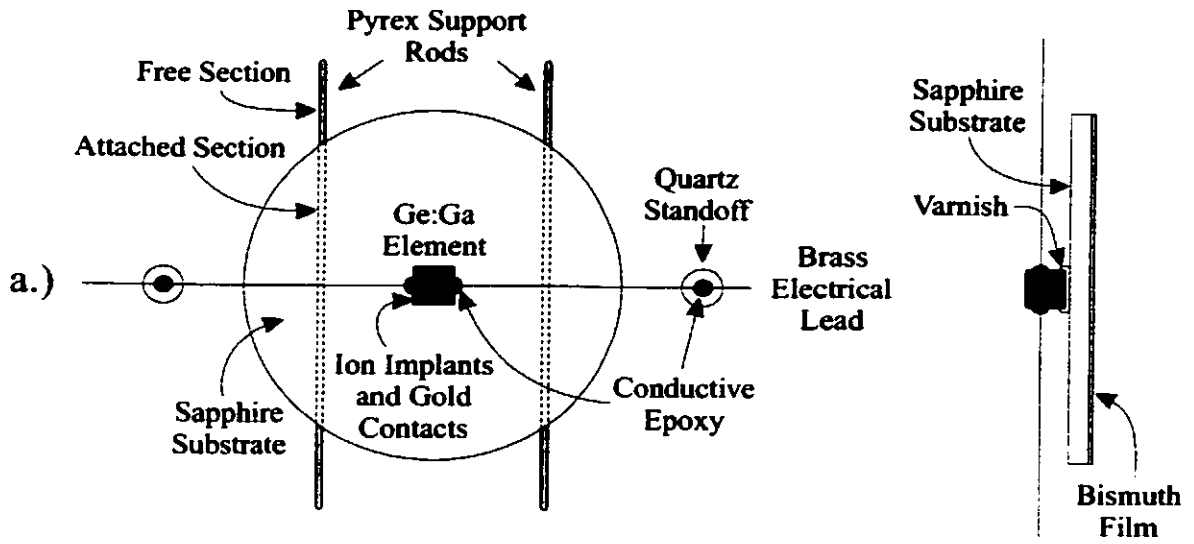

Figure 2.1 : Details of the bolometer unit construction.

support, ensuring that any microphonic vibration of the element will occur at a high frequency well above the optical signal modulation frequencies produced by the FTS. The two ends of the element are boron ion implanted, then palladium and gold plated to provide a good thermal and electrical connection with the two brass electrical leads. The brass wires, quartz standoffs, and to a lesser extent the Pyrex rods, define the thermal conduction path to the integrating cavity housings, which are cooled to the temperature of the cold stage (~0.3 K). This thermal conductance, as we will show, is of critical importance to the low noise and high frequency operation of the bolometers.

Table 2.1 : Bolometer Dimensions and Heat Capacity

Material	Specific Heat ($J/K/mm^3$)	# per bolo-meter	Dimensions X (mm)	Y/Diam. (mm)	Z/Length (mm)	Volume (mm^3)	Heat Capacity (J/K)
Ge:Ga Element	$2.928 \cdot 10^{-10}$	1	0.25	0.25	0.275	$1.718 \cdot 10^{-2}$	$5.033 \cdot 10^{-12}$
Ion Implant	$3.5 \cdot 10^{-10}$	2	0.25	0.25	10^{-3}	$1.25 \cdot 10^{-4}$	$4.375 \cdot 10^{-14}$
Palladium	$3.773 \cdot 10^{-7}$	2	0.25	0.25	$2 \cdot 10^{-5}$	$2.5 \cdot 10^{-6}$	$9.432 \cdot 10^{-13}$
Gold Contact	$2.644 \cdot 10^{-8}$	2	0.25	0.25	$2.5 \cdot 10^{-4}$	$3.125 \cdot 10^{-5}$	$8.263 \cdot 10^{-13}$
GE7031 Varnish	$3.363 \cdot 10^{-9}$	1	0.2	0.2	0.01	$4 \cdot 10^{-4}$	$1.345 \cdot 10^{-12}$
Silver Epoxy	$1.367 \cdot 10^{-8}$	2	0.15	0.15	0.02	$9 \cdot 10^{-4}$	$1.230 \cdot 10^{-11}$
Brass Wire	$4.778 \cdot 10^{-8}/3$	2	-	0.012	2.5	$5.655 \cdot 10^{-4}$	$9.005 \cdot 10^{-12}$
Sapphire Disc	$1.356 \cdot 10^{-11}$	1	-	3	0.03	0.212	$2.875 \cdot 10^{-12}$
Bismuth Film	$2.690 \cdot 10^{-9}$	1	-	3	10^{-4}	$7.069 \cdot 10^{-4}$	$1.901 \cdot 10^{-12}$
Pyrex Rod (free)	$1.089 \cdot 10^{-9}/3$	4	-	0.014	0.65	$4.002 \cdot 10^{-4}$	$1.453 \cdot 10^{-13}$
Pyrex (attached)	$1.089 \cdot 10^{-9}$	2	-	0.014	2.6	$8.005 \cdot 10^{-4}$	$8.718 \cdot 10^{-13}$
						Total Heat Capacity :	$3.531 \cdot 10^{-11}$

It will also be shown later in this chapter that minimizing the heat capacity of the bolometer maximizes its frequency response. From Table 2.1 it can be seen that the largest contributions to the heat capacity are from the bolometer element itself, the brass wires, and the conductive epoxy used to bond the wires to the gold contacts. The dimensions of these components are optimized by considering the following: The bolometer element can only be made smaller at the expense of lower resistance, the brass wires need to be thick enough to create a large thermal conductance, and the the epoxy droplets must be large enough to ensure

good thermal and electrical bonds.

There is considerable uncertainty in the value of the total heat capacity, due not to measurement error, but rather to the uncertainty in the geometry of the components. The corners of the bolometer element, for example, are rounded as a result of the manufacturing process, and therefore the volume will be somewhat less than the calculated value, even though the dimensions given in Table 2.1 are accurate to ± 1 μm. More importantly, the volume of varnish used in bonding the bolometer crystal to the substrate, and of the epoxy forming the electrical connections, cannot be controlled precisely during construction.

The factor of 3 reduction in the specific heats given in the table for the brass wires and the unbonded sections of the Pyrex rods should be noted. When a rod is connected between a heat sink and a body with sinusoidally varying temperature, the thermal conductance acts to effectively lower the heat capacity of the rod [6]. While this effect is not present when the bolometer is viewing a constant source, the heat capacity is only used for determination of the frequency response of the detector.

The two bolometer units are each composed of a bolometer element and substrate, an integrating cavity, and a f/3 Winston cone [7] light collector. Figure 2.1b shows a schematic of the bolometer unit construction. The hemispherical integrating cavities are machined from copper and form the mechanical housing for the bolometer elements. The Winston cones (also referred to as feed horns) and the integrating cavities concentrate the radiation from the field optics system (described in Chapter 3) onto the bolometer elements, maximizing the overall absorption efficiency. Since the efficiency of a Winston cone is highly dependent on the smoothness of the reflecting surface, the horns are manufactured by electroplating copper onto precision ground, paraboloid mandrels instead of being milled out of solid stock by conventional methods. The integrating cavities and horns are also gold plated to improve their reflectivity. The 5.6 mm entrance apertures of the horns define the f/3 field of view for the bolometers (the detector *system* field of view is adjustable and is discussed in Chapter 3), and the horns are each fitted with 55 cm^{-1}, low-pass, alkali-halide edge filters. These filters are necessary to prevent any residual stray radiation above 55 cm^{-1} (including near infrared) from reaching the bolometers. A diagram of the bolometer units mounted on the cold stage is given in Figure 3.2.

A schematic of the heat flow through the bolometer element is shown in Figure 2.2a. Radiation

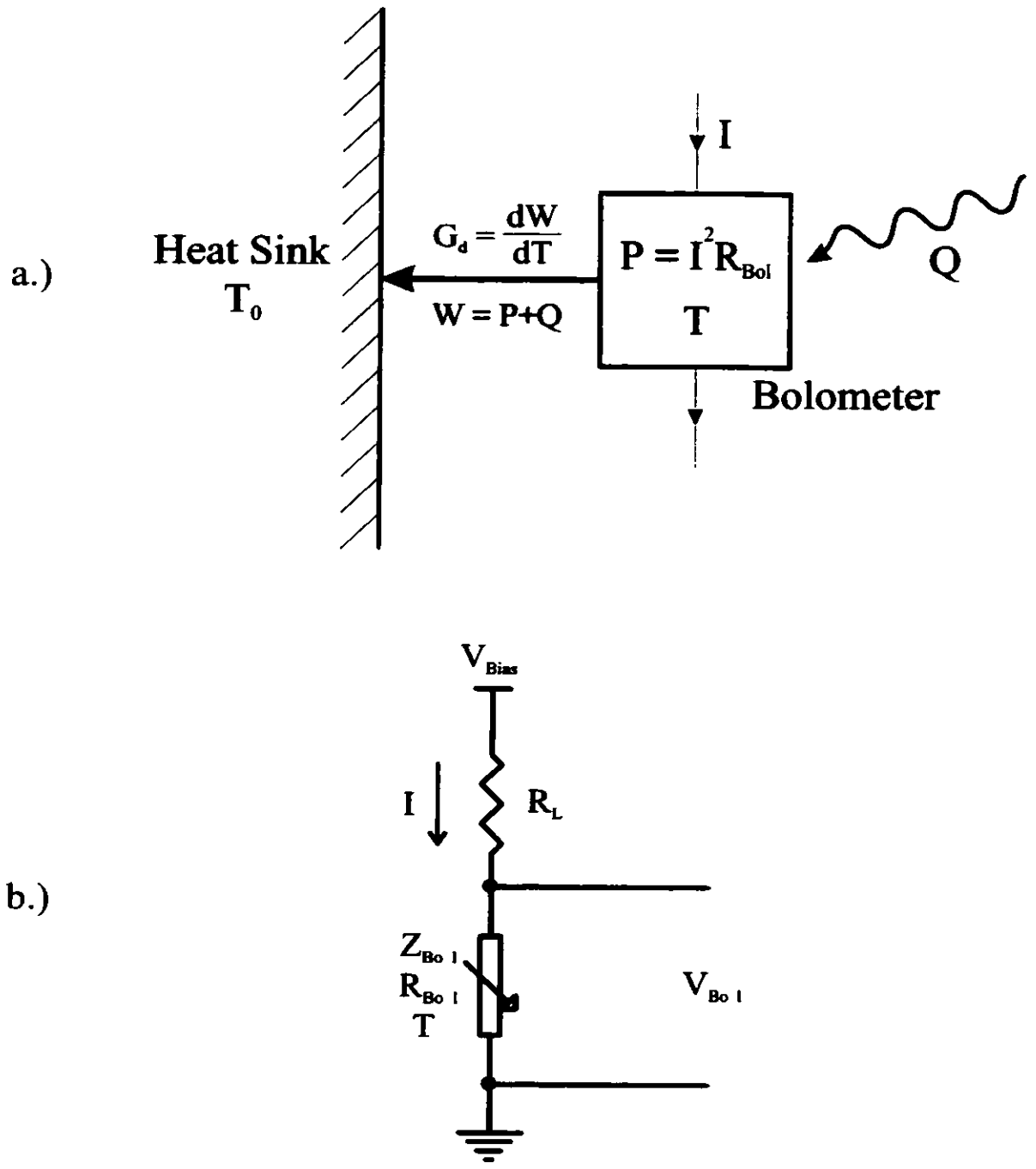

Figure 2.2 : Schematics of the equivalent thermal (a.) and electrical (b.) circuits for the bolometers.

incident on the bolometer (from the source and background) is represented by a radiant power loading of Q, while Joule heating of the bolometer element by the bias current is represented by P. The bolometer element reaches thermal equilibrium at a temperature T when the power flowing into the element is balanced by the power flowing out through the thermal link. In the steady state, the rate of heat flow out of the bolometer, W, is given by Equation (2.1).

$$W = P + Q \ . \tag{2.1}$$

In general, the steady state thermal conductance, G, of a thermal link depends on the temperature gradient, composition, and geometry of the link, and is given in Equation (2.2) as the thermal conductivity, k, multiplied by the cross-sectional area to length ratio of the link. Since the temperature distribution in the link will depend on the temperature of the bolometer element, T, and the temperature of the heat sink, T_0, the thermal conductivity and thermal conductance, will be functions of T and T_0. Now, since the total heat flow, W, must pass through the thermal link, it is equal to the thermal conductance multiplied by the temperature difference across the link as given in Equation (2.3). The dynamic thermal conductance, G_d, is defined by Equation (2.4) as the rate change of heat flow caused by a change in the temperature of the bolometer element, T. If the radiant power loading, Q, is constant, then the temperature of the bolometer varies only with a change in the joule heating caused by a change in bias current. Thus, if we know the electrical power dissipated by the bolometer as a function of T, we can write Equation (2.5).

$$G_{(T,T_0)} = k_{(T,T_0)} \frac{A}{l} \qquad (W/K) \ . \tag{2.2}$$

$$W = G_{(T,T_0)} \cdot (T - T_0) \ . \tag{2.3}$$

$$G_d = \frac{dW}{dT} \tag{2.4}$$

$$= \frac{d}{dT}(P + Q)$$

$$= \frac{dP}{dT} \ . \tag{2.5}$$

These equations provide two ways of determining the total thermal conductance of the bolometer: by measuring the geometry and thermal conductivities of the thermal links, and by measuring the change in electrical power as a function of temperature. In our case, the thermal links are formed by the two brass

electrical connections, the two short quartz standoffs connecting the brass wires to the bolometer housing, and the two Pyrex support rods (see Figure 2.1). The thermal conductivities of these materials have been measured [8], and plots of the values are given in Figure 2.3. The thermal conductance is primarily determined by the brass leads; the contribution from the two Pyrex support rods is negligible since the thermal conductivity of Pyrex is nearly 2 orders of magnitude smaller and the rods are relatively thin and long (see Table 2.1). For example, using the thermal conductivity at 0.35 K from the figure, and the dimensions of the rods given in the table, Equation (2.2) gives a thermal conductance of ~ 18.1 nW/K for the brass wires, and ~ 2.4 nW/K for the Pyrex rods. The conductance of the quartz standoffs can be disregarded since the standoffs are short and thick, and quartz has a much lower thermal conductivity than brass, therefore the conductance of the brass will be the limiting factor.

Most authors assume a power law form for steady-state thermal conductance at low temperatures as given by Equation (2.6), where G_0 is the thermal conductance at the bath temperature $T=T_0$, and β is a material dependent parameter, ~1 for metals and ~3 for dielectrics [9]. Further, the assumption is usually made that the temperature of the link can be considered to be some average of the bolometer and bath temperatures (which is valid for a perfectly symmetrical rod of homogenous composition).

$$G = G_0\left(\frac{T}{T_0}\right)^{\beta} \quad . \tag{2.6}$$

$$\therefore \quad W = G\cdot(T-T_0) = G_0\left(\frac{T}{T_0}\right)^{\beta}(T-T_0) \quad .$$

If the thermal conductance is accurately represented by this equation, then the electro-thermal behaviour of the bolometer can be completely modelled. We will show, however, that in our case the thermal conductance is not completely described by Equation (2.6). The actual thermal behaviour of the device can deviate from the theoretical predictions for several reasons: The measurement of the dimensions of the wires and support rods are subject to error, the value of the thermal conductance depends on the particular brass alloy or glass composition used, and the small physical dimensions of the links in our bolometer may produce behaviour that differs from that measured in larger scale samples.

In order to proceed, we need to derive an expression for the thermal conductance in terms of directly

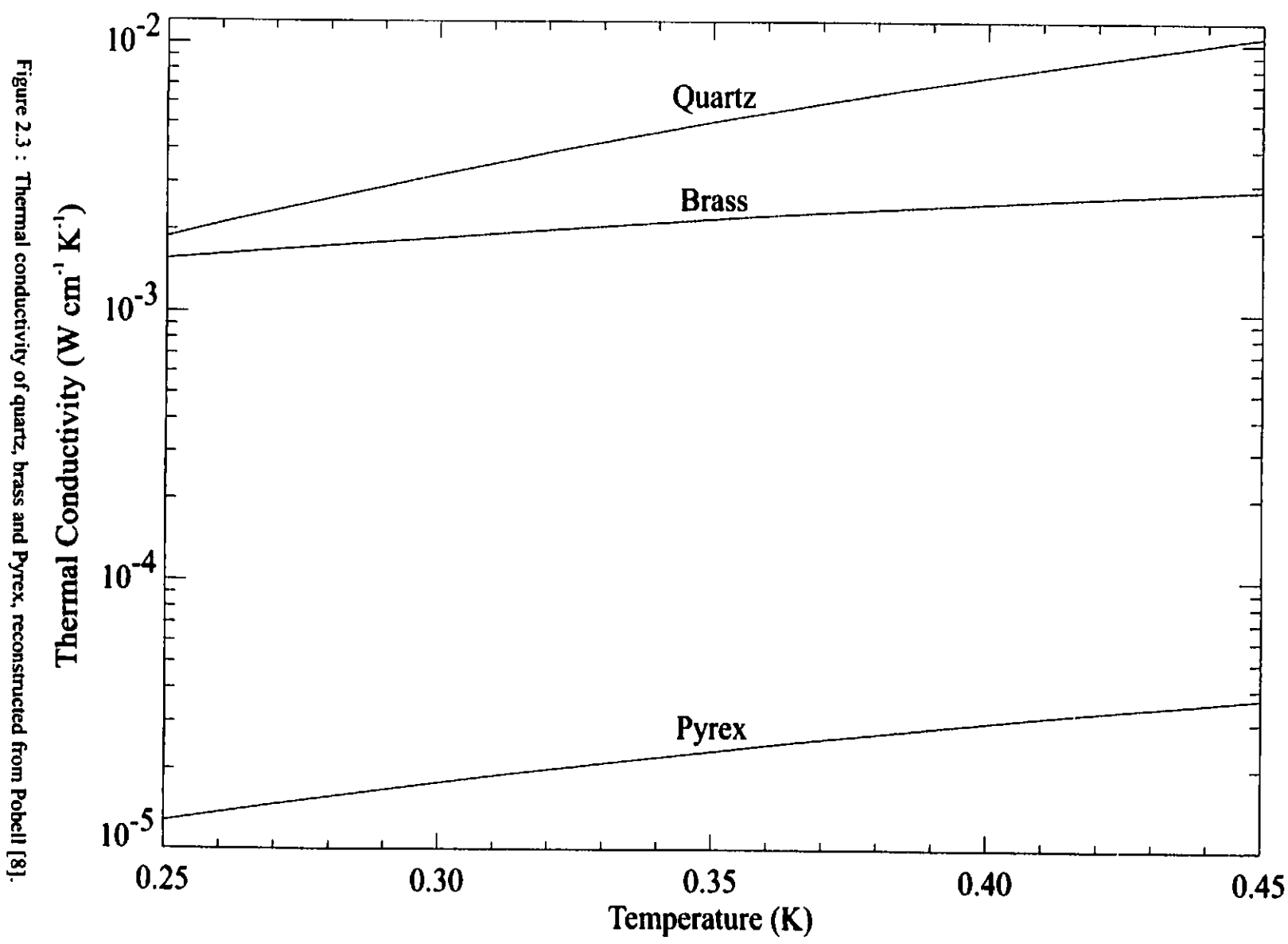

Figure 2.3 : Thermal conductivity of quartz, brass and Pyrex, reconstructed from Pobell [81].

measurable electrical quantities. An equivalent electrical circuit for a typical bolometer is shown in Figure 2.2b. In this figure, the bolometer element is represented by a resistance R_{Bol}, with a value that varies as a function of its temperature, T. A bias voltage, V_{Bias}, applied across a load resistor, R_L, in series with the bolometer, creates a bias current, I. The load resistor is chosen to be much larger than R_{Bol} so that the bias current has a minimal dependence on the bolometer resistance. The bolometer signal is then measured as the voltage drop across the bolometer, V_{Bol}. The dynamic impedance of the bolometer is defined as:

$$Z_{Bol} = \frac{dV_{Bol}}{dI} \quad . \tag{2.7}$$

It should be noted that the bolometers in this detector are configured for fully differential operation, where the bolometer elements are connected in series between 2 load resistors, each with half the resistance of R_L, in order to cancel out common mode noise. The differential electronics system is discussed in Chapter 3. For this analysis, however, we will use the simplified circuit given above.

The resistivity of Ge:Ga as a function of doping level has been measured by Haller [5], so given the dimensions of the crystal (Table 2.1), we can determine the bolometer resistance as a function of temperature. The resistance is simply the resistivity multiplied by the length to cross-sectional area ratio, and can be written in the empirical form of Equation (2.8), where T_g is a material dependent parameter, and R^* is a combined material and geometry parameter. For a chip of Haller NTD material #13 with the dimensions of our bolometer elements, $R^* = 7.56\ \Omega$ and $T_g = 62.6$ K. Figure 2.4 shows the resistance of the bolometer elements over their typical operating temperature range.

$$R_{Bol} = R^* e^{\sqrt{T_g/T}} \quad . \tag{2.8}$$

This equation can be solved for T, and written in terms of V_{Bol} and I:

$$T = \frac{T_g}{\left(\ln \frac{R_{Bol}}{R^*}\right)^2} = \frac{T_g}{\left(\ln \frac{V_{Bol}}{IR^*}\right)^2} \quad . \tag{2.9}$$

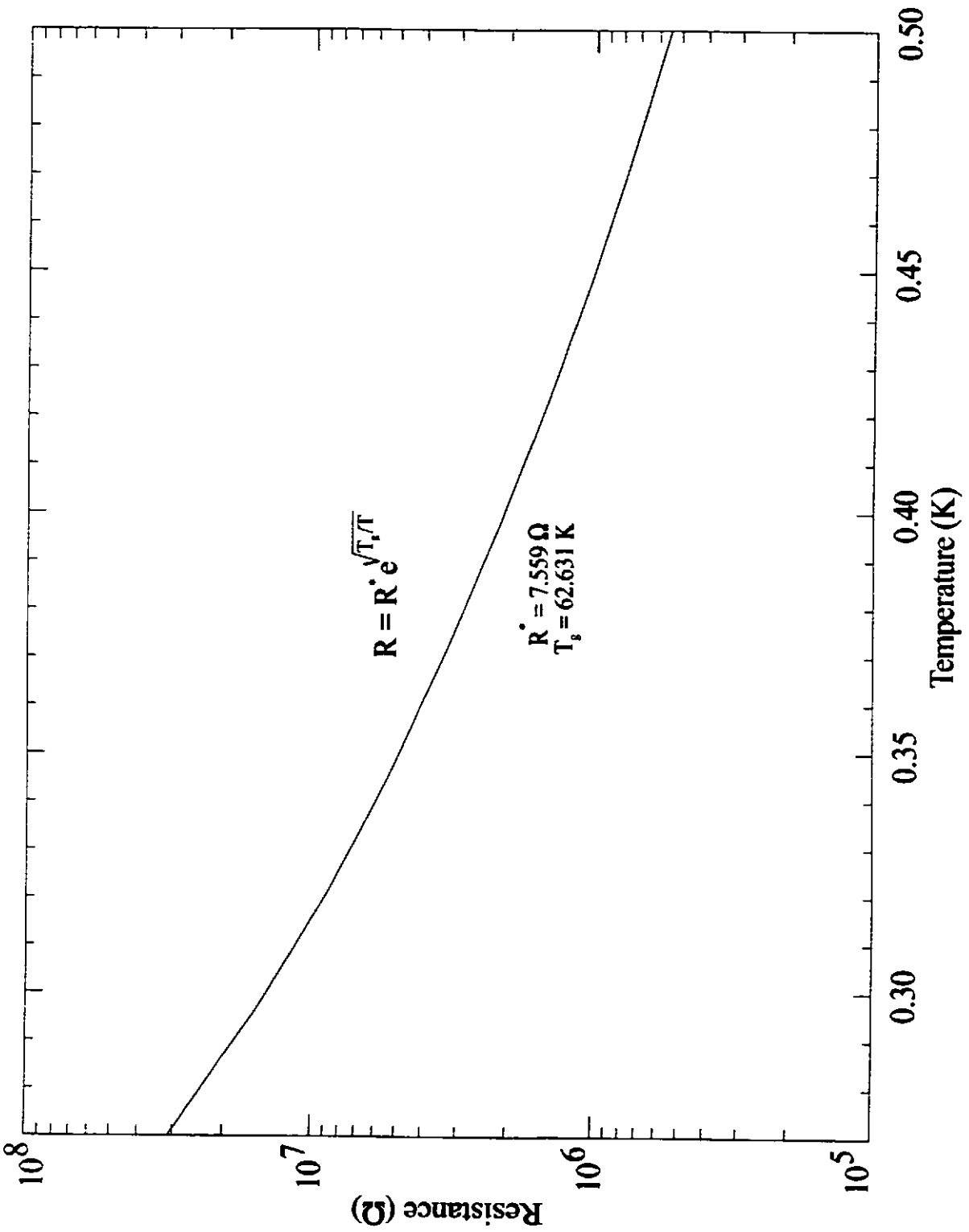

Figure 2.4 : **Resistance of the bolometer elements as a function of temperature [5].**

We can also write the temperature coefficient of resistance, α, as:

$$\alpha \equiv \frac{1}{R_{Bol}} \frac{dR_{Bol}}{dT} = -\frac{\sqrt{T_g}}{2T^{3/2}} = -\frac{1}{2T_g}\left(\ln\left(\frac{V_{Bol}}{IR^*}\right)\right)^3 . \tag{2.10}$$

The Joule heating of the element is given by Equation (2.11).

$$P = V_{Bol} I = I^2 R_{Bol} = \frac{V_{Bol}^{\ 2}}{R_{Bol}} . \tag{2.11}$$

Now we can relate the dynamic thermal conductance and the resistance using Equation (2.12) (see Appendix 2.1).

$$\begin{aligned} G_d &= \frac{dP}{dT} \\ &= \alpha P\left(\frac{Z_{Bol} + R_{Bol}}{Z_{Bol} - R_{Bol}}\right) \\ &= I^2 \frac{dR_{Bol}}{dT}\left(\frac{Z_{Bol} + R_{Bol}}{Z_{Bol} - R_{Bol}}\right) . \end{aligned} \tag{2.12}$$

Since the flow of heat through the bolometer is analogous to the flow of electrical current through an RC circuit, we can define a thermal relaxation time constant given by Equation (2.13), where G is the reciprocal of the thermal resistance and C is the thermal capacitance.

$$\tau \equiv \frac{C}{G_d} . \tag{2.13}$$

Zwerdling [10] has shown that the electro-thermal interaction between the heating of the bolometer from the absorbed radiation and the resulting change in dissipated electrical power acts to increase the apparent thermal conductivity. The resulting effective thermal conductance, G_e, is given by Equation (2.14) where the term in the brackets is referred to as the "static electro-thermal interaction" function.

$$G_e = G_d - \alpha P\left(\frac{R_L - R_{Bol}}{R_L + R_{Bol}}\right) . \tag{2.14}$$

As a result of this change in the thermal conductance, the measured time constant of the electrical detector signal differs from the physical time constant in Equation (2.13) when the detector views a chopped radiation source. This effective time constant, τ_e, is given in Equation (2.15). Equation (2.16) shows that in general, τ_e will be smaller than τ, and in the special case when Z_{Bol} is zero (and $R_L >> R_{Bol}$), the electro-thermal interaction acts to effectively double the frequency response of the detector. The results of this analysis for this detector system are discussed in the frequency response section of Chapter 5.

$$\tau_e \equiv \frac{C}{G_e} = \frac{C}{\alpha P}\frac{(R_{Bol}+R_L)(Z_{Bol}-R_{Bol})}{2R(Z_{Bol}+R_L)} . \tag{2.15}$$

$$\therefore \quad \frac{\tau_e}{\tau} = \frac{Z_{Bol}+R_{Bol}}{2R_{Bol}}\frac{R_{Bol}+R_L}{Z_{Bol}+R_L} . \tag{2.16}$$

2.3 Theoretical V-I Equations

By extending the previous analysis, we can generate the theoretical bolometer voltage and bias current as a function of bolometer temperature. In Chapter 5, the resulting voltage vs. current curves are fitted to the experimental data, providing a method of determining several bolometer parameters.

The power dissipated by the bolometer element is given by Equation (2.17). We can immediately solve for the bias current and bolometer voltage as given by Equations (2.18).

$$P = I^2 R_{Bol} = V_{Bol} I . \tag{2.17}$$

$$\therefore \quad I = \sqrt{P/R_{Bol}} \quad , \quad V_{Bol} = \sqrt{PR_{Bol}} . \tag{2.18}$$

Using Equations (2.1) and (2.4) we can write the electrical power as:

$$\begin{aligned} P &= W - Q \\ &= \int_{T_0}^{T} G_d \, dT - Q . \end{aligned} \tag{2.19}$$

If the thermal conductance is completely described by the power-law form of Equation (2.6), then we do not have to evaluate the integral in Equation (2.19); we can write Equation (2.20) instead.

$$P = G_0 \left(\frac{T}{T_0}\right)^{\beta} (T - T_0) - Q . \tag{2.20}$$

We can now use Equation (2.8) to rewrite the bias current and bolometer voltage equations as Equations (2.21). Alternatively, if the thermal conductance does not have a simple power law form, we can write the V-I equations as Equations (2.22).

$$I = \sqrt{\frac{G_0\left(\frac{T}{T_0}\right)^{\beta}(T-T_0)-Q}{R^{*}e^{\sqrt{T_g/T}}}}\,, \qquad V = \sqrt{\left[G_0\left(\frac{T}{T_0}\right)^{\beta}(T-T_0)-Q\right]\cdot R^{*}e^{\sqrt{T_g/T}}}\,. \tag{2.21}$$

$$I = \sqrt{\frac{\int_{T_0}^{T} G_d\,dT - Q}{R^{*}e^{\sqrt{T_g/T}}}}\,. \qquad V = \sqrt{\left[\int_{T_0}^{T} G_d\,dT - Q\right]\cdot R^{*}e^{\sqrt{T_g/T}}}\,. \tag{2.22}$$

These are the fundamental equations that will be used for the analysis of the V-I data in Chapter 5.

Appendix

Appendix 2.1 :

Since the resistance of the bolometer is a strong function of temperature, a change in Q will cause a change in R_{Bol}. Consequently, the electrical power dissipated by the element, P, will vary with temperature in a complex manner. In order to calculate the thermal conductance as a function of temperature, we need to calculate the derivative of the dissipated power with respect to temperature. In all the following equations, V, R, and Z are used instead of V_{Bol}, R_{Bol}, and Z_{Bol} for compactness. The other terms use the same notation as the text.

In order to determine $\frac{dP}{dT}$ we will need the following result, where we make use of the fact that the load resistors are metal film and therefore their impedance, Z_L, is simply their resistance (they have zero inductance unlike a wire-wound resistor).

$$
\begin{aligned}
\frac{dR}{dI} &= \frac{d}{dI}\left(\frac{VR_L}{V_{Bias}-V}\right) \\
&= \left(\frac{1}{V_{Bias}-V}\right)\frac{d(VR_L)}{dI} + (VR_L)\frac{d}{dI}\left(\frac{1}{V_{Bias}-V}\right) \\
&= \left(\frac{R_L}{V_{Bias}-V}\right)\frac{dV}{dI} - (VR_L)\left(\frac{1}{V_{Bias}-V}\right)^2\left(\frac{dV_{Bias}}{dI}-\frac{dV}{dI}\right) \\
&= \frac{R_L Z}{V_{Bias}-V} - \frac{VR_L}{(V_{Bias}-V)^2}(Z+Z_L-Z) \\
&= \frac{Z}{I} - \frac{VR_L Z_L}{(IR_L)^2} \\
&= \frac{Z}{I} - \frac{VZ_L}{I^2 R_L} \\
&= \frac{Z}{I} - \frac{R}{I} \qquad (Z_L = R_L)\ .
\end{aligned}
$$

$$
\therefore\ \frac{dI}{dR} = \frac{I}{Z-R}\ .
$$

Now we can calculate $\frac{dP}{dT}$:

$$\frac{dP}{dT} = \frac{d(VI)}{dT} = V\frac{dI}{dT} + I\frac{dV}{dT}$$

$$= V\frac{dI}{dR}\frac{dR}{dT} + I\frac{dV}{dR}\frac{dR}{dT}$$

$$= \alpha VR\frac{dI}{dR} + \alpha IR\frac{dV}{dR}$$

$$= \frac{\alpha V^2}{I}\frac{dI}{dR} + \alpha V\frac{dV}{dI}\frac{dI}{dR}$$

$$= \frac{\alpha V^2}{I}\frac{I}{Z-R} + \alpha VZ\frac{I}{Z-R}$$

$$= \frac{\alpha V(V+IZ)}{Z-R}$$

$$= \frac{\alpha V^2\left(1+Z/R\right)}{Z-R}$$

$$= \frac{\alpha V^2}{R}\left(\frac{Z+R}{Z-R}\right)$$

$$= \alpha P\left(\frac{Z+R}{Z-R}\right).$$

The last equation is the same as that given by Jones [11], where the term in the brackets is referred to as the "slope parameter", H.

[1] Department of Physics, Queen Mary and Westfield College, Mile End Road, London, E1 4NS, UK

[2] El-Atway, S., and P. A. R. Ade, "Far-Infrared Composite Bolometers Using Surface Ion Implanted Ge as an Absorbing Surface", *Infrared Physics*, Vol. 18, 683-690, 1978.

[3] Dereniak, E., and D. Crowe, *Optical Radiation Detectors*, John Wiley & Sons, New York, 1984.

[4] Nishioka, N. S., P. L. Richards, and D. P. Woody, "Composite Bolometers for Submillimetre Wavelengths", *Applied Optics*, Vol. 17, 1562-1567, 1978.

[5] Haller, E. E., "Physics and Design of Advanced IR Bolometers and Photoconductors", *Infrared Physics*, Vol. 25, 257, 1985.

[6] Smith, R. A., F. E. Jones, and R. P. Chasmar, *The Detection and Measurement of Infra-Red Radiation*, 2nd ed., Oxford, Toronto, 1968, p.55.

[7] Harper, D. A., R. H. Hildebrand, R. Stiening, and R. Winston, "Heat Trap: an Optimized Far Infrared Field Optics Systems", *Applied Optics*, Vol. 15, 53-60, 1976

[8] Pobell, F., *Matter and Methods at Low Temperatures*, 2nd ed., Springer-Verlag, New York, 1996, p. 58.

[9] beta parameter for dielectrics

[10] Zwerdling, S., R. A. Smith, and J. P. Theriault, "A Fast, High-Sensitivity Bolometer Detector for the Very-Far Infrared", *Infrared Physics*, Vol. 8, 271-336, 1968.

[11] Jones, R. C., "General Theory of Bolometer Performance", *J. Opt. Soc. Am.*, Vol. 43, 1-14, 1953.

Chapter 3

Detector Design and Construction

3.1 Introduction

In this chapter we present the details of the detector construction. The dewar, optics, filters, and electronics are discussed in separate sections. Construction of the filters, bolometer units and optical components, and assembly of the detector occurred at Queen Mary and Westfield College, University of London (QMW) [1]. The preamplifier was designed and built by Cochise Instruments [2]. The closed cycle cryogenic stage was a commercial unit manufactured by Chase Research [3], and its operation is discussed in Chapter 4.

3.2 Dewar Components and Construction

An Infrared Laboratories HDL8 extended dewar [4] was chosen as the system cryostat, since its large size affords space for the closed cycle cooling system, cooled optics, and the large nitrogen and helium vessels required for long hold times. A large, 76 mm diameter, cryostat input window was required to accept the diffraction limited image produced by the 15 m, f/35, James Clerk Maxwell Telescope (JCMT). A f/3 field lens matched this input beam to the f/3 bolometer feed horns. Even with this fast focal ratio, the optical path had to be folded to fit within the dewar. A diagram of the dewar dimensions is given in Figure 3.1. The system can be divided into 4 temperature layers: the outer case, the liquid nitrogen shield (73 K on Mauna Kea), the liquid ^{4}He shield (~ 4 K), and the liquid ^{3}He stage (~ 0.3 K). This series of radiation shields is necessary for minimizing the thermal loading of the cold stage, which enables lower ultimate bolometer operating temperatures and hence greater sensitivity, and longer operation times.

The 5 litre stainless steel liquid nitrogen vessel is suspended from the top plate of the dewar by 3 fibreglass supports and the fill tube. These rigid supports provide a stable mount for the entire internal structure while minimizing thermal conductance. A thin aluminum shield extends downward from the LN_2 vessel, forming the 73 K radiation shield. The effectiveness of this shield is improved by a layer of superinsulation which is wrapped around it and the nitrogen and helium vessels. This superinsulation is constructed from layers of reflective aluminized Mylar thermally isolated from each other by intervening layers of fine nylon mesh. The nylon mesh thermally decouples the Mylar sheets, and also prevents gas from being trapped between the sheets when the dewar is evacuated.

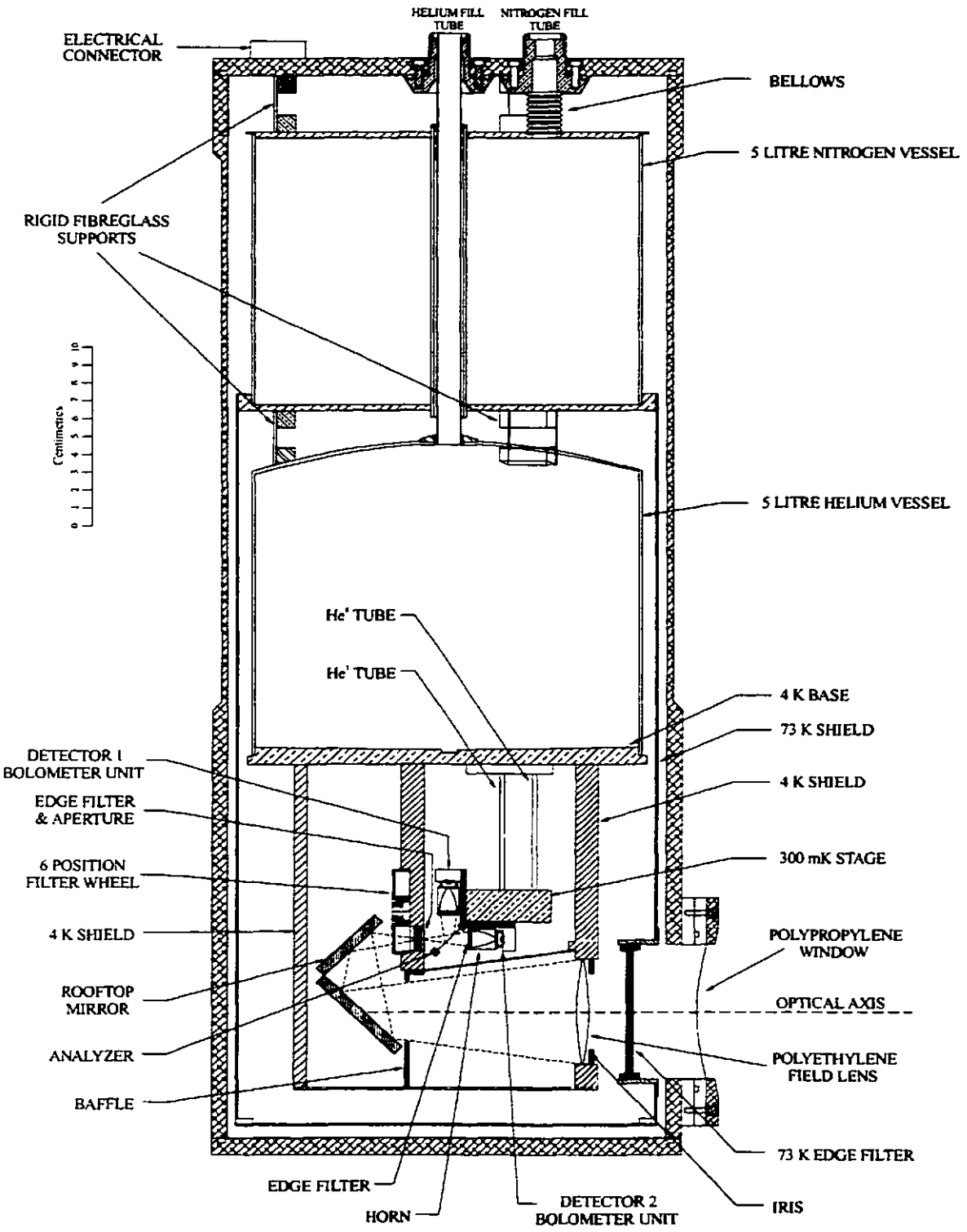

Figure 3.1 : Modified HDL8 dewar configuration.

Mounted to the bottom of the nitrogen vessel is the 5 litre helium vessel. This stainless steel vessel is mounted by 3 more fibreglass supports, and is filled via an isolated fill tube which passes though the nitrogen vessel and serves as additional support. The base of the vessel is a 9 mm thick copper plate which serves as the mounting surface for the LHe radiation shield, optical framework, and the closed cycle pumps and cold stage which are discussed in Chapter 4.

3.3 Optical System

Figure 3.2 shows the details of the optics and the cold stage. Radiation enters the dewar through a 76 mm diameter, 1 mm thick, polypropylene window, which is strong enough to withstand atmospheric pressure and yet is greater than 90 % transparent over the required wavelength range. Under pressure, the window bows in which reduces the formation of resonant optical cavities within the dewar, that produce unwanted channel spectra [5]. Mounted immediately after the window on the LN_2 shield is a large, ~ 75 mm diameter, 35 cm^{-1} capacitive grid low pass edge filter [6]. This type of metal grid filter remains colder (and is therefore a less significant source of thermal emission) than absorption filters for two reasons: It efficiently reflects short wavelength radiation (rather than absorbing it), and as a good thermal conductor, it is in better thermal contact with the LN_2 shield. The bandpass filters are of similar construction, and are described in the next section.

All the optics from this point on are cooled to the bulk LHe bath temperature to reduce their thermal emission. An adjustable iris provides an aperture stop that allows the optical beam to be matched to the diffraction limited beam of the telescope. Manual adjustment of the iris is made possible by a geared Torlon [7] shaft that passes to the outside of the dewar via a high vacuum feed-through. Torlon is a strong polymer that is thermally stable and has low thermal conductivity. The walls of the hollow shaft are thin, and the shaft is loosely coupled to the external mechanism to minimize heat transfer. A 65 mm diameter f/3 polyethylene planoconvex field lens is mounted to the frame directly after the iris. This lens re-images the telescope primary mirror onto the entrance apertures of the detector horns. The beam then passes through a 36 mm diameter baffle designed to block stray radiation. The relatively long focal length of the field lens requires that the beam be folded in order for the focal point to fall inside the dewar. An aluminum dihedral, or rooftop, mirror is used to redirect the beam through one of the 6 filters in the filter wheel, a 33 cm^{-1} edge filter, and a polarizer (analyser) mounted on the 0.3 K stage. In this way the orthogonal components of the beam from the

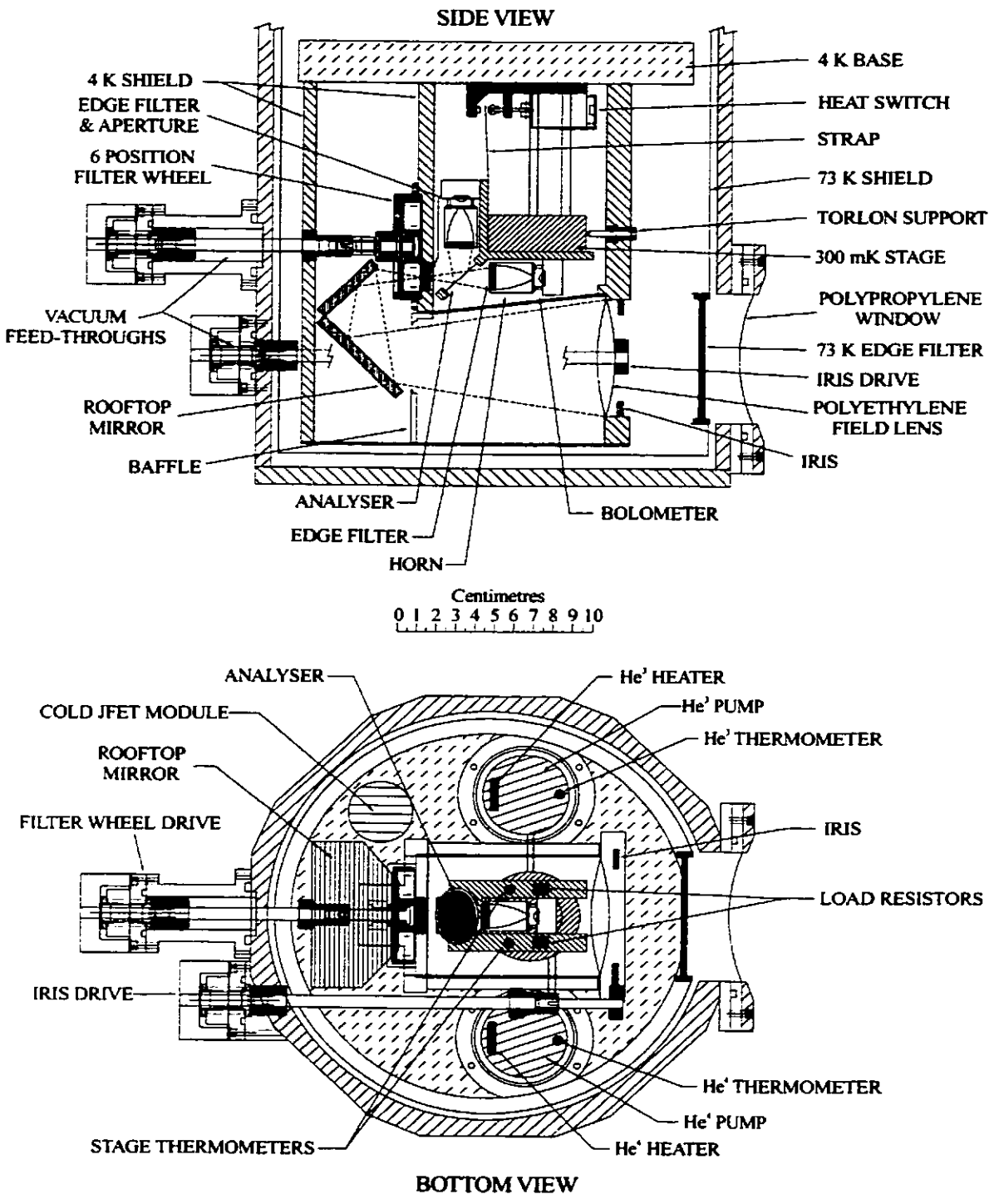

Figure 3.2: Details of the detector optics and 0.3 K stage.

polarizing FTS are recombined and directed to the two detector units. The Winston horn of each detector (described earlier in Chapter 2), is capped with a 5.6 mm aperture and 55 cm^{-1} edge filter, and concentrates the radiation into the integrating cavity which houses the bolometer element.

3.4 Filters

A six position filter wheel assembly, shown in Figure 3.3, houses filters with passbands that are matched to the atmospheric transmission windows of interest. Selection of a particular filter is enabled by a mechanical vacuum feed-through similar to the one used for the iris adjustment, with the exception that the external housing is elongated to allow for a longer Torlon drive shaft (see Figure 3.2). This longer shaft is required to reduce thermal conduction to the 4 K filter wheel, which would cause unwanted emission from the filters. A certain amount of play is needed in the shaft coupling to decrease thermal conduction, so the filter wheel is held in position by detents on the wheel assembly.

The filter units are composed of resonant metal mesh bandpass filter elements [6]. Figure 3.4 shows the geometry and equivalent circuit for the two filter types. A square mesh pattern of wires is analogous to a parallel LRC high-pass electrical filter circuit (Figure 3.4a), whereas a grid of isolated conducting squares is analogous to a series LRC low-pass filter (Figure 3.4b). When the two geometries are combined, the result is a resonant circuit with steep falloff (Figure 3.4c). Some of the filters units also include low pass capacitive grid edge filters to block higher frequency radiation (see Table 3.1). Each of these filters is composed of several individual layers, each supported by a dielectric substrate and separated by a vacuum space created by lapped stainless steel washers. Multiple layers improve the effectiveness of the filters, and enable multi-pole filters to be constructed.

Table 3.1 : Filter Units That Contain Edge Filters

Filter Band	Associated Edge Filter Cutoff
750	18 cm^{-1}
850	15 cm^{-1}
1100	10 cm^{-1}
1400	10 cm^{-1}

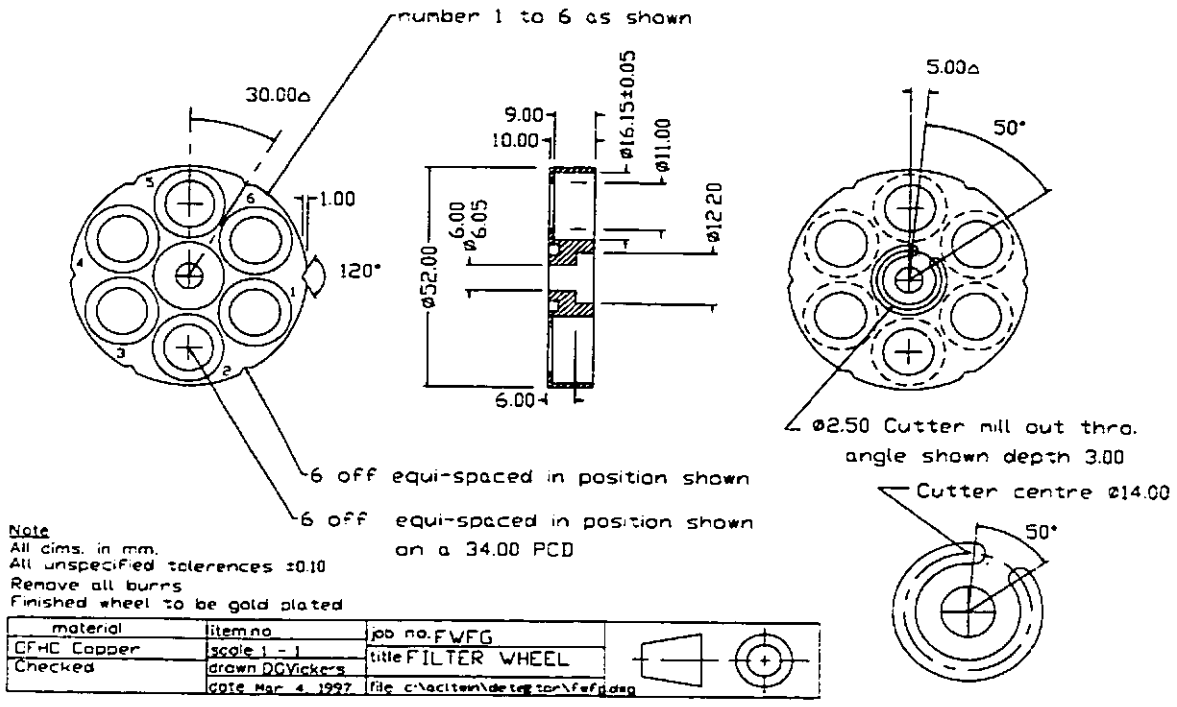

Figure 3.3: Six position filter wheel assembly.

a.) Inductive Mesh

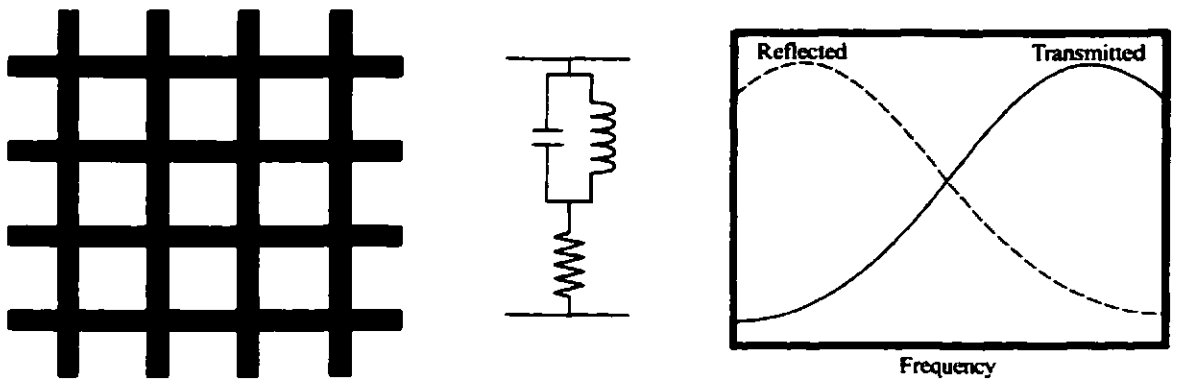

b.) Capacitive Mesh

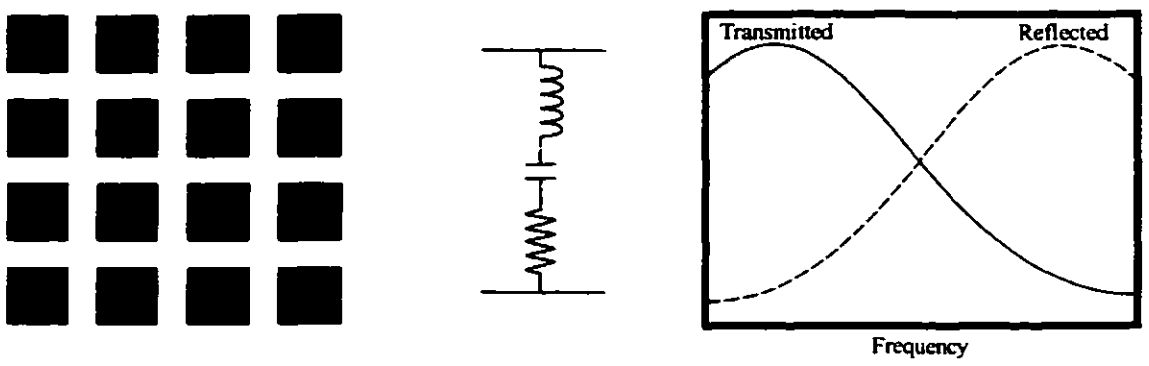

c.) Resonant Mesh

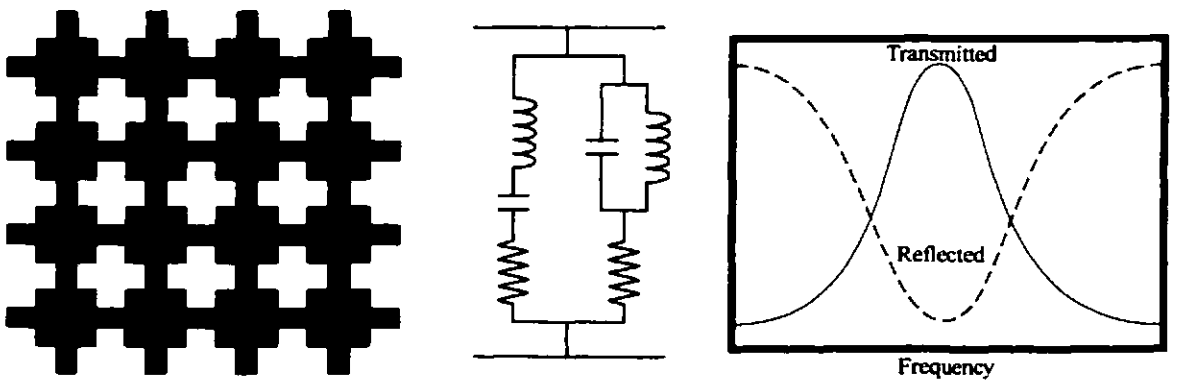

Figure 3.4: Geometry, equivalent circuits, and idealised spectral performance of mesh filters [6].

Profiles for the main filters as measured by QMW are shown in Figure 3.5. Similarly, Figure 3.6 shows the profiles for the dewar windows, blocking filters and edge filters. Measurements of the filter performance when mounted in the detector are described in Chapter 5. Figure 3.7 shows the measured filter profiles superimposed on a theoretical zenith transmission spectrum for the atmosphere above Mauna Kea, modelled for 0.5 mm of precipitable water vapour, corresponding to very good observing conditions.

The filter passbands are seen to be well matched to the atmospheric transmission windows, which minimizes the change in received flux as the width of the atmospheric windows changes with varying water vapour abundance. This matching is particularly important for a FTS system where such signal modulation creates a multiplex disadvantage [8]. In addition, the narrow passbands reduce the background radiant loading on the bolometers which increases their sensitivity.

3.5 Detector Electronics

The goal of the electronics design was to create a bolometer-noise limited system. Since the operating environment in the JCMT is particularly noisy, great care must be taken to eliminate electromagnetic interference (EMI) in the detector electronics. Large currents in the telescope drive give rise to large and variable magnetic fields. Noisy compressor motors are periodically activated. The grounding network of the telescope is not particularly good in the small signal sense, with common mode voltages of the order of volts often present between the telescope frame and the scientific instrumentation.

To ensure that induced currents are not generated in the presence of magnetic fields, all wiring inside the dewar is formed of twisted pairs (8 tpi), varnished down to the dewar structure. To reduce EMI associated with electric fields, the preamplifier is mounted in an RFI shielded box mounted to the side of the dewar. The power supply for the preamplifier and bolometer bias network is contained inside this box. The bolometers and JFETs are shielded by the dewar itself. Together, the bolometer, JFET, and preamplifier electronics can be considered to be within a single, shielded enclosure.

3.5.1 Detector Preamplifier Circuit

The novel feature of this detector system, and possibly the most significant factor in its performance, is the fully differential design of the detector, preamplifier and data acquisition electronics. Several low noise

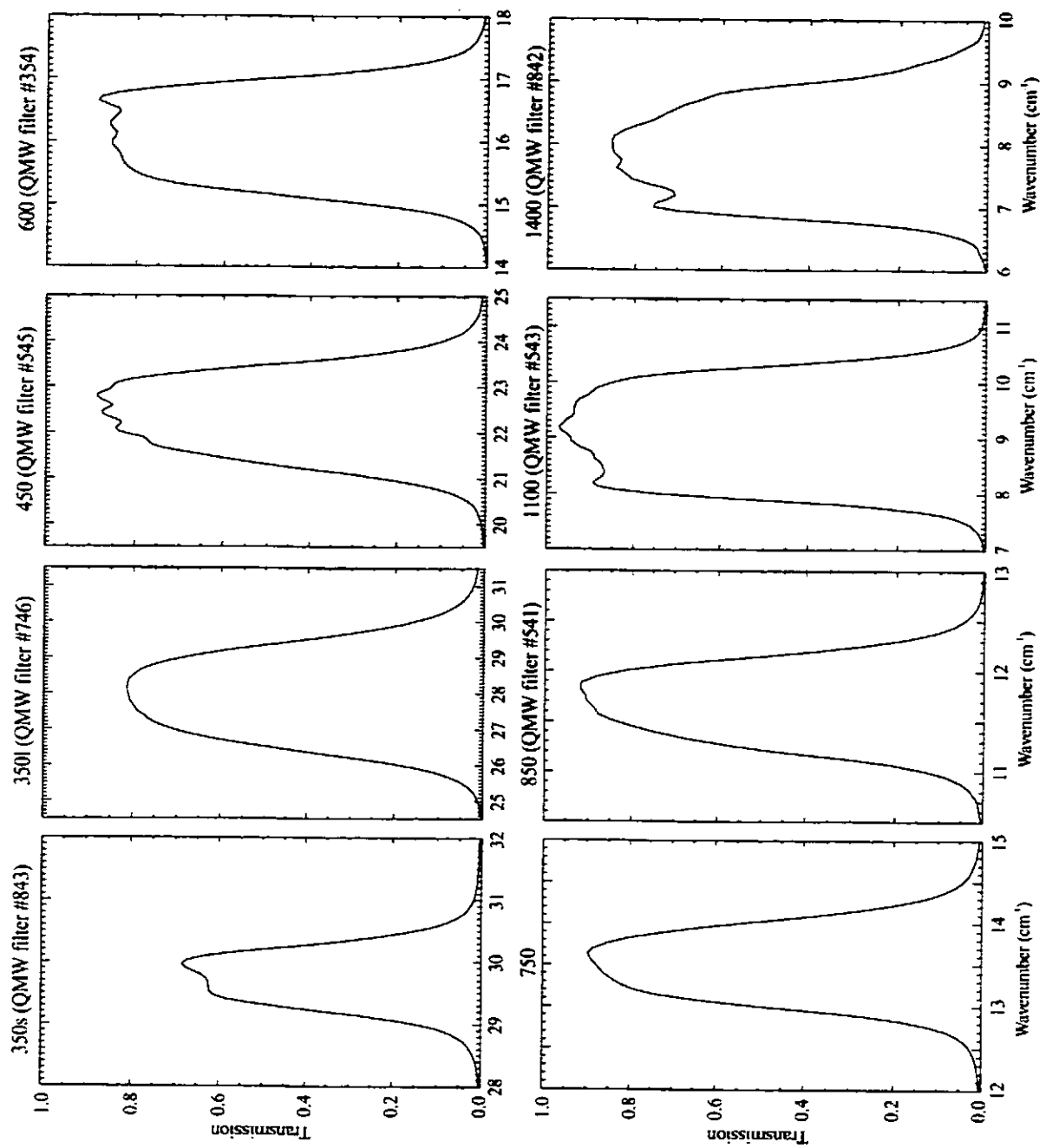

Figure 3.5 : Profiles for the filter elements and blocking filters as tested at the QMW.

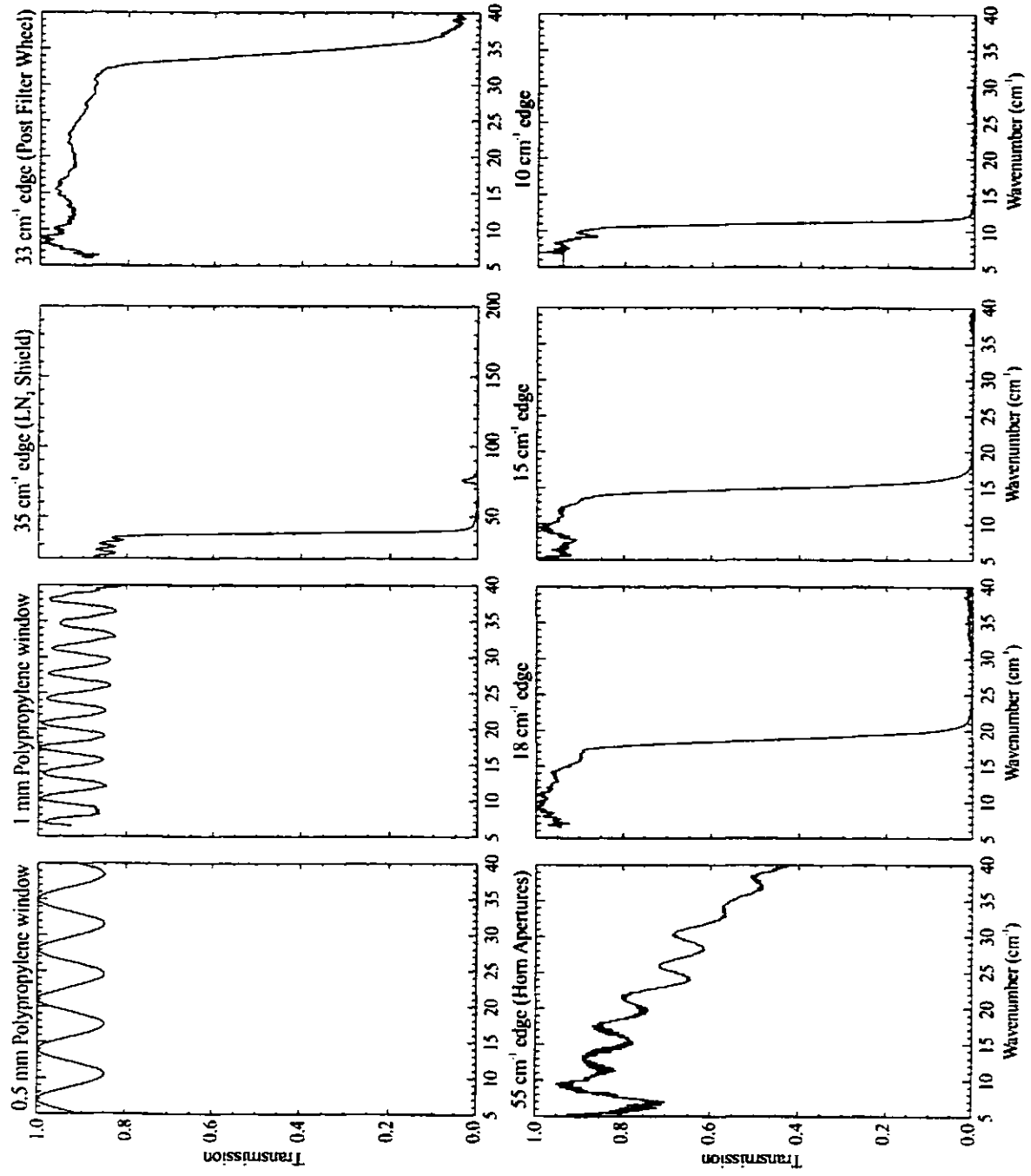

Figure 3.6 : Filter profiles for the dewar windows, blocking filters and edge filters associated with the 750, 1100, and 1400 μm filters.

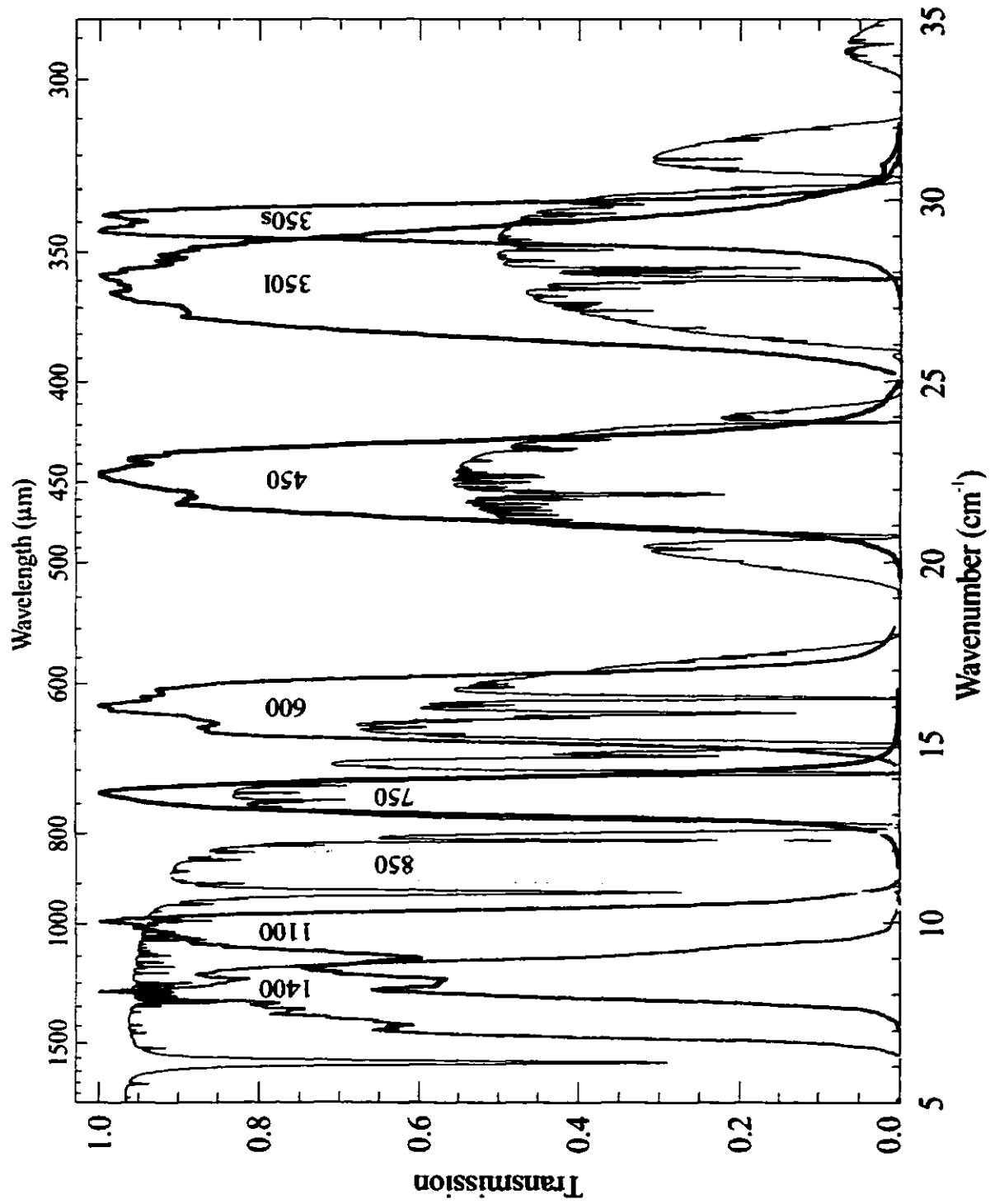

Figure 3.7 : Normalized profiles of available filter bands superimposed on zenith atmospheric transmission above Mauna Kea.

preamplifiers for far-infrared bolometers and photoconductors have been presented in literature [9,10,11], but none use the fully differential design described below.

In a balanced differential system, any external noise component induced in one signal line will be matched by an identical component induced in the other signal line. Upon taking the difference between the two signal lines, the interference components will cancel, leaving the desired differential signal from the detector element. However, this technique will only work if the entire detector system is completely symmetrical. Figure 3.8 shows a schematic of the symmetrical electronic design developed for these detectors. In this design, a bolometer element is isolated from the dewar ground and placed between two identical bias resistors and two identical and complementary active bias voltage generators. The cold preamplifier uses matched JFETs (IFN146 [12]) configured as source followers fed by a common drain voltage (4.96 V). The room temperature preamplifier consists of two identical channels, one for the inverting output and one for the non-inverting output. It is essential that the gains and phase shifts of the two channels are the same. Since the data acquisition system is located in the control room of the JCMT, a 30 m twisted pair, shielded cable connects the differential output of the preamplifier with a balanced differential line receiver designed to ensure that the complex impedances seen by the inverting and non-inverting signal lines are the same. Finally, the output of the line receiver is connected to a 16-bit differential ADC.

Figure 3.9 shows the schematic for one channel of the detector preamplifier. The preamp is essentially a two stage instrumentation amplifier, used to amplify the small differential signal across the bolometer element and reject common-mode noise. The input stage formed by the matched op-amps in U2 provides a differential gain of $G_{sig} = 1 + \frac{2 \cdot R7}{R9 + R11} \approx 10.5$ (in addition to the JFET gain of ~0.89), while maintaining a unity common-mode gain. The DC output op-amp, U3, removes any remaining common-mode noise and provides a single ended output representing the DC voltage across the bolometer element with a gain of 10. Similarly, the second stage of the preamp, consisting of U6 and U7 with a selectable gain of 10 or 100, produces a single ended AC output with a total gain of 100 or 1000. U4 and U8 are unity gain coax drivers which send the inverted and non-inverted signals (with a gain of 100 or 1000) to the data acquisition system. The RC filters formed by C9 and R21, and by C10 and R22, define the frequency response of the preamp and provide a high-pass cutoff frequency of 0.16 Hz in order to decrease 1/f noise without affecting the detector signal. The electronic system noise contribution is discussed in the following section.

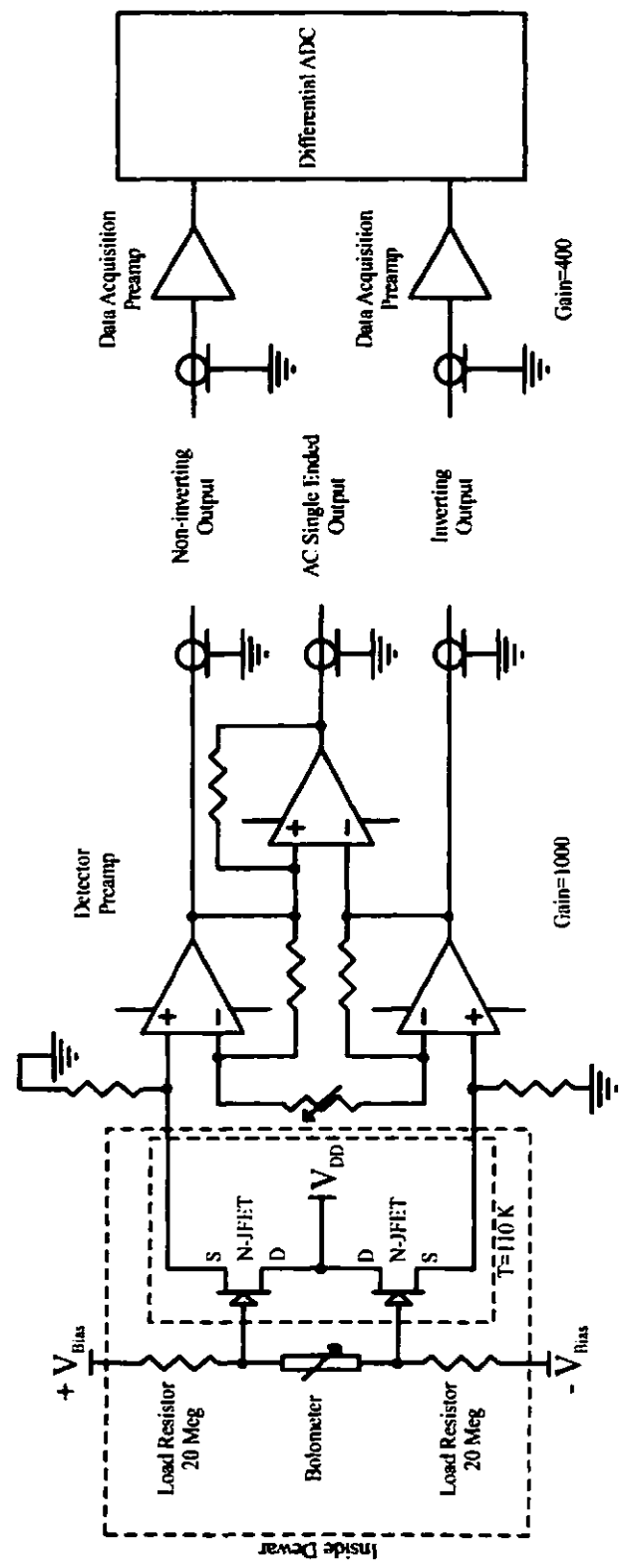

Figure 3.8 : Generalized schematic of the differential circuit design for one detector.

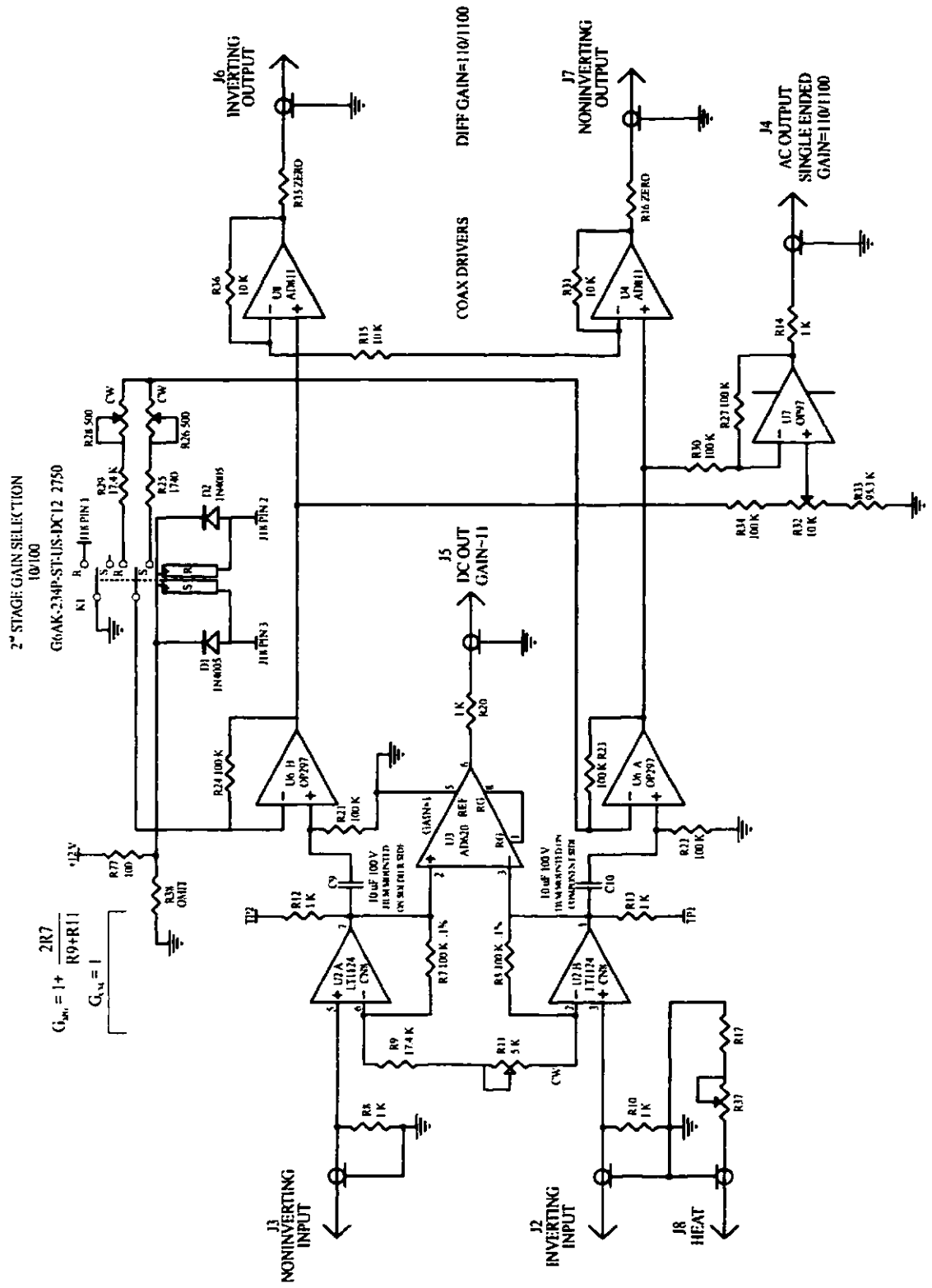

Figure 3.9 : Detailed schematic of the detector preamplifier circuit for one detector.

3.5.2 Electronic System Noise Contribution

Great care was taken in the electronics design to minimize noise levels. The JFETs were chosen for their extremely low noise characteristics. The input op-amps were selected for their high common-mode rejection ratio (CMRR) of 120 dB, and their low input noise voltage and current densities of 3 $nV/\sqrt{Hz}$ and 1.3 $pA/\sqrt{Hz}$ respectively at 10 Hz. The load resistors were mounted to the 0.3 K cryogenic stage in order to minimize their Johnson noise contribution. Also, low noise active bias voltage generators were used to supply the bias current through the bolometers instead of batteries in order to achieve the lowest possible current noise. A schematic of the circuit for one detector is given in Figure 3.10 [2]. Low noise op-amps (input noise voltage density = 3.6 nV/ $\sqrt{Hz}$, input noise current density = 1.1 pA / $\sqrt{Hz}$, at 10 Hz) produce a symmetrical positive and negative bias voltage across the load resistor network, with a total effective noise voltage density (due to the op-amps alone) across the bolometer of ~ 0.2 nV/ $\sqrt{Hz}$ at 10 Hz. A temperature compensated current source is used to generate the input voltage for the op-amps to ensure that the bias voltage does not vary due to the frequent temperature fluctuations in the telescope dome.

For our system we must consider the noise produced intrinsically by the bolometer elements, and the noise produced by the amplifiers and bias network. The entire electrical network is illustrated in Figure 3.11a in terms of ideal resistive elements with associated noise voltage and current generators. The symbols in the figure will be defined in the text as they are needed. First, we will calculate the contributions from the four forms of noise voltages produced by the bolometer elements: Johnson noise, phonon or thermal noise, shot noise, and $1/f$ or flicker noise.

Johnson noise [13] is produced by any resistive element and is described by Equation (3.1), where R is the resistance and T is the resistor temperature. Mather [14] modified the standard Johnson noise equation for a bolometer by taking into account the electrothermal feedback from the bias network. Equation (3.2) is the modified Johnson NEP, where P is the power dissipated by the bolometer element, Z is the dynamic impedance, ω is the signal frequency, and τ=C/G is the physical time constant.

$$e_{nJohnson} = \sqrt{4kTR} \qquad \left(V_{rms}/\sqrt{Hz}\right) . \tag{3.1}$$

$$NEP^2_{Johnson} = 4kTP\left|\frac{Z+R}{Z-R}\right|^2\left(1+\omega^2\tau^2\right) \qquad \left(W/\sqrt{Hz}\right)^2 . \tag{3.2}$$

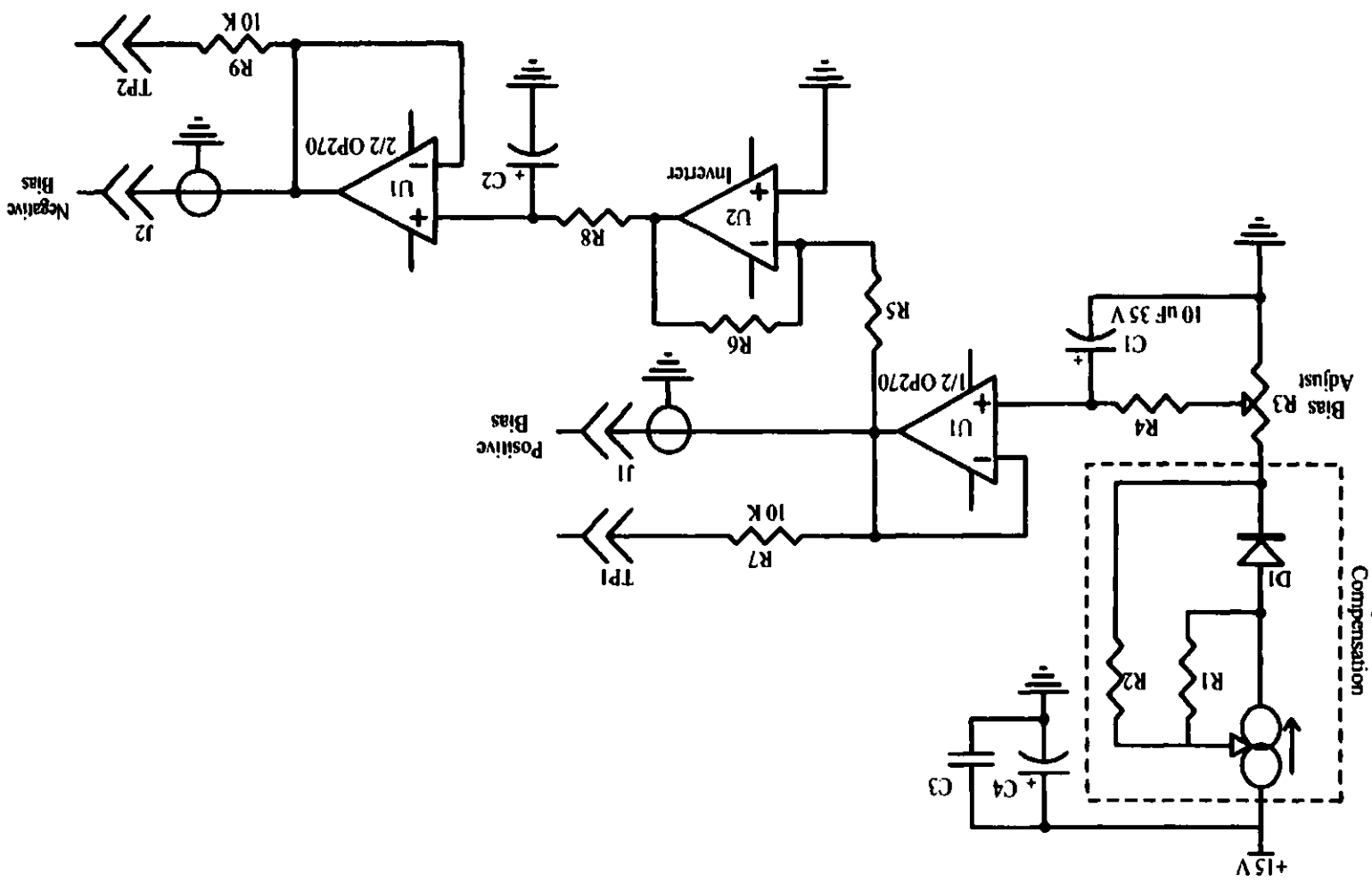

Figure 3.10 : Schematic of the bias voltage supply circuit for one detector.

a.)

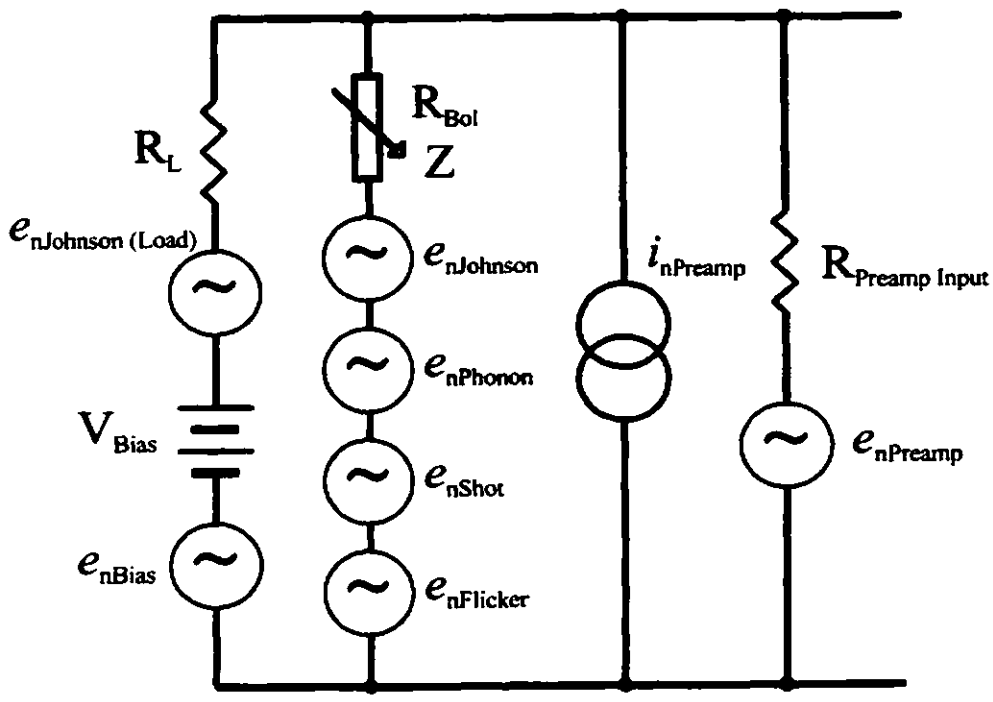

b.)

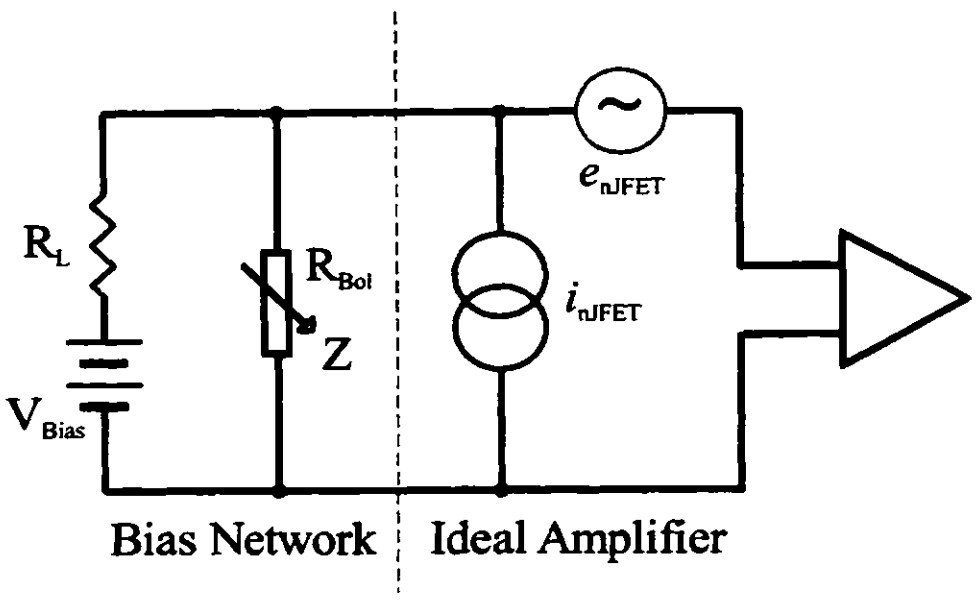

Figure 3.11 : Equivalent noise circuits. a.) Total electrical noise contributions for the bolometer network and amplifier. Symbols are defined in the text. b.) Ideal amplifier with electrothermal feedback from a bias network. i_{nJFET} and e_{nJFET} are the equivalent preamplifier noise current and voltage respectively.

Noise voltages in the bolometer element can also be produced by random fluctuations in heat flow between the element and the sink. The thermal noise analysis of Mather [14] gives this phonon NEP as a function of the thermal conductance of the link, G, the material parameter, β (which is 1 for our brass thermal links), and the bolometer temperature, T. Using the notation $\Delta=1-T_c/T$ where T_c is the sink temperature, the phonon NEP is given in Taylor series form in Equation (3.3).

$$NEP_{Phonon}^2 = 4kGT^2\left[1-\left(\frac{\beta}{2}+1\right)\Delta+\left(\frac{(\beta+2)(3\beta+2)}{12}\right)\Delta^2-\cdots\right]\ \left(W/\sqrt{Hz}\right)^2 . \tag{3.3}$$

Shot noise arises as a result of fluctuations in the flow of charge carriers across a potential barrier. This noise current is expressed as $i_{nShot}=\sqrt{2qI}$, where q is the electron charge and I is the current flowing across the barrier [13]. The electrical connections to a semiconductor bolometer element can produce a barrier to current flow which becomes a source of shot noise. This contact shot noise voltage has been modelled by Mather [14] using Equation (3.4), where Z_{bar} is the contact barrier impedance. Flicker or $1/f$ noise is also present in the detector signal, and has been attributed to fluctuations in charge carrier trapping on the surface of a semiconductor [15]. Precise values for flicker and contact shot noise are difficult to produce from theory due to lack of knowledge about the bolometer contacts. Both of these noise sources show up as excess noise in the detector signal, and are measured directly.

$$e_{nShot}=Z_{Bar}\cdot i_{nShot} . \tag{3.4}$$

The amplifier electronics produce additional noise in the detector signal, which can be expressed in the form of a NEP. The JFETs and amplifier shown in Figure 3.8 can be represented by a single ideal amplifier with associated noise voltage and current generators, as shown in Figure 3.11b. The equivalent noise voltage and current are determined by the following analysis.

The high resistance of the detector ($R_{Bol}\sim 2M\Omega$) necessitates an input device with low input noise current, therefore a JFET was chosen. There are two components of the JFET noise current: a thermal component and a shot noise component. Equation (3.5) gives the thermal component, where R_{GS} is the gate-source resistance, which can be greater than $10^{14}\ \Omega$ for a JFET. This thermal component is simply the current produced by the Johnson noise from the high gate-to-channel resistance, since the channel resistance is

very low and produces a negligible Johnson noise. The shot noise component is given by Equation (3.6), where q is the electronic charge and I_G is the reverse gate current.

$$i_{nThermal} = \sqrt{\frac{4kT}{R_{GS}}} \quad . \tag{3.5}$$

$$i_{nShot} = \sqrt{2qI_G} \quad . \tag{3.6}$$

The shot noise is the dominant noise component. To minimize the input noise current it is therefore necessary to minimize the reverse gate current, which is a function of the reverse junction potential, V_{DD}. V_{DD} is minimized at ~2.5 V, just slightly greater than the pinchoff voltage of the JFET. The JFET drain current, I_D, is set to ~4 mA. At room temperature this gives a reverse gate current, I_G, of ~0.5 pA and a transconductance, g_{fs}, of 0.035 S. Since the current is a strong function of device temperature, the JFETs are operated at T~110 K to further reduce the noise current.

For a JFET, a noise voltage is produced by Johnson noise in the channel resistance. This noise follows the form of Equation (3.1) where the resistance R is replaced by $R_{eq} \sim 0.67/g_{fs}$; the equivalent noise resistance of the JFET, where g_{fs} is the forward transconductance of the device. Johnson noise can be reduced by increasing the forward transconductance (equivalent to increasing the gate area) and/or decreasing the device temperature. The limit to performance enhancement is determined by the increased input capacitance and the decreased carrier mobility at low temperature. The IFN146 dual matched JFETs, with large gate geometry, were selected for the input stage of the preamplifiers based on these considerations.

Two additional sources of JFET noise voltage must be considered: Flicker noise, given by Equation (3.7) where f_1 is the corner frequency and f is the operating frequency, and popcorn noise. Flicker noise is thought to be due to surface defects in the device, while popcorn noise is caused by contamination during the semiconductor manufacturing process. Therefore, the contribution from both these noise sources can be minimised by careful selection of the manufacturer and fabrication process.

$$e_{nFlicker} \approx \sqrt{4kTR_{eq}\frac{f_1}{f^n}} \quad . \tag{3.7}$$

The flicker noise component of the IFN146 has a relatively high corner frequency, f_1, of 1 KHz. The

total JFET noise voltage at any frequency can be expressed from combining the JFET Johnson voltage noise and Equation (3.7) as:

$$e_{nJFET} \approx \sqrt{4kTR_{eq}\left(1+\frac{f_1}{f^n}\right)} \ . \tag{3.8}$$

Following the notation of Mather [14], we can now calculate the total preamp NEP contribution using Equation (3.9), where S is the detector responsivity. The complex form of this equation is due to the electrothermal interaction of the bias network. Typical values for the total JFET noise current and voltage at 50 Hz are 0.4 $fA/\sqrt{Hz}$ and 0.6 $nV/\sqrt{Hz}$, respectively.

$$NEP^2_{Preamp} = i^2_{nJFET}\left|\frac{2ZI}{\frac{Z}{R}-1}\right|^2\left[1+\omega^2\tau^2\left(\frac{Z+R}{2Z}\right)^2\right]+\frac{e^2_{nJFET}}{\left|S^2(\omega)\right|} \qquad \left(W/\sqrt{Hz}\right)^2 \ , \tag{3.9}$$

$$where \quad i^2_{nJFET} = i^2_{nThermal} + i^2_{nShot} = \frac{4kT}{R_{GS}} + 2qI_G \ .$$

Johnson noise from the load resistors must also be taken into account using Equation (3.10) [14]. The noise from the bias voltage generator, e_{nBias}, is 0.2 $nV/\sqrt{Hz}$ at 100 Hz, and is negligible compared to the load resistor Johnson noise.

$$NEP^2_{Load} = \frac{4kT_L}{Z_L}\left|\frac{2ZI}{\frac{Z}{R}-1}\right|^2\left[1+\omega^2\tau^2\left(\frac{Z+R}{2Z}\right)^2\right] \qquad \left(W/\sqrt{Hz}\right)^2 \ . \tag{3.10}$$

The total detector system noise is discussed in the noise analysis section of Chapter 5, where the predicted noise contributions presented above are compared with the measured detector system noise.

[1] Department of Physics, Queen Mary and Westfield College, Mile End Road, London, E1 4NS, UK.

[2] Cochise Instruments Inc., 6304 deMello Street, Hereford, Arizona, 85615, USA.

[3] Chase Research, 35 Wolstenholm Road, Sheffield, S7 1LB, UK.

[4] Infrared Laboratories Inc., 1808 East 17th Street, Tucson, Arizona, 85719, USA.

[5] Naylor, D. A., A. A. Schultz, and T. A. Clark, "Eliminating channel spectra in Fourier transform spectroscopy", *Appl. Opt.* **27**, 2603-2607, 1988.

[6] Ade, P. A. R., "Metal mesh interference filters and their use in metre submillimetre systems", *In Proceedings of Workshop on Bolometers for Submillimetre Space Projects*, Orsay, IAS RS95-02, June 1995.

[7] Amoco Polymers Inc., TORLON/KADEL Parts & Resins, 5300 B Fulton Industrial Blvd., Atlanta, GA 30336, USA.

[8] Martin, D. H., in *Infrared and Millimeter Waves*, Volume 6, Academic Press, New York, Ed. K. J. Burton, 1982, p. 65-148.

[9] Gush, H. P., Halpern, M., and Knotek, S., "Cooled Low-Noise Preamplifier for a Bolometer", *Rev. Sci. Instrum.* **63**, 90-92, 1992.

[10] Low, F. J., "Application of JFETs to Low Background Focal Planes in Space", *Proc. SPIE Infrared Astronomy*, **280**, 56-60, 1981.

[11] Rieke, G. H., Montgomery, E. F., Lebofsky, M. J., and Eisenhardt, P. R., "High Sensitivity Operation of Discrete Solid State Detectors at 4 K", *Appl. Opt.*, **20**, No. 5, 814-818, 1981.

[12] InterFet Corporation, 1000 North Shiloh Road, Garland, Texas, 75042, USA.

[13] Horowitz, P., and Hill, W., *The Art of Electronics* 2nd Ed, Cambridge University Press, New York, 1993.

[14] Mather, J. C., "Bolometer Noise: Nonequilibrium Theory", *Appl. Opt.*, **21**, No. 6, 1125-1129, 1981.

[15] van Vliet, K. M., "Noise Limitations in Solid State Photodetectors", *Appl. Opt.*, **6**, 1145, 1967.

Chapter 4

Closed Cycle Cryogenic System

4.1 Introduction

In order to achieve background photon noise limited operation, the bolometer elements must be cooled to below 1 K. This is well below the bath temperature of ~ 4 K for the bulk liquid ^{4}He. A liquid ^{4}He bath can be cooled to nearly 1 K by pumping, but below this temperature the vapour pressure becomes too low and this method becomes inefficient.

Cooling below the temperatures attainable by pumped ^{4}He fridges can be achieved with Joule-Thomson, pumped ^{3}He, and ^{3}He dilution fridges. However, the following requirements precluded the use of these fridges in our system: Fourier spectrometers are particularly sensitive to vibration (which causes unwanted modulation in the interferogram signal), so detectors with fridges requiring mechanical pumps should not be used. Cooling the large thermal mass of the bolometer units and the associated support structure requires a fridge with a large cooling capacity. Also, the detector dewar has to be a self contained unit small enough to mount on the FTS, and require minimal maintenance. Finally, the cost of the system had to be kept low.

The only system that meets these requirements is a dual stage ^{4}He:^{3}He closed cycle refrigerator with vibration free adsorption pumps. A closed cycle ^{4}He fridge is necessary in order to pre-cool the collecting vessel of the ^{3}He fridge to below the critical temperature of ^{3}He so that it will condense. It is also much more efficient to pump on a small amount ^{4}He to cool the ^{3}He vessel than to pump the entire bulk ^{4}He bath to cool it to below 3.3 K. A closed cycle system is required for the ^{3}He fridge to prevent loss of the much more expensive ^{3}He (typically ~ 1000 times more expensive per unit liquid volume than ^{4}He).

There are several properties of ^{3}He that allow it to be pumped efficiently to 0.3 K: ^{3}He has a significantly higher vapour pressure than ^{4}He at temperatures below its critical temperature of 3.3 K [1]; at 1 K the ratio of the vapour pressures P(^{3}He):P(^{4}He) is 74 but at 0.5 K the ratio becomes 10^4. Some key parameters of liquid ^{3}He and ^{4}He are given in Table 4.1. Vapour pressure curves for both isotopes are given in Figure 4.1 [2], where the practical lowest temperatures obtainable by pumping on an open bath are shown as dots. In addition, the specific heat of ^{3}He is greater than that of ^{4}He below 1.5 K so it acts as a better heat reservoir in

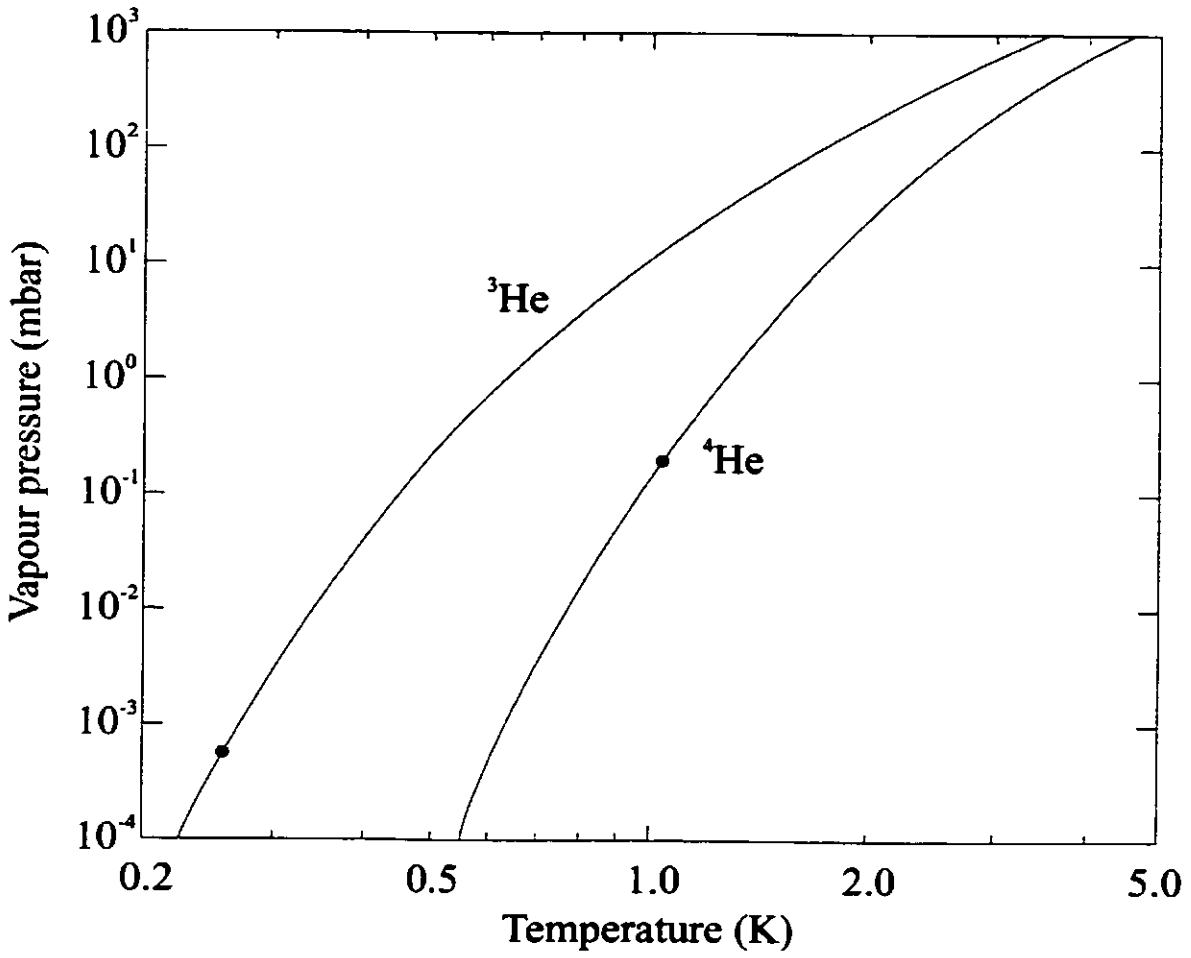

Figure 4.1 : Vapour pressure as a function of temperature for ^{3}He and ^{4}He [2]. The practical lower temperature limits achievable by pumping a liquid bath are indicated by dots on the curves.

this temperature range. The specific heat of ^{3}He also varies less with temperature than that of ^{4}He so less liquid is lost to evaporation in cooling the bath to low temperatures. Phase diagrams for ^{4}He and ^{3}He are given in Figure 4.2 [3]. From the phase diagrams it can be seen that whereas ^{4}He becomes superfluid below 2.18 K, which creates containment and possible heat flow problems, ^{3}He has a maximum superfluid transition temperature of 2.5 mK.

Table 4.1 : Thermal Properties of Liquid Helium

	^{3}He	^{4}He
Boiling Point at 1 Bar (K)	3.19	4.21
Critical Temperature (K)	3.32	5.20
Critical Pressure (Bar)	1.16	2.28
Latent Heat of Evaporation (kJ/l)	0.48	2.56
Maximum Superfluid Temperature (K)	$2.5 \cdot 10^{-3}$	2.177
Gas (NTP) to Liquid (1 K) Volume Ratio	662	866
Specific Heat at 0.3 K (J/mol·K)	3	$2 \cdot 10^{-3}$
Molar Volume at 0 K (cm^3/mol)	36.84	27.58

The closed cycle cryogenic refrigerator used in this detector is a commercial unit manufactured by Chase Research [4]. Included with the fridge was an electronics unit that enabled manual operation of the cooling cycle. As the cooling cycle is a sensitive, time consuming operation, it was decided that an automatic cycling system would provide the most reliable operation and most efficient use of limited telescope time. Design of the automatic cryogen cycling electronics and associated control software is given in the following sections.

4.2 Closed Cycle Fridges

The design of the fridge system is shown schematically in Figure 4.3. The system is composed of two independent closed cycle fridges, one operating on ^{4}He, the other on ^{3}He, both consisting of baths pumped by carbon adsorption pumps. These pumps use the extremely large (many m^2/g) surface area of activated charcoal granules to adsorb the gas. A chart of the minimum attainable temperature of a ^{3}He bath pumped by 20 g of activated charcoal as a function of the thermal load is given in Figure 4.4 [5]. From this graph it is evident that for a desired temperature of 0.3 K, a 20 g charcoal pump can provide 200 μW of cooling power.

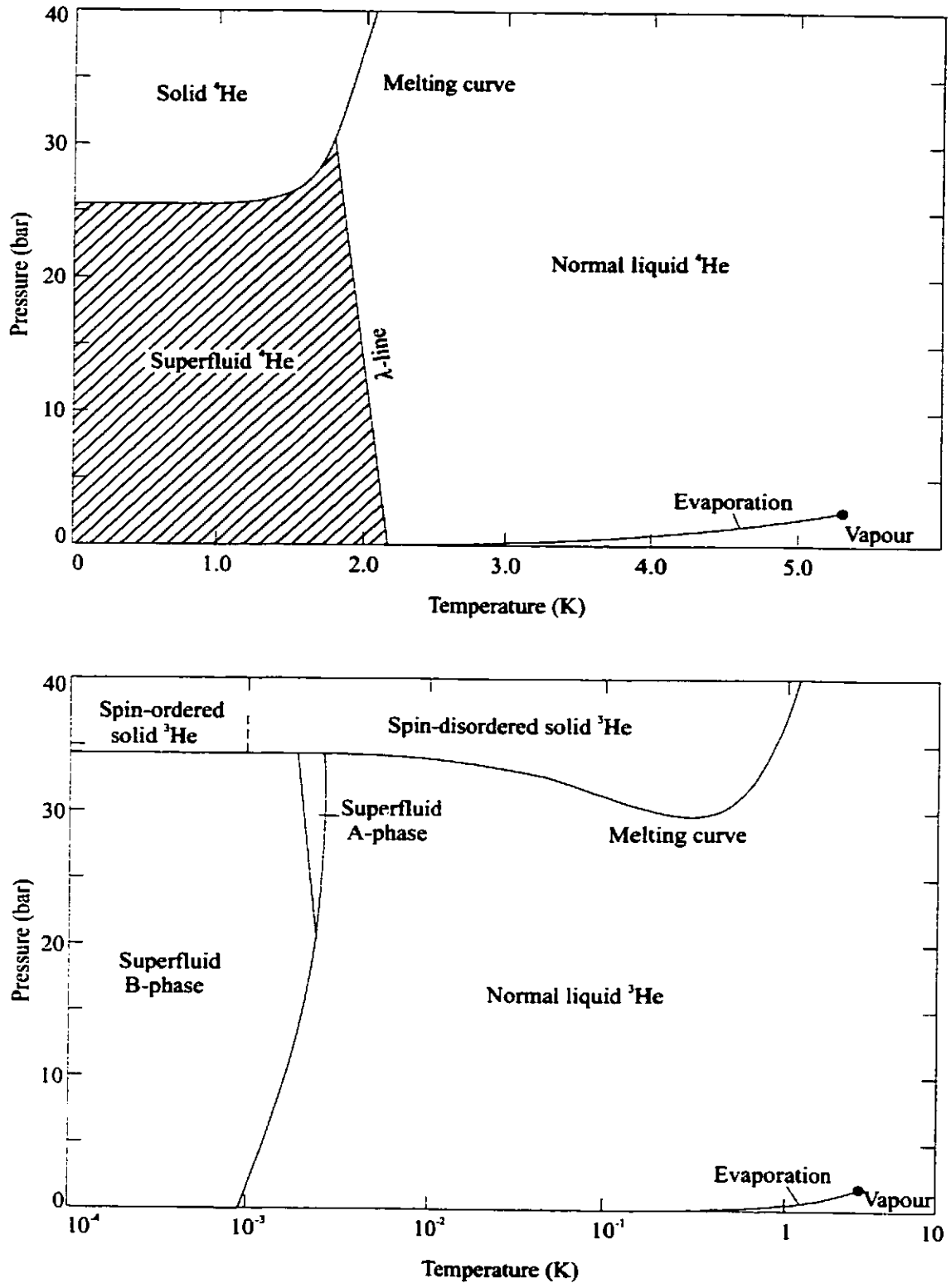

Figure 4.2 : Phase diagrams for ^{4}He and ^{3}He [3]. Note the logarithmic temperature axis for the ^{3}He diagram.

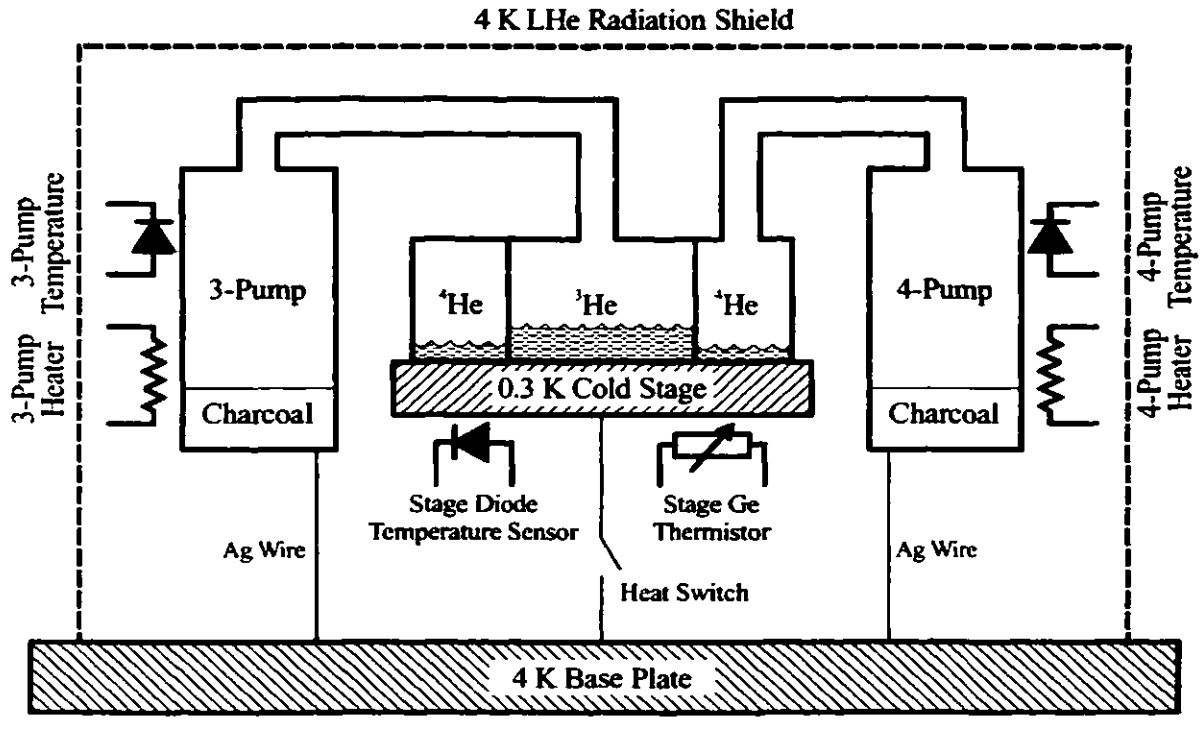

Figure 4.3 : Schematic of the cryostat system.

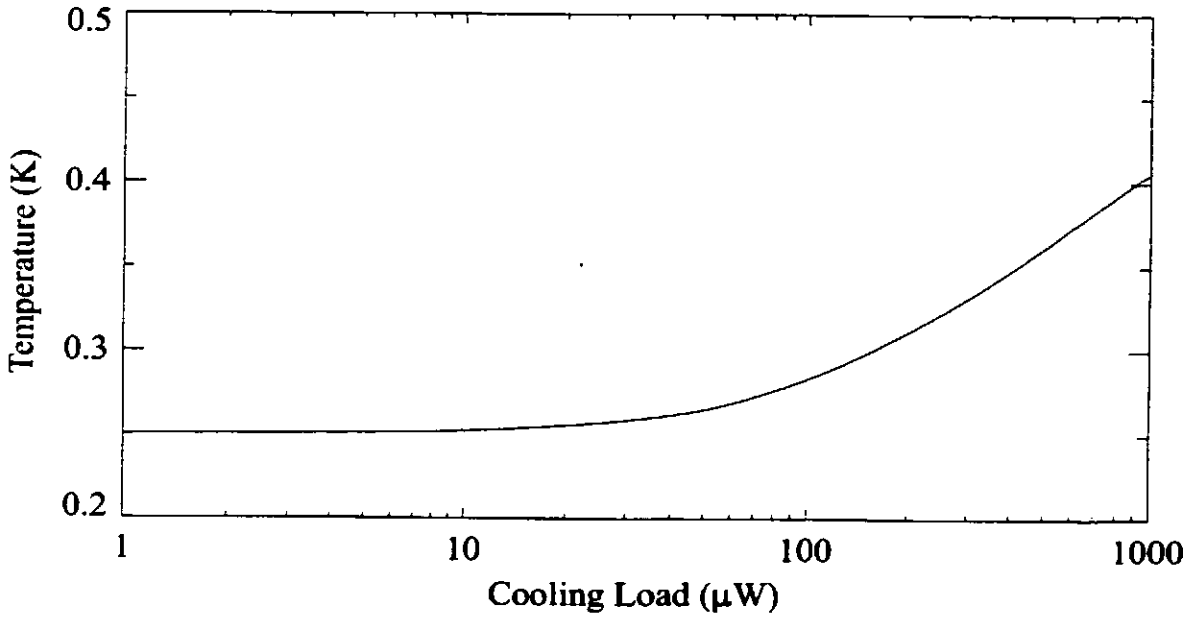

Figure 4.4 : Minimum temperature of a 3He bath pumped by a 20 g charcoal adsorption pump as a function of thermal load [5].

The bath of the ^{3}He fridge is a small cylindrical vessel suspended from the 4 K base plate by a thin walled (0.125 mm) stainless steel tube which connects it to the ^{3}He pump mounted on the base plate (see Figure 3.2). The bath of the ^{4}He fridge is a cylindrical vessel concentric with, and thermally connected to, the inner ^{3}He vessel. A second tube connects this vessel to the ^{4}He pump. The ^{4}He pump (from now on referred to as the 4-pump) is a small canister containing carbon granules and 5 STP litres of ^{4}He gas which corresponds to a pressure of ~6 MPa at room temperature, or a volume of ~6 ml of liquid at 1 K. Similarly, the 3-pump contains 3 STP litres of ^{3}He (~4.5 ml liquid at 1 K). Both pumps are mounted to the 4 K base with silver wires whose dimensions determine the thermal conduction, and therefore the pumping rate, for each pump. Each pump is heated with a resistor which can dissipate ~2 W to drive any adsorbed gas out of the carbon at the beginning of the pumping cycle. A silicon diode temperature sensor (DT470 [6]) is fitted to each pump to monitor the cooling process. The temperature of the stage is monitored with a diode temperature sensor for temperatures above 1 K, and a Ge thermistor (GR100 [6]) for low temperatures.

A solenoid driven clamp mounted on the 4 K base plate acts as a mechanical heat switch between the stage and the main helium reservoir (see Figure 3.2). When activated, the clamp grips a gold plated copper strip extending from the stage, which provides a direct thermal link to the bulk 4He reservoir and assists in pre-cooling the stage.

4.3 Electronics

The principal advantage of the closed cycle system is that its operation is easily automated. The pumps are controlled by simply applying current to their heaters, and the cooling process is monitored by measuring the temperature of the pumps and the cold stage. An electronic interface unit (referred to as the cycle box) was constructed to drive the heaters, relays, and temperature sensors, and to amplify the sensor signals. The cycle box is controlled with a computer by means of an inexpensive, general purpose data acquisition and control module (AD612 [7]). This module was modified to provide 6 channel, 12-bit analog-to-digital conversion and 8 digital I/O lines using a single PC parallel port.

The current supplies and signal buffers for the pump and stage diode temperature sensors are shown in Figure 4.5. The stage diode current supply can be disabled when the sensor is not being used to reduce the thermal loading of the stage. The signals are fed into the AD612 unit, as well as to coax connectors on the back of the cycle box for direct measurement.

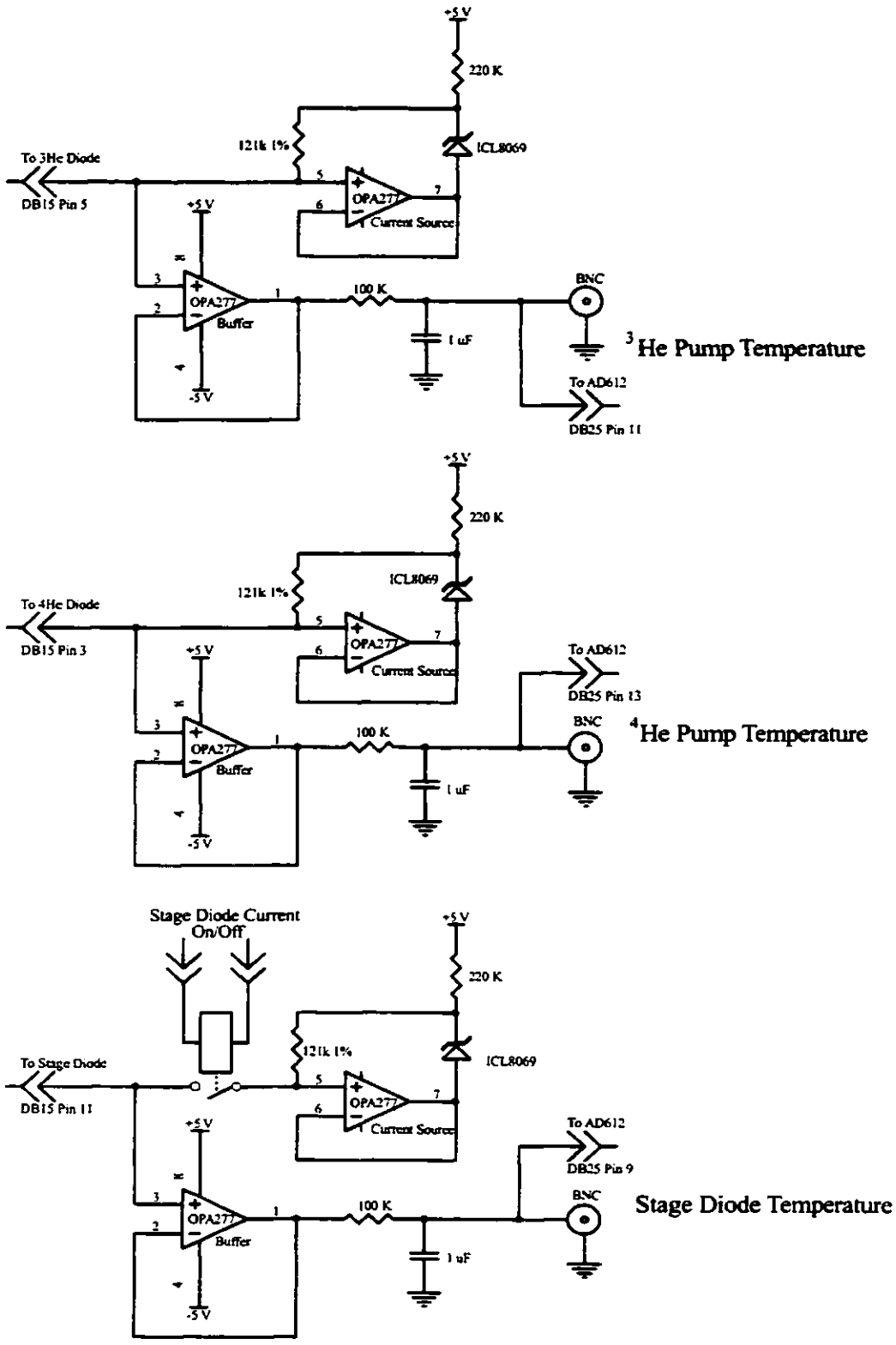

Figure 4.5 : Schematic of the current supplies and signal buffers for the pump heater and stage diodes.

For precise temperature measurements below 1 K, the stage Ge sensor (GRT-100 [6]) is used. In order to minimize self heating and thermal loading of the stage, the measurement current passed through the sensor must be small. Since a small DC current would provide a very low signal-to-noise ratio measurement, the sensor was excited with a small AC current and the resulting signal was synchronously detected. This circuit, shown in Figure 4.6 [8], allows the use of a very small 50 nA rms current to drive the Ge thermistor, producing a negligible ~50 pW rms of self heating. The driving frequency is set at 250 Hz to avoid 1/f and other noise sources. The amplified signal is then digitized by the AD612 unit and averaged by the control software to prevent glitches.

Electronic control of the heat switch solenoid, pump heaters, and stage diode current is provided by logic driven relays, shown in Figure 4.7, which are controlled using the I/O lines of the AD612. Manual override switches are mounted on the cycle box, and indicator LEDs to show the status of the various system components (pumps, heat switch, heaters, etc.).

4.4 Cycling Software

It is desirable to be able to cool the detector and cycle the cryogenic system automatically between observing runs so as not to waste telescope time or manpower. To this end, a cycling program was written in C++ to run on an IBM PC interfaced with the cycle box. Appendix 6.2 contains the cycling software code and a typical configuration file. The software converts the digitized sensor signals from the cycle box to temperature, and intelligently controls the temperature and operation time of the pumps in order to ensure complete and efficient recycling of the fridges. All values from the temperature sensors are averaged (20 to 30 samples each) by the software in order to avoid any noise spikes generated by the switching of the pump heater currents. The program can be set to start after a time delay so that the recycling completes just before the next observing shift. A real time graphical display of the cooling process is provided, and all the temperature values are written to a log file. A typical plot produced by the cycling software during a recycling sequence is shown in Figure 4.8. A flow chart of the control logic used by the cycling software is given in Figure 4.9, where hexagons represent conditional statements, and rectangles represent actions. Execution flows from top to bottom if a condition is false, and from left to right if true, and the entire loop is checked repeatedly until the cycle is complete or the operator intercedes. The operation of the pump heaters and deactivation of the

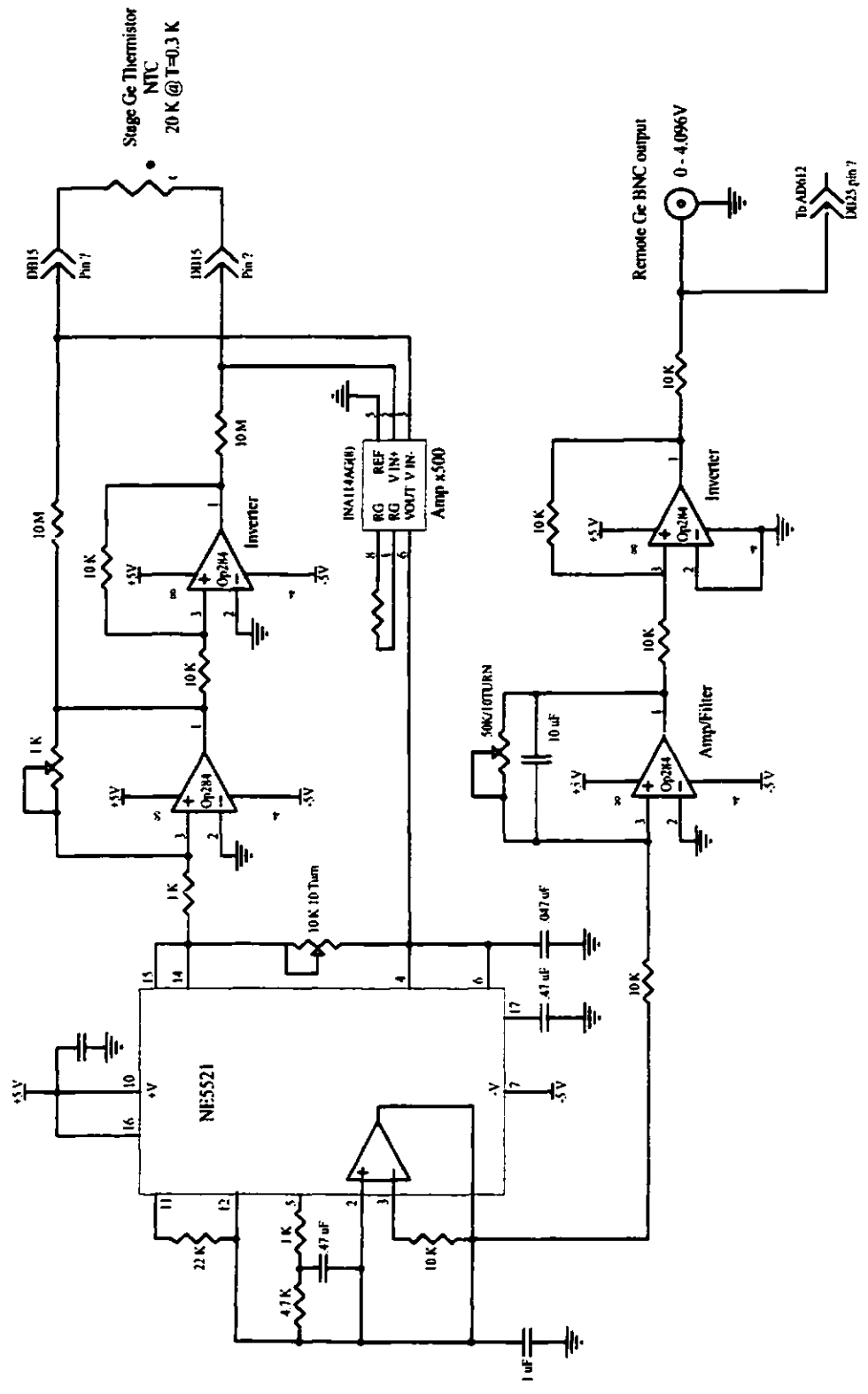

Figure 4.6 : Schematic of the phase sensitive detector circuit used to measure the stage Ge temperature sensor.

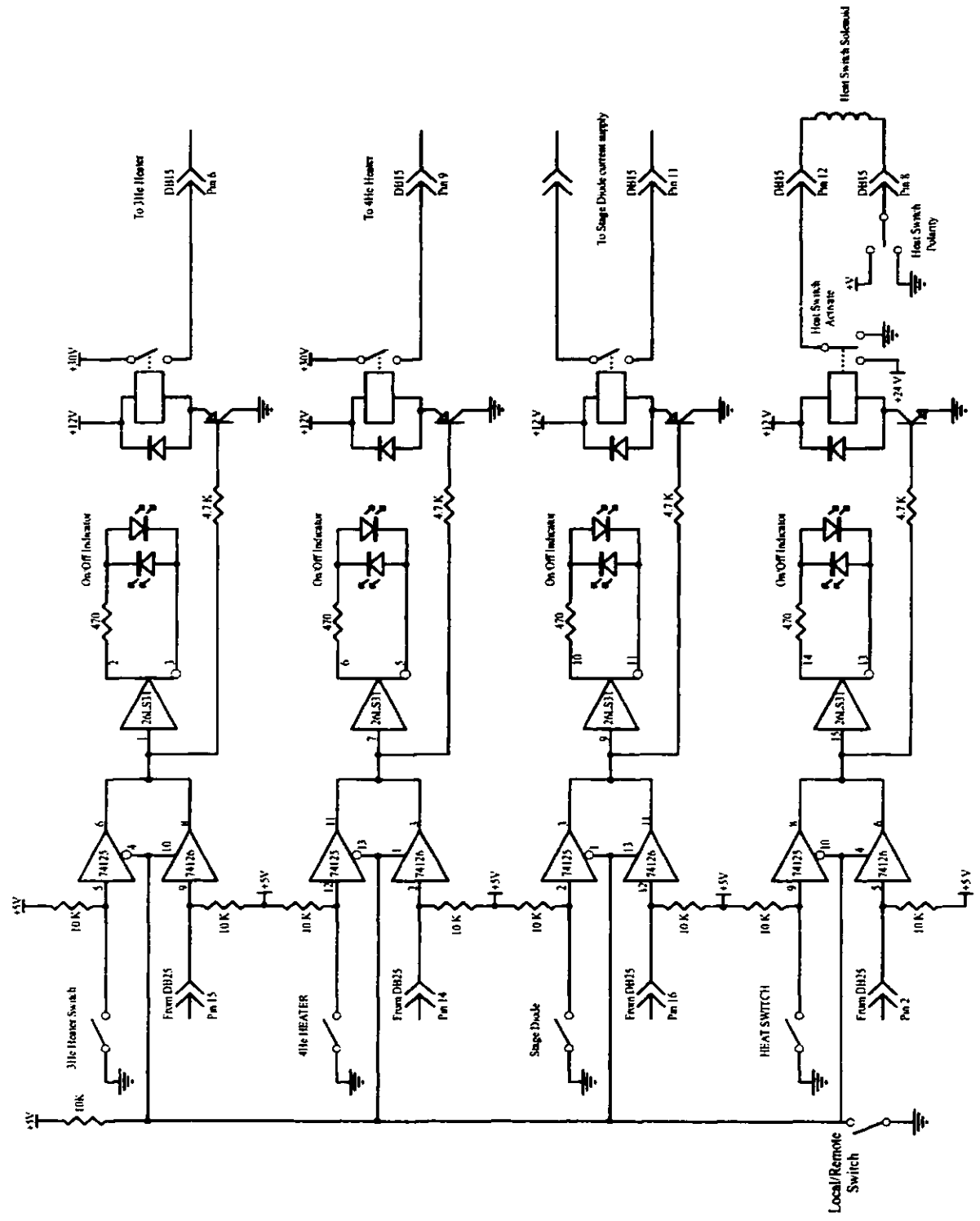

Figure 4.7 : Schematic of the cycle box switches, indicators, and relays for driving the pump heaters, heat switch solenoid, and stage diode current.

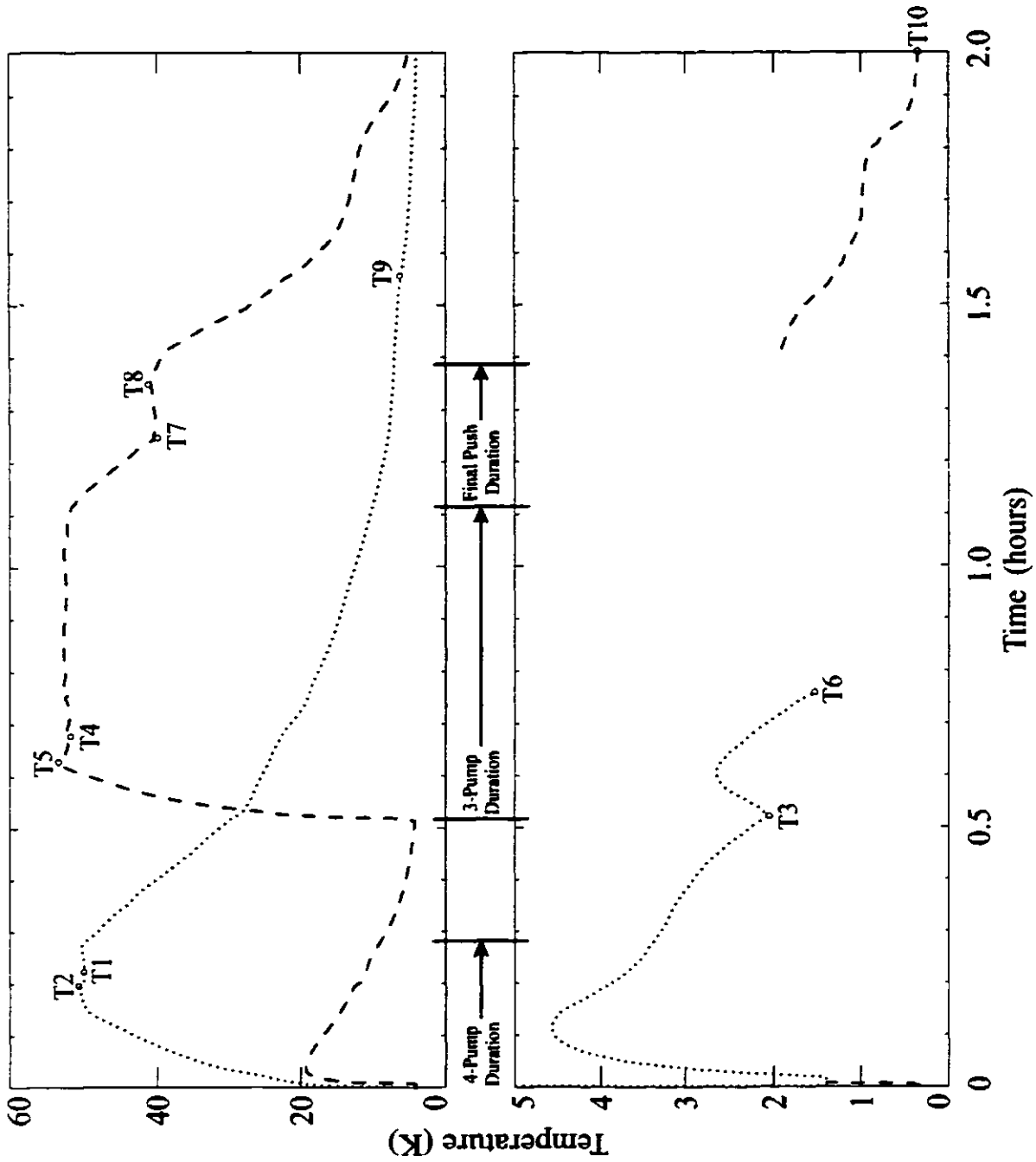

Figure 4.8 : A typical recycling log. The top graph shows the pump temperatures, where the dotted line is the 4-pump, and the dashed line is the 3-pump. Bottom graph shows the stage temperature, where the dotted line is the diode thermometer, and the dashed line is the Ge thermometer.

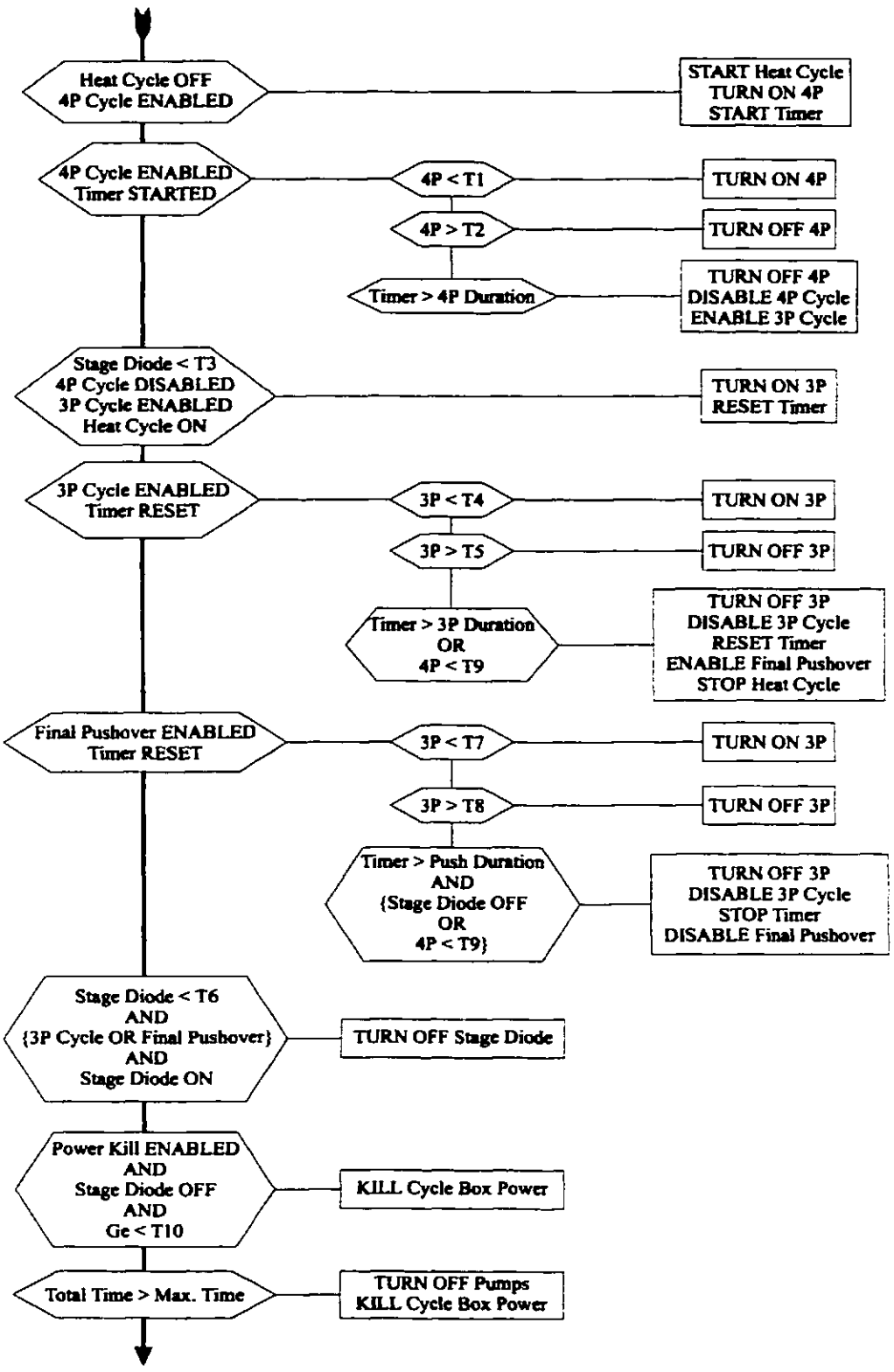

Figure 4.9 : A flow chart of the control logic used by the cycling software to recycle the ^{3}He and ^{4}He pumps. Hexagons represent conditional statements, rectangles represent actions. Execution flows from top to bottom if a condition is false, and from left to right if true.

temperature sensors occurs at various temperature and time set points that are easily modified to fine tune the recycling process. The temperature set points are referred to in the flow chart as T1 through T10, and are labelled in Figure 4.8. The operation times of the 4-pump and 3-pump heaters are limited by the time set points referred to as the 4P, 3P, and Final Pushover durations in the flow chart and the recycling log plot. Typical values for the set points are contained in the configuration file given in Appendix 6.2.

4.4.1 Description of Cycling Procedure

The pre-cooling process involves pumping the dewar vacuum space to 10^{-5} Torr, engaging the heat switch, and then filling both the nitrogen and bulk helium vessels with LN_2 to cool the system (to 73 K on Mauna Kea). The heat switch is used to provide a conduction path to the well isolated cold stage which would otherwise take days to cool. After the system has been allowed to settle at LN_2 temperature for an hour, the bulk helium vessel is emptied of LN_2 and then filled with LHe. Once the bulk helium vessel is filled, and the stage diode is measured to be at LHe temperature, the heat switch is opened to allow final cooling of the cold stage.

The cold stage is now at ~ 4 K which is well below the critical temperature of 5.2 K for the ^{4}He gas in the 4-pump. The 4-pump heater is activated and gas is driven out of the charcoal and into the outer collecting vessel where it condenses. The temperature of the 4-pump is held between the set points T1 and T2 which typically provide a hysteresis of ~ 1 K. When all of the gas is liquified, the heater is turned off and the pumping action of the 4-pump begins. Since there is no direct indication of when all the ^{4}He has liquified (except for a decrease in the slope of the stage temperature curve due to the reduction in flow of hot ^{4}He gas), the heater is turned off after it has been on for a time greater than the 4P duration set point. When the 4-pump has lowered the temperature of the cold stage to below the critical temperature of 3.3 K for ^{3}He, the inner collecting vessel will collect liquid ^{3}He and the 3-pump heater can be activated. In practice, T3, the temperature of the stage at which the 3-pump is activated, is set at 2.2 K to allow the 4-pump to extract as much heat from the stage as possible without allowing the ^{4}He to become superfluid. The heat of the incoming ^{3}He gas, and latent heat of vaporization as the ^{3}He liquifies, raises the temperature of the stage slightly which increases the boil-off rate of the collected ^{4}He. This can be inferred from the plot by the hump in the stage diode temperature and the change in slope of the 4-pump temperature. It is critical that all the ^{4}He is evaporated before the 3-pump heater

is deactivated, or too much ^{3}He will be wasted by cooling the ^{4}He bath. There is also the possibility that the remaining ^{4}He will be cooled to below its superfluid transition temperature, creating a potential heat flow problem due to the resulting superfluid flow. To ensure that all the ^{4}He has evaporated, the 3-pump heater is left on for a set amount of time (3-pump duration ~30 min) or until the temperature of the 4-pump falls below a set temperature (T9 ~ 6 K).

Once the 3-pump heater is deactivated, the 3-pump cools the stage to its ultimate temperature of ~0.3 K. At the end of the cycling process, power to the temperature sensors is cut off to prevent unnecessary loss of condensed ^{3}He, and power to the cycle box is also cut off to prevent any possible accidental reactivation of the pumps or heat switch.

A typical recycle (not the first cool-down cycle) consumes approximately 0.9 litres of bulk liquid helium, and a negligible amount of liquid nitrogen. The collected ^{3}He has a hold time of approximately 30 hours depending on the loading of the detector. Before the bath is exhausted, the pumps can be recycled by turning on the 4-pump heater which forces over ^{4}He gas and evaporates any remaining liquid ^{3}He. The operation of the pumps is then repeated as described above.

At the end of an observing shift, the bulk cryogens in the dewar are replenished, and the control software is set to initiate after a suitable delay so that the system has just finished recycling at the beginning of the shift on the next day. In this way, the detector remains at operating temperature for the maximum amount of time during the shift.

[1] Pobell, F., *Matter and Methods at Low Temperatures*, 2nd ed., Springer-Verlag, New York, 1996, p. 110.

[2] Pobell, *ibid.*, p. 21.

[3] Pobell, *ibid.*, p. 16.

[4] Chase Research, 35 Wolstenholm Road, Sheffield, S7 1LB, UK.

[5] Pobell, *ibid.*, p. 116.

[6] Lakeshore Cryotronics Inc., 64 East Walnut Street, Westerville, Ohio, 43081-2399, USA.

[7] AD612 DAS module, Accu-Data, Suite C-178 297 Route 72 West, Manahawkin, New Jersey 08050-2890, USA.

[8] Tompkins, G., Technical Services, University of Lethbridge, 4401 University Drive, Lethbridge, Alberta, T1K 3M4, Canada.

Chapter 5

Detector Performance

5.1 Introduction

This chapter describes the five sets of laboratory tests which have been performed on the ^{3}He dual polarization bolometric detector system: beam profile measurements, frequency response measurements, V-I performance, noise performance and spectral performance. The data collection, analysis and results for each set of tests are described in separate sections as listed below:

- **Section 5.2** : Beam profile measurements are analysed to determine if there are any serious misalignments of the internal optics.
- **Section 5.3** : The frequency response of the detectors are measured to determine the maximum possible modulation frequency of the FTS, and to verify the heat capacity of the bolometer elements.
- **Section 5.4** : The detector V-I curves are modelled to determine bolometer parameters such as the thermal conductance, bolometer housing temperature and background radiant power loading. The V-I data is manipulated in following sections to calculate the NEP for each detector as a function of bias current, which allows the optimum bias setting to be determined for a given filter band.
- **Section 5.5** : The detector responsivity is calculated from the V-I curves, and modelled to provide the system optical efficiencies.
- **Section 5.6** : The measured detector noise performance is compared to the noise performance predicted from the V-I analysis. The system NEPs determined by four different methods are compared, and the optimum bias point corresponding to the minimum NEP for each detector is determined.
- **Section 5.7** : Spectra measured with the detector in conjunction with the FTS are analysed to determine the full system NEP. The spectral performance is compared with the previous detector system and with a current state-of-the-art system.
- **Section 5.8** : Concluding remarks and a summary of the detector parameters are given.
- **Section 5.9** : Future considerations and possible improvements are discussed.

The detector system resides permanently at the JCMT to avoid the expense of shipping and the possibility of damage during transport. Consequently, access to it is limited to the engineering and commissioning time allocated at the beginning of an observing run. The tests described in this chapter were performed over this period during the 1997 and 1998 runs.

5.2 Beam Profile

In order to calculate the throughput of the detector system, a quasi-far-field blackbody point source was used to map out the beam profile. The source was an electric cigarette lighter element held at a temperature of ~1000 K determined by its red colour [1]. This source was placed behind a 290 K chopper blade to provide a 20 Hz modulated signal. The blackbody assembly was mounted on a stand that could be positioned vertically and horizontally. The detector and source were configured as illustrated in Figure 5.1. This enabled horizontal and vertical scans to be taken perpendicular to, and passing through, the optical axis of the detector. The distance between the source and detector window was 287 ±1 cm, and the samples were taken in 1° (25 mm) increments along the vertical and horizontal axes. In order to obtain measurements in a reasonable time and with a high signal to noise ratio, the wide band (5 to 35 cm^{-1}) filter, with its higher bandwidth and throughput, was used for the beam profile measurements. The peak-to-peak voltage of the detector signal, V_{pp}, was measured with an oscilloscope as a function of angle, for each of the four canonical iris diameter settings. The iris settings for the various filter bands (the filter band designations are given in Chapter 3) are typically chosen to match the detector beam to the diffraction limited beam of the telescope. These settings were different in the two years , as shown in Table 5.1, partly due to a mechanical misalignment in 1997, and partly to a decision in 1998 to use larger aperture settings to increase the throughput. All the beam profile data, however, were collected using the 1997 aperture settings.

Table 5.1 : Aperture Diameter / Filter Band Combinations

Filter Band Designation	Typical Diffraction Limited Aperture Diameter (mm)	1997 Aperture Diameter (mm)	1998 Aperture Diameter (mm)
350s	21	20	30
350l	21	20	30
450	27	24	40
750	47	-	65
850	47	44	65
1100	65	-	65
1400	65	62	-
Open	65	62	-

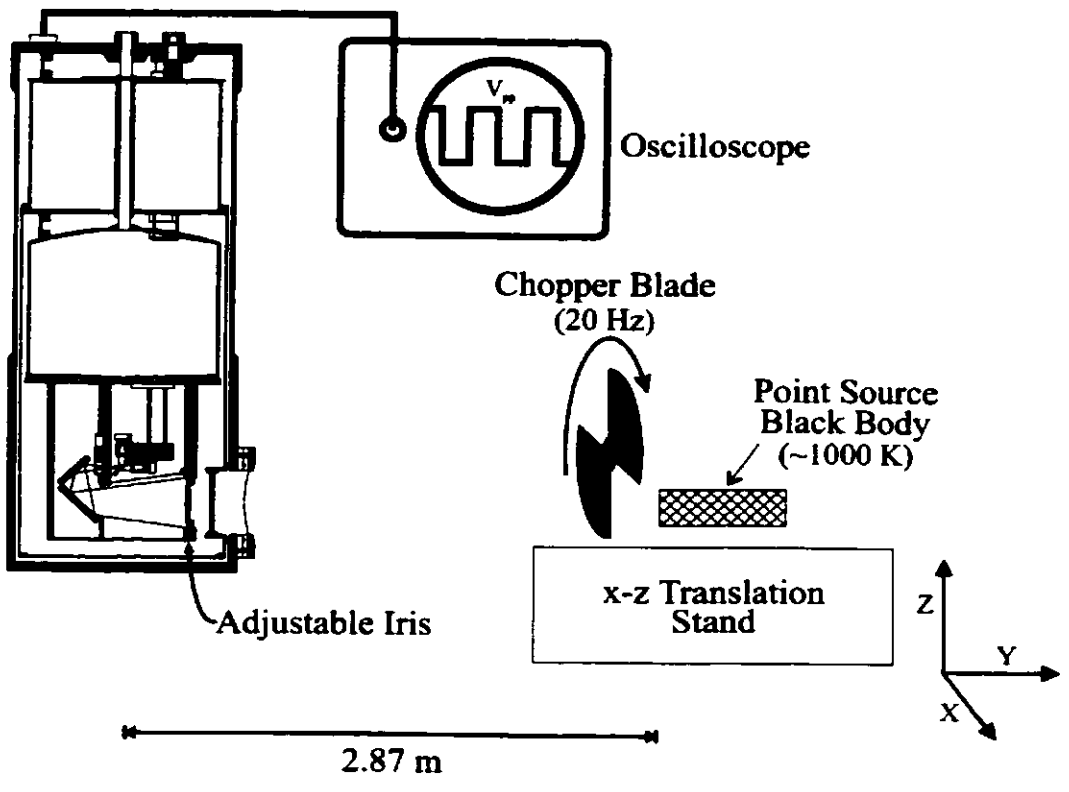

Figure 5.1 : Experimental setup for the beam profile tests.

5.2.1 Analysis

Whereas the Fraunhofer diffraction pattern produced by monochromatic radiation incident on a circular aperture is an Airy function [2], the diffraction pattern produced by broadband radiation represents a superposition of Airy functions with a range of widths. Consequently, the diffraction pattern produced by the wide spectral band (5 to 35 cm^{-1}) is not described by a simple Airy function. For simplicity, the assumption was made that the overall beam pattern would be Gaussian in shape. IDL code was written to perform nonlinear least squares fitting of a single component Gaussian with DC offset to each data set. The fitting procedure returned the widths and relative amplitudes of the fitted Gaussian curves for each profile.

5.2.2 Results

The horizontal and vertical profile data are shown in Figures 5.2 and 5.3, respectively. From the graphs it is apparent that single component Gaussians (lines) are well matched to the beam profile data (symbols) for each aperture setting. It can be seen that the amplitudes decrease with decreasing aperture diameter. There is a slight increase in the beams widths with decreasing aperture, which is not obvious in the figure. Also, the centres of the horizontal and vertical profiles do not coincide exactly with the optical axis of the detector (see Figure 3.1), which is at the origin of the plot scales.

When viewing a distant source, the beam, as seen by the detector, has two components: one determined by the *f*-number of the system, and another produced by diffraction at the iris aperture. We would therefore expect to see increased broadening of the beam profiles as the aperture diameter is decreased, due to the increased effects of diffraction. We can calculate the theoretical dependence of the beam width on aperture diameter by the following analysis: Since wide-band radiation produces a range of diffracted angles, a simplification was made by calculating the beam width for the weighted average wavelength $\overline{\lambda}$ given in Equation (5.1). In this equation, $B_{(\lambda,T)}$ is the Planck function, which is a function wavelength, λ, and source temperature, T. For the wide band filter and our blackbody source, $\overline{\lambda}$ is approximately 500 μm.

$$\overline{\lambda} = \frac{\int B_{(\lambda,T)} \cdot \lambda d\lambda}{\int B_{(\lambda,T)} d\lambda} . \qquad (5.1)$$

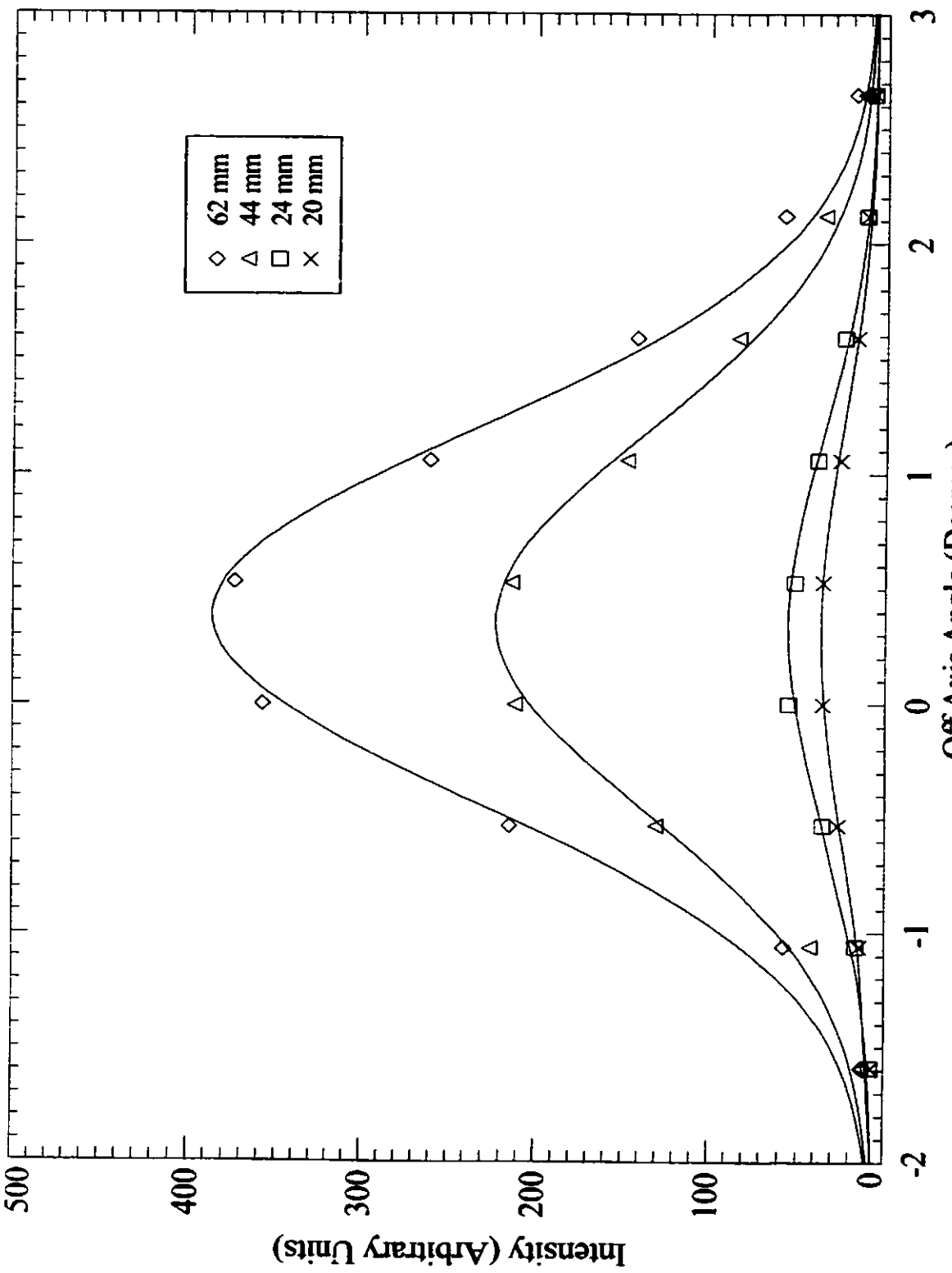

Figure 5.2 : Horizontal beam profile data (symbols) and single component Gaussian fits (lines) as a function of aperture size.

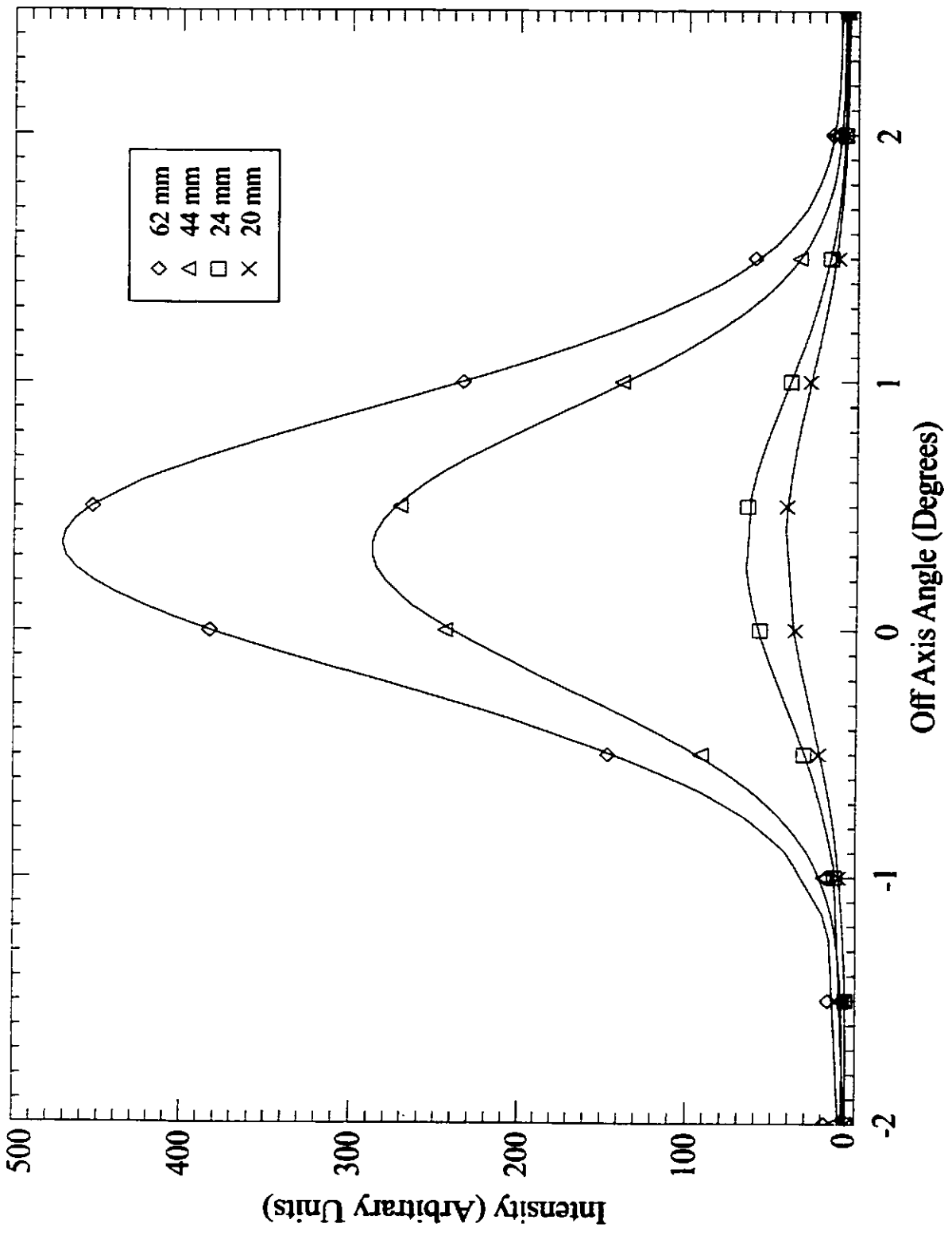

Figure 5.3 : Vertical beam profile data (symbols) and single component Gaussian fits (lines) as a function of aperture size.

The angular width of the beam can then be approximated by Equation (5.2) where ϕ is the aperture diameter, θ_{Diff} is the angular dispersion caused by diffraction at a circular aperture, and θ_{f35} is the angular size of the *f*/35 beam. Figure 5.4 shows the FWHM of the fitted Gaussians for the four apertures. The lines are the best fits of the theoretical Equation (5.2) obtained by varying parameters χ and ψ. The data points exhibit the expected angular dependence on aperture size, within the limits of this crude model.

$$\theta = \sqrt{\theta_{f/35}^2 + \theta_{Diff}^2} \quad .$$
$$\theta = \chi \cdot \sqrt{\left(\frac{\psi}{35}\right)^2 + \left(\frac{1.22\lambda}{\phi}\right)^2} \quad . \tag{5.2}$$

An examination of Figure 5.3 shows that the vertical scans for each aperture are narrower than the corresponding horizontal scans. Since the difference appears for each aperture setting, we assume that there must be a vignetting of the beam somewhere between the bolometer feed horns and the iris, probably within the internal optics near the focal plane of the field lens. As was described in section 3.3, the supporting structure of the internal optics is necessarily minimal to reduce heat transfer from the ambient surroundings to the internal cooled stage. While differential contraction of the various structures was taken into account in the design of the system, there is inevitably some distortion that occurs during cooling. Consequently, the vignetting may be due to a temperature induced misalignment of two or more of the apertures in the optical path (see Figure 3.2). The detector horn apertures and the 33 cm^{-1} edge filter aperture are particularly prone to misalignment due to their small size and the lack of a direct mechanical connection between them.

In order to calculate the efficiency of our elliptical beam as compared to an ideal circular Gaussian beam, the horizontal and vertical profiles were combined to construct a 2-dimensional elliptical Gaussian profile as shown in Figure 5.5. In this analysis the 44 mm aperture profiles were used since this aperture is the least affected by diffraction and vignetting effects. The power incident on the detector is proportional to the throughput of the system, which is proportional to the cross-sectional area of the beam. As a result, the efficiency of an elliptical Gaussian beam, as compared to a circular one with radius equal to the semimajor axis, r, of the ellipse, is given by Equation (5.3) where *e* is the eccentricity of the elliptical beam cross-section.

$$\eta_\Omega = \frac{P_{elliptical}}{P_{circular}} = \frac{\pi r^2 \sqrt{1-e^2}}{\pi r^2} = \sqrt{1-e^2} \quad . \tag{5.3}$$

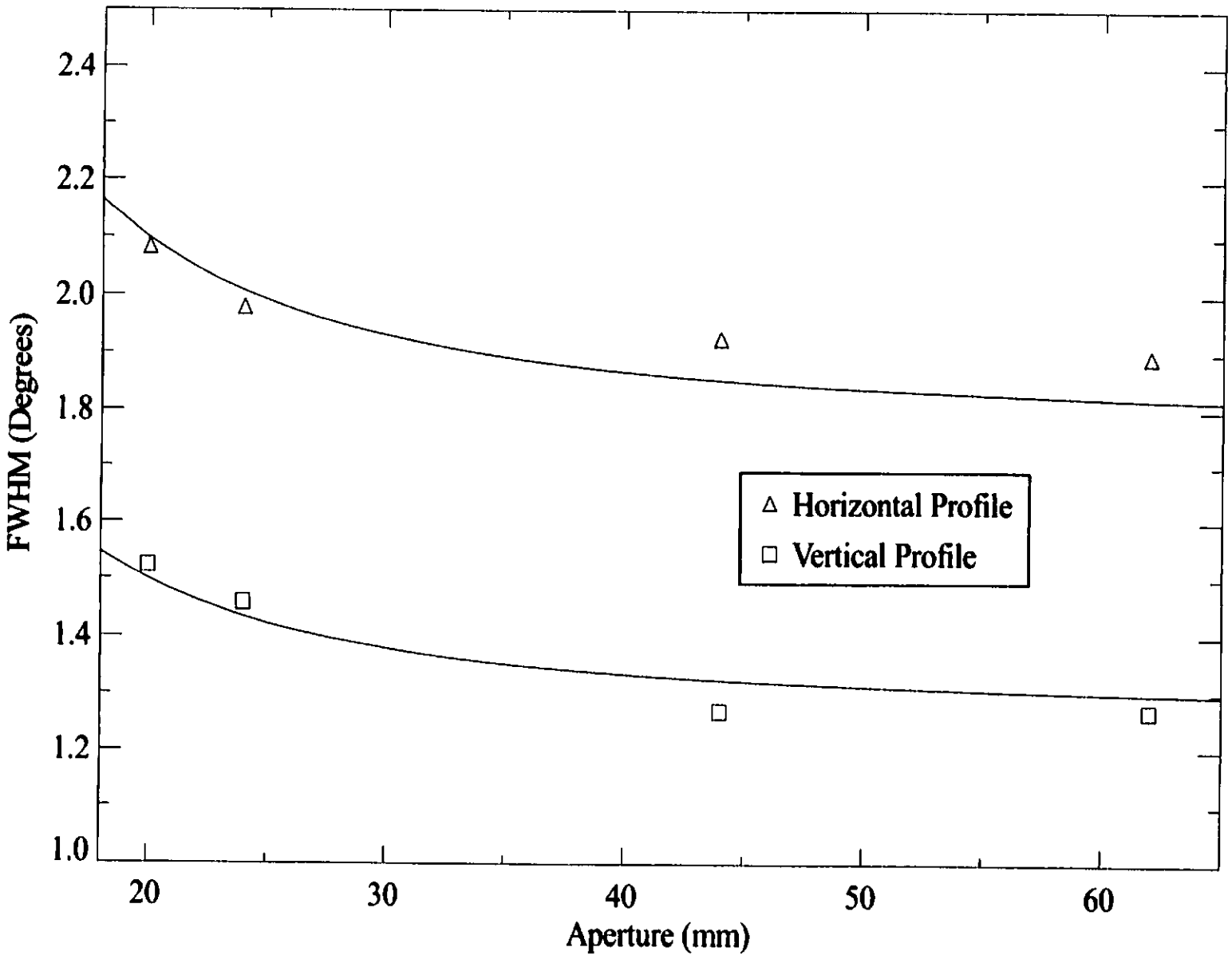

Figure 5.4 : FWHM of the fitted beam profiles as a function of aperture (symbols) compared to the theoretical curves (lines).

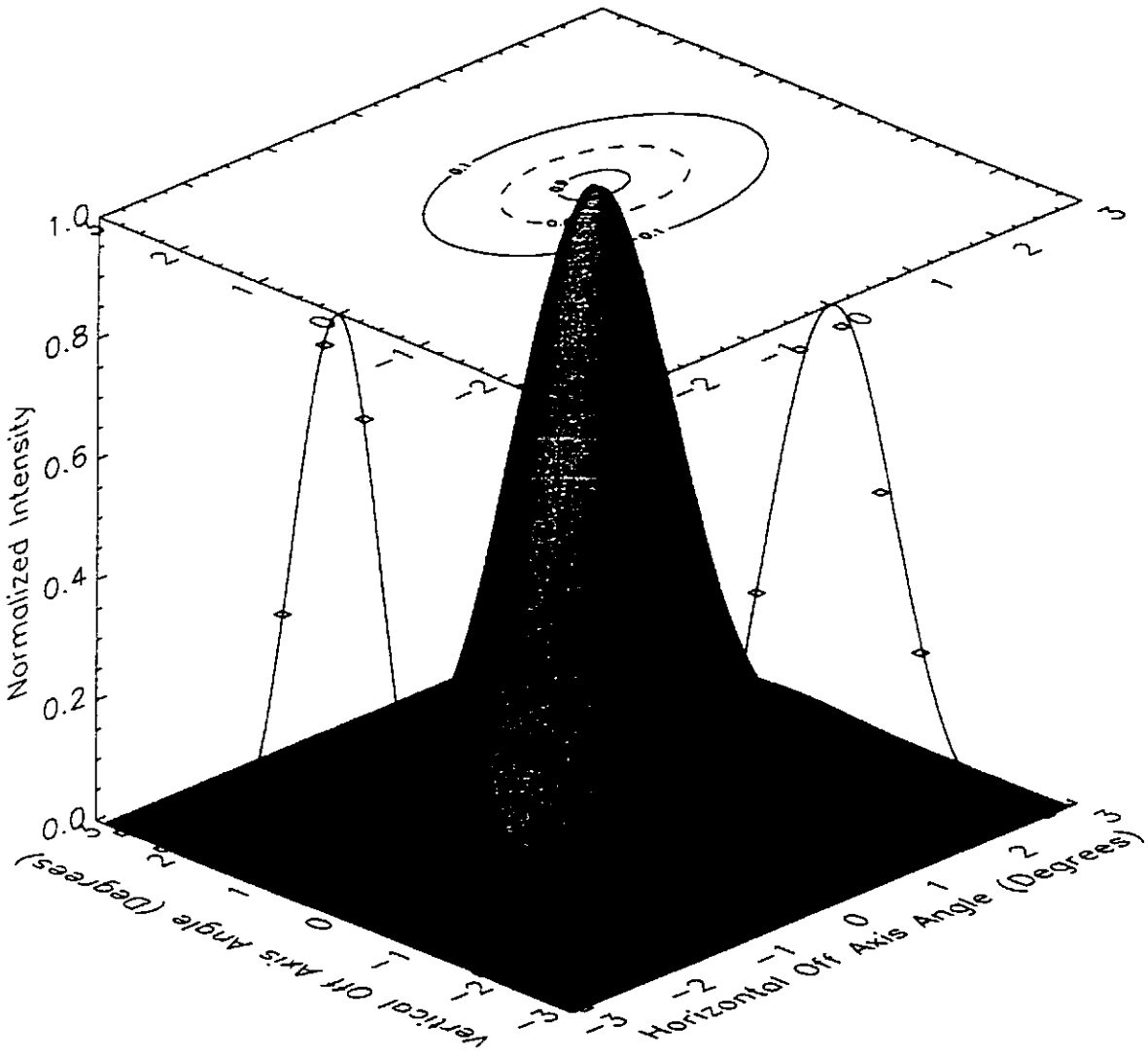

Figure 5.5 : 2-dimensional Gaussian beam profile reconstructed from the horizontal and vertical profiles for the 44 mm aperture. Squares represent averaged data for the horizontal and vertical scans.

The power in the beam is proportional to the integrated volume of the 2-dimensional Gaussian beam profile. We expect, therefore, that the volume described by the fitted 2-dimensional Gaussians should scale as the square of the aperture diameter. In Figure 5.6, the volumes of the fitted beam profiles are plotted against the square of the aperture. The line represents the linear (zero offset) least-squares fit to the lower three data points. The data are normalized so that the theoretical value for the 62 mm aperture is unity. There is a statistical uncertainty of approximately ±1% in the fitted volumes which is roughly equivalent to the size of the plot symbols on the graph.

It can be seen that there is good agreement between the theory and the data except for the 62 mm aperture, where the volume is ~ 87 % of the expected value. While the present data set does not contain sufficient detail to allow determination of the actual cause of this power loss, we expect that it is due to another source of vignetting in addition to the one in the internal optics. If, for example, the rooftop mirror became misaligned as it cooled, then the bolometers would view the field lens or the iris slightly off-centre. As a result, the narrow beams for the small aperture settings would pass through unobstructed, but the beam for the 62 mm aperture would be vignetted.

For simplicity, we model the power loss by considering the normalized effective area of a circular beam clipped by a circular aperture of the same diameter. This efficiency is given by Equation (5.4), where ϕ, is the aperture diameter, and x is the offset from the optical axis. For a 62 mm aperture, an efficiency of 87% corresponds to a misalignment of ~ 6 mm between the beam and the iris. If the misalignment is entirely in the rooftop, this corresponds to an error in the order of 1° in the dihedral angle, or in the tilt of the stage. In reality, the inefficiency is most likely due to the cumulative effects of smaller misalignments at several of the aforementioned points.

$$\eta_{Area} = \frac{2}{\pi}\left[Sin^{-1}\left(\sqrt{1-\frac{x^2}{\phi^2}}\right) - \frac{x}{\phi}\left(\sqrt{1-\frac{x^2}{\phi^2}}\right)\right]. \qquad (5.4)$$

Table 5.2 summarizes the total efficiency of the four aperture settings compared to an ideal circular aperture, taking into account the two sources of vignetting described above.

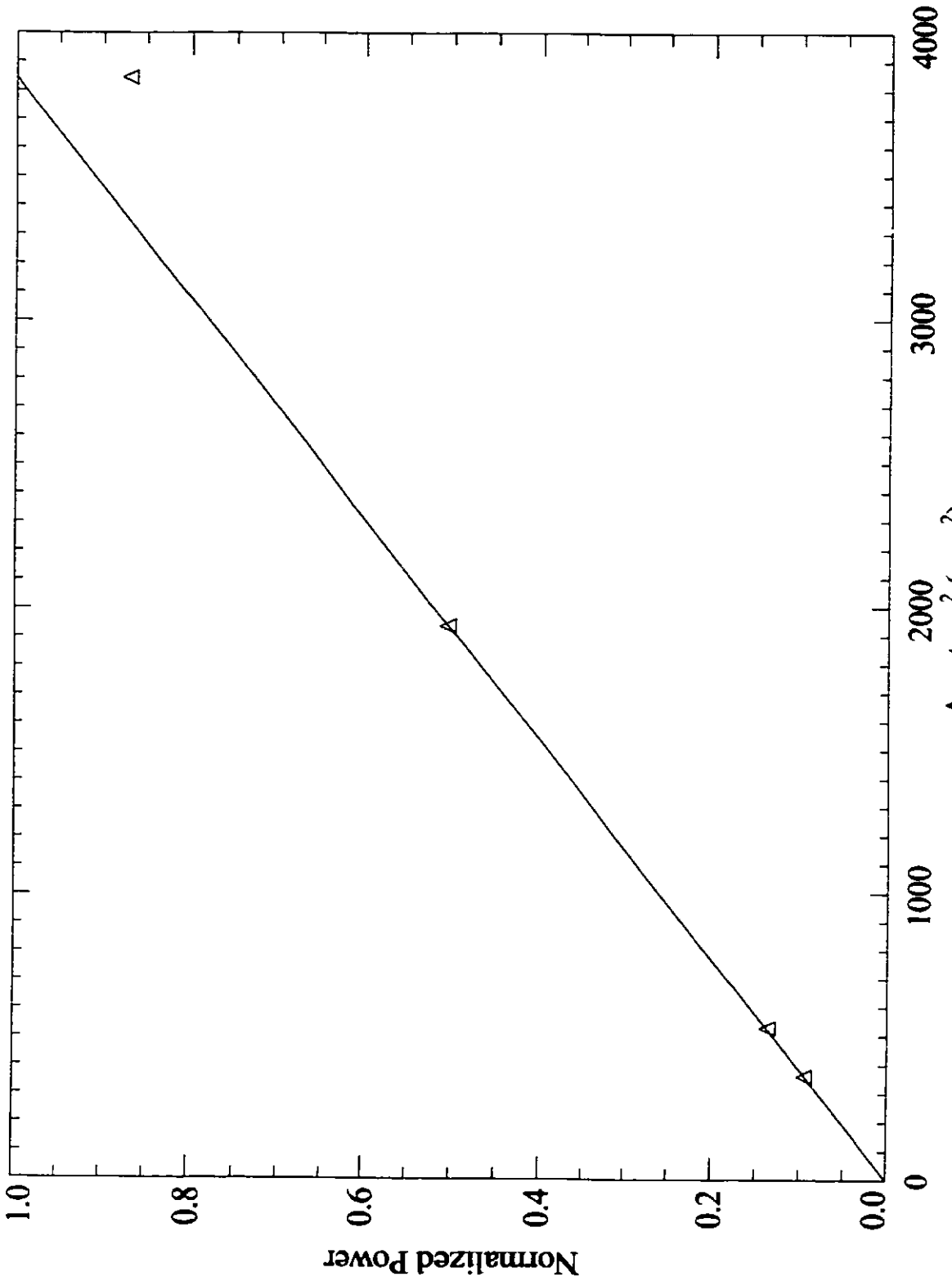

Figure 5.6 : Power from the fitted Gaussian profiles vs. the square of the aperture, normalized to the theoretical value for the 62 mm aperture. Symbols represent the data, the line represents the theoretical fit to the lower 3 data points.

Table 5.2 : Aperture Efficiencies

Aperture (mm)	FWHM (degrees) Horizontal	Vertical	Gaussian Eccentricity	Solid Angle Efficiency (η_Ω)	Area Efficiency (η_{Area})	Total Efficiency
20	2.08	1.52	0.682	0.73	1	0.73
24	1.98	1.46	0.676	0.74	1	0.74
44	1.93	1.27	0.752	0.66	1	0.66
62	1.90	1.27	0.742	0.67	0.87	0.58

The solid angle, Ω, and optical throughput, $A\Omega$, for an elliptical beam with semimajor and semiminor axes a and b, respectively, are given by Equations (5.5) and (5.6) where ϕ is the aperture diameter, and a and b are measured in degrees.

$$\Omega = \frac{4\pi^3 \cdot a \cdot b}{360^2} \quad . \tag{5.5}$$

$$A\Omega = \frac{\phi^2 \pi^4 \cdot a \cdot b}{360^2} \quad . \tag{5.6}$$

The throughputs for each aperture are given in Table 5.3. The throughputs for a f/35 beam are given for comparison in the far right column.

Table 5.3 : Optical Throughput

Aperture (mm)	Ω (str)	Throughput (m^2·str)	f/35 Throughput (m^2·str)
20	$7.56 \cdot 10^{-4}$	$2.38 \cdot 10^{-7}$	$2.01 \cdot 10^{-7}$
24	$6.92 \cdot 10^{-4}$	$3.13 \cdot 10^{-7}$	$2.90 \cdot 10^{-7}$
44	$5.86 \cdot 10^{-4}$	$8.92 \cdot 10^{-7}$	$9.75 \cdot 10^{-7}$
62	$5.77 \cdot 10^{-4}$	$1.74 \cdot 10^{-6}$	$1.94 \cdot 10^{-6}$

While the beam has been found to be elliptical when viewing a source in the far field, when the detector is coupled to the Fourier Transform Spectrometer (FTS), the telescope produces an image of the astronomical source at the field lens within the dewar, and the beam is found to be in good agreement with a f/35 beam. Consequently, the efficiency terms given in Table 5.2 are not used for a source in the near-field of the detector. For the NEP calculations later in this chapter, the throughput for a f/35 beam was assumed. The far-field beam profile tests did, however, provide a useful means of verifying that there were no serious optical alignment problems.

5.3 Frequency Response

The frequency response of the detector determines the optimum velocity of the interferometer scanning mirror. For a FTS, the frequency of modulation of the infrared radiation is given by $f=2v\sigma$, where v is the linear velocity of the moving mirror and σ is the wavenumber of the radiation. The frequency response also provides data to verify the predicted values of the heat capacity and thermal conductivity of the bolometer, which in turn are necessary for predicting the minimum NEP.

Following the notation of Chapter 2, the thermal time constant, τ, is defined by Equation (5.7), where G_d is the dynamic thermal conductance and C is the heat capacity of the bolometer. When observing a source, the time constant of the bolometer is modified by the electrothermal feedback from the temperature fluctuations of the bolometer. The effective time constant (or response time constant), τ_e, is given by Equation (5.8), where C is again the heat capacity, and G_e is the effective thermal conductance. Whereas the thermal time constant is the more fundamental quantity, in practice it is the effective time constant that is measured.

$$\tau \equiv \frac{C}{G_d} \ , \tag{5.7}$$

$$\tau_e \equiv \frac{C}{G_e} \ , \tag{5.8}$$

$$where \quad G_e = G_d - \alpha P\left(\frac{R_L - R_{Bol}}{R_L + R_{Bol}}\right) .$$

Two methods were used to determine the frequency response: The first method used the standard procedure of measuring the peak-to-peak detector output voltage as a function of optical signal frequency using an oscilloscope. For this measurement, a hot blackbody source (~ 1000 K) was placed in the detector beam, behind an ambient temperature chopper blade. Observations were made using the wide-band filter (5-35 cm^{-1}) with a 62 mm aperture and a chopping frequency range of 1 to 110 Hz. The detectors were operated with a bias current of ~ 40 nA. The second method made use of otherwise unwanted cosmic ray collisions. When observing at high altitudes, detectors typically record cosmic ray events at the rate of one every several minutes. A cosmic ray colliding with a bolometer element produces an effectively instantaneous thermal excitation of the crystal. When the detector is coupled to an FTS, the decay of the resulting voltage spike is digitized and recorded in the time-domain interferogram. While such spikes are normally removed from the interferogram before processing, the frequency spectrum of the spikes should characterise the frequency response of the detector.

5.3.1 Analysis

By plotting the detector output voltage as a function of frequency, the cutoff (or -3 dB) frequency can be obtained. The time constant is related to the cutoff frequency by $\tau = 1/(2\pi f_{3dB})$. It should be noted that while the typical cosmic ray decay curve shown in Figure 5.7 appears exponential on first inspection, it is incorrect to describe the time constant of the detector using the time constant of an exponential decay. The frequency spectrum of an exponential decay exhibits a $(1+f^2)^{-1}$ frequency dependence, whereas the true response of a bolometer is analogous to that of a single pole lowpass RC filter (see Chapter 2), and therefore has a $(1+f^2)^{-1/2}$ dependence. To extract the time constant from the cosmic ray decay curves, IDL code was written (see Appendix 6.3) to compute the FFT of 10 cosmic ray decay curves and then average the resulting frequency-domain data for each detector. A least squares fitting routine was used to fit the above equation to the data by varying the cutoff frequency. The frequency responses obtained from the chopped signal measurements and the cosmic ray spikes for each detector were then compared.

5.3.2 Results

Figure 5.8 shows the frequency response of the two detectors obtained from the cosmic ray analysis, compared with the normalized detector signal as a function of chopping frequency. The symbols represent the raw data, and the lines represent the best fit to the theory. The horizontal line represents the -3 dB amplitude. We notice immediately that the cutoff frequencies of the cosmic ray curves for both detectors are significantly lower than those of the chopped signal curves. This suggests that cosmic ray collisions excite the bolometer elements differently than does infrared radiation. Typical cosmic rays have energies in the MeV to GeV range, while infrared photons have energies of $\sim 10^{-3}$ eV. It is possible that cosmic rays produce such sudden heating of the element that the heat flow in the bolometer thermal links becomes nonlinear and the assumptions [3] made in the derivation of Equation (5.7) are no longer valid. Holland [4] has described the effect of power loading on bolometer responsivity, and has shown that the responsivity may become nonlinear when large changes in power loading occur. A change in the detector responsivity could also distort the shape of the observed decay curve. We can approximate the effect of a typical cosmic ray collision on the bolometers by considering the energies involved. A cosmic ray with energy E will heat the bolometer by a temperature of $\Delta T = E/C$ where C is the heat capacity of the bolometer. This will change the resistance of the bolometer by ΔR, which will generate a detector voltage ΔV as shown in Equation (5.9). Using typical values

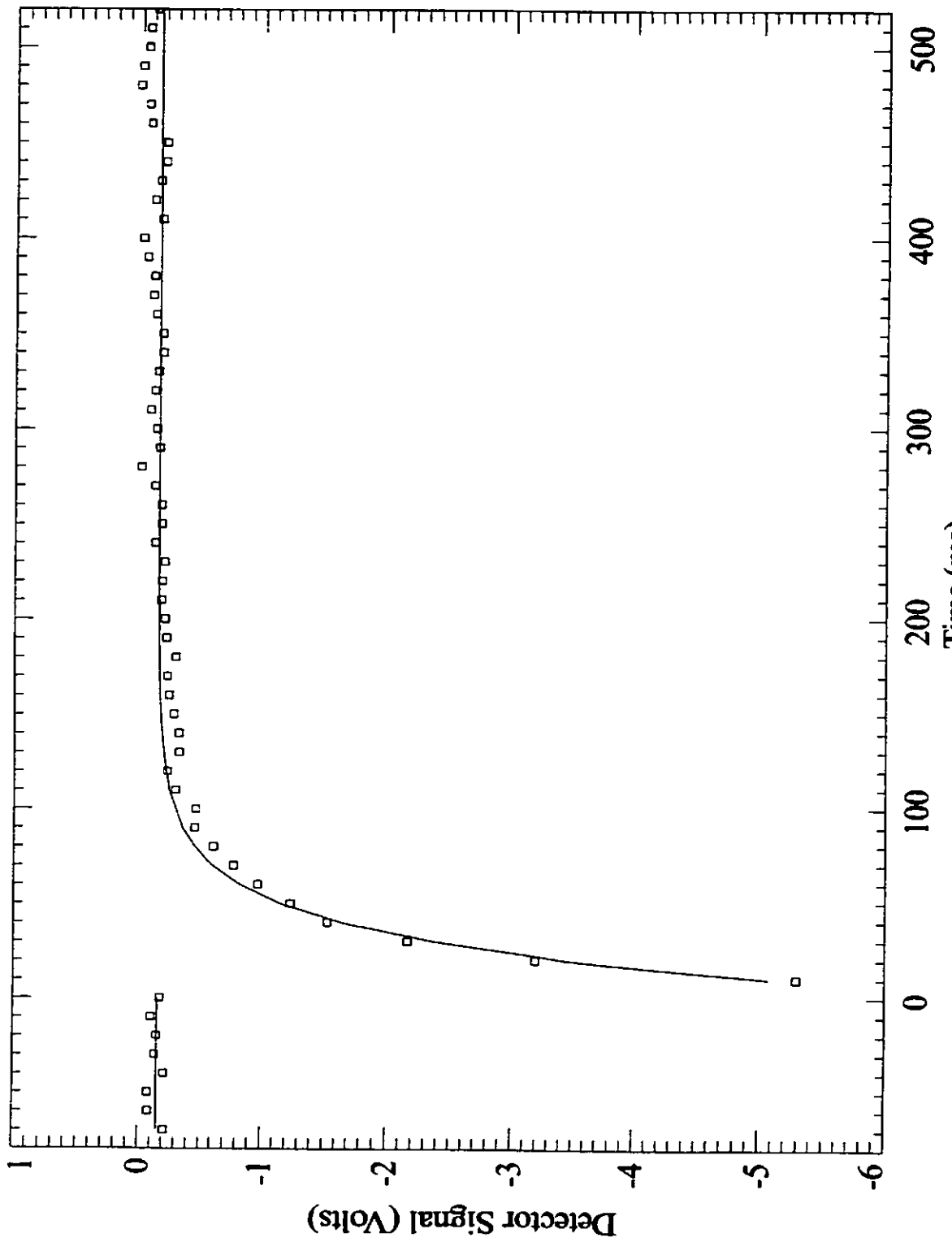

Figure 5.7 : Typical cosmic ray collision as recorded in an interferogram. An exponential decay curve is plotted for comparison (solid line).

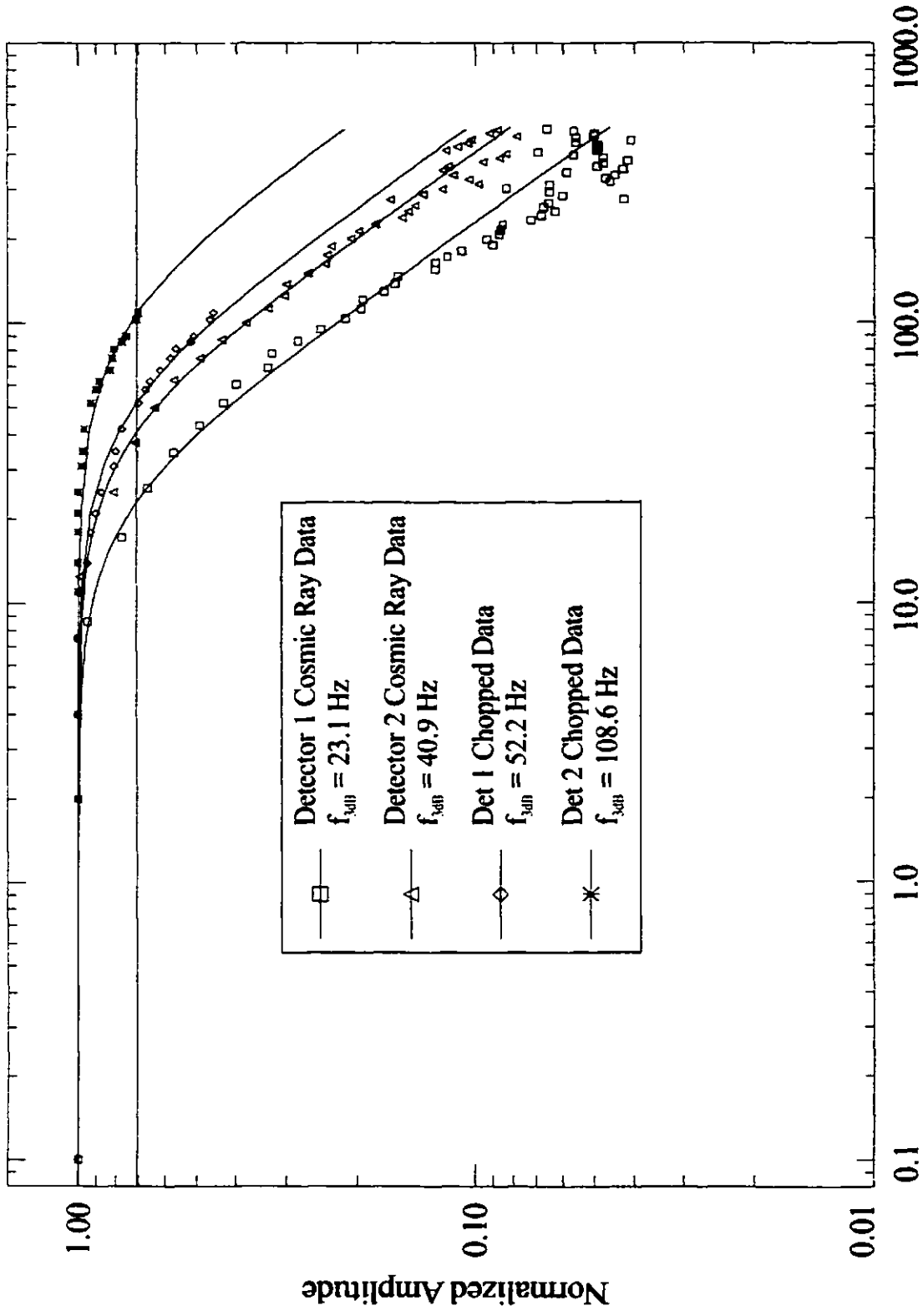

Figure 5.8 : Frequency response for both detectors. Curves in order of increasing cutoff frequency are: detector 1 cosmic ray data, detector 2 cosmic ray data, detector 1 chopped signal data, and detector 2 chopped signal data. The cosmic ray data points represent the average of 10 Fourier Transforms.

of I = 30 nA, T_0 = 0.3 K, C = 35 pJ/K, total FTS system gain of $Gain_{FTS} = 4 \cdot 10^5$, and the values defined earlier for the other bolometer parameters, we find that a spike of ~10 volts, which would saturate the interferogram scale, corresponds to a comic ray energy of only 420 eV. Or, taken another way, the heating of the bolometer element caused by a low energy, 1KeV shower particle would still be an order of magnitude greater than that from the typical modulated infrared signal produced by the FTS.

$$\begin{aligned} \Delta V &= Gain_{FTS} \cdot I \cdot \Delta R \\ &= Gain_{FTS} \cdot I \cdot R^* [e^{\left(T_s/T_0+\Delta T\right)^\alpha} - e^{\left(T_s/T_0\right)^\alpha}] , \\ &\quad where \quad \Delta T = \frac{E}{C} . \end{aligned} \tag{5.9}$$

Another possible explanation of the discrepancy in the frequency response results is that cosmic rays cause ionization as they collide with the crystal, which would effectively change the bias current and produce unpredictable results. The detector voltage produced by an induced change in the bias current would decay with a shorter time constant than the physical time constant of the bolometer, due to the filters in the bias generator circuitry (see Section 3.5).

It is also evident from Figure 5.8 that detector 2 has a higher cutoff frequency than detector 1 in both data sets. This shorter time constant could correspond to a higher thermal conductance, lower heat capacity, or both since it is difficult to control the exact amount of the materials used in the fabrication of each detector (see Chapter 2 for a description of the bolometer construction). Final determination of these parameters can only be accomplished by modelling the V-I performance of the detectors, which is done in the following section. The measured cutoff frequency from the cosmic ray analysis is 23.1 Hz for detector 1 and 40.9 Hz for detector 2. It is assumed that the frequency responses for the chopped radiant source represent the true behaviour of the detector. In this case, the measured cutoff frequencies are 52.2 Hz for detector 1 and 108.6 Hz for detector 2. These values are well suited to the modulation frequencies of 20 to 60 Hz produced by the FTS with a scanning mirror velocity of 1 cm·s^{-1}, and spectral bands of 10 to 30 cm^{-1}.

It is important to recognize that the choice of operating bias current has a strong effect on the time constant of the bolometers. With the use of the V-I equations derived in the next section, it is possible to plot the ratio of τ_e to τ (see Equation (2.16)) as a function of bias current, as shown in Figure 5.9. As will be shown, the choice of operating bias current not only affects the detector frequency response, but the NEP as well.

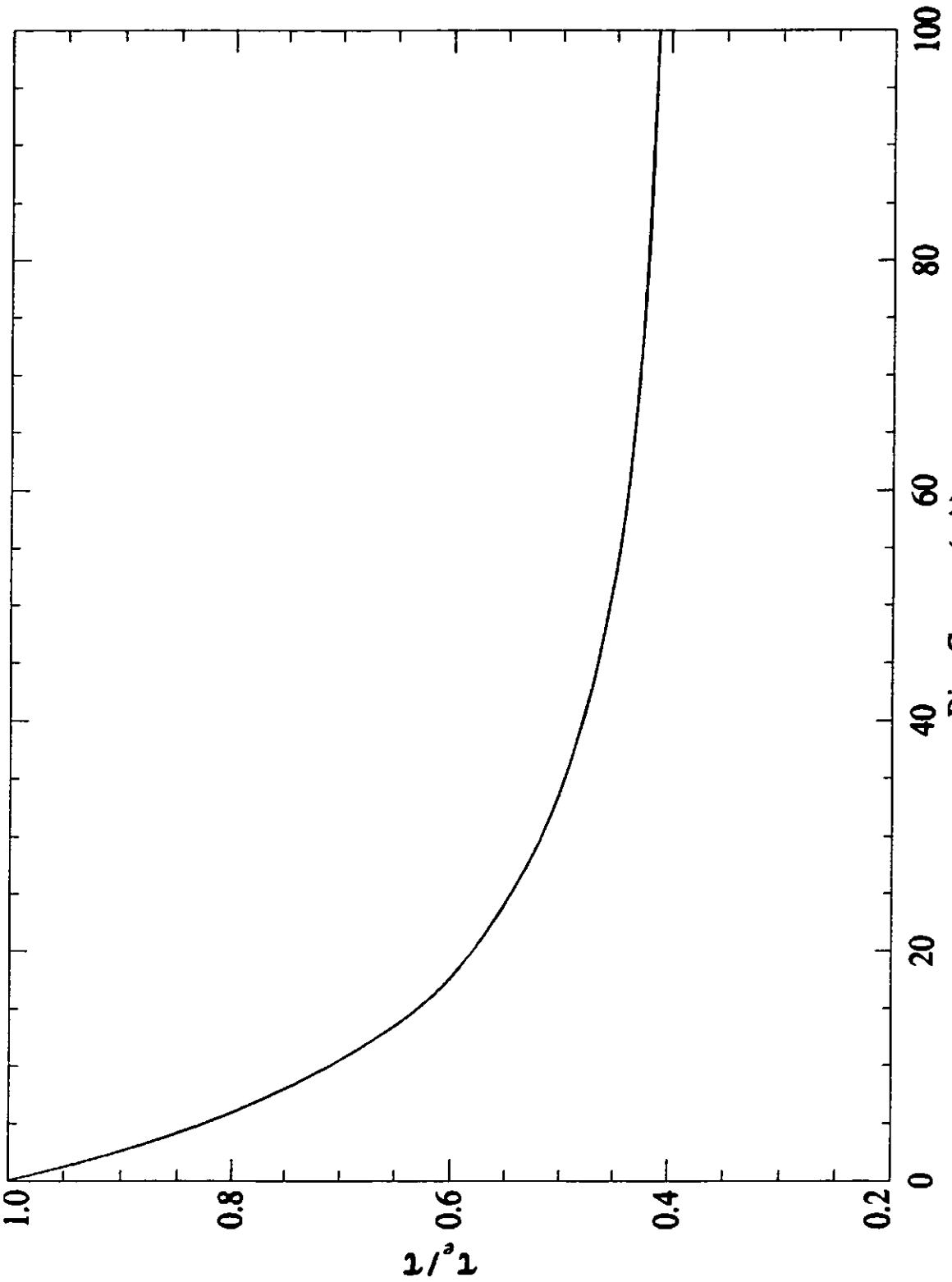

Figure 5.9 : Ratio of the effective time constant, τ_e, to the physical time constant, τ, calculated using Equation (2.16) as a function of bias current (typical of both detectors).

5.4 V-I Characteristics

Measurement of the bolometer voltage as a function of bias current and radiant power loading provides a simple method to characterize the detector's performance. Analysis of the V-I curves, and a knowledge of the bolometer frequency response, allows the NEP to be calculated as a function of bias, which determines the optimum bias current for a given loading condition. Also, by fitting theoretical curves to the V-I data, one can obtain values for parameters that would otherwise be difficult to measure such as the thermal conductance and detector efficiency.

A C program was written to perform the data collection using a simple data acquisition module [5] connected to a PC. The software continuously records the bolometer voltage, V_{Bol}, as the bias current is varied by manually adjusting the bias voltage, V_{Bias}, from 0 to roughly 2 volts. Data was collected for both detectors and all filter bands viewing a hot black body (338 K), an ambient black body (290 K), a liquid nitrogen bath (73 K), and a blanked off filter position corresponding to the least possible loading (~ 4 K). Code for the data collection software is given in Appendix 6.4.

5.4.1 Analysis

A diagram of the bolometer circuit was previously shown in Figure 2.2. The variables in the following equations refer to the ones given in that diagram. For theoretical modelling we need to convert the recorded bias voltage to bias current flowing through the bolometer element. From Ohm's Law we find the current flowing through the element as given in Equation (5.10). We can also calculate the bolometer resistance from Equation (5.11) where V_{Bol} is the bolometer voltage, and R_L is the load resistance. Since the bolometers are actually configured in a differential circuit as shown in Figure 3.8, the total bipolar bias voltage, V_{Bias}, across the load resistor network is twice the measured unipolar bias voltage, V_c.

$$I = \frac{V_{Bias}}{R_L + R_{Bol}} \,. \tag{5.10}$$

$$R_{Bol} = \frac{V_{Bol} \cdot R_L}{V_{Bias} - V_{Bol}} \,. \tag{5.11}$$

The measured detector output voltage, V, is related to the actual bolometer voltage, V_{Bol}, by Equation (5.12), where the gain of the JFETs and amplifiers is taken into account. The amplifiers introduce a

slight DC offset which must also be removed. This offset is measured when V_{Bias} is zero.

$$V_{Bol} = \frac{V}{Gain} - offset \quad . \tag{5.12}$$

Using the Equations (5.11) and (5.12), Equation (5.10) becomes:

$$I = \frac{2V_C - \left(\frac{V}{Gain} - offset\right)}{R_L} \quad . \tag{5.13}$$

The bolometer voltage can now be plotted as a function of bias current flowing through the element. Figure 5.10 shows the measured V-I curves for detector 1 and all filters. In each plot, the uppermost curve represents the detector viewing the blanked off filter position, which is the curve with the lowest possible loading. The second curve from the top is for the liquid nitrogen source, the next is for the ambient source, and the bottom curve is for the hot black body. There are no blanked off or hot black body curves for the 1400 and open bands since these filters were measured in May of 1997 and V-I curves were only measured for LN_2 and ambient sources that year. Figure 5.11 shows the corresponding plots for detector 2. Later in this chapter, the unipolar bias voltage, V_c, is used for abscissae in the plots instead of the bias current (which is the more fundamental quantity), since V_c is the quantity that is directly adjusted when selecting the operating bias current.

There is no way to directly measure the thermal conductance of the bolometers. Also, wiring limitations prevent us from mounting temperature sensors on the bolometer housings, so there is no way to measure precisely the heat sink temperature, T_0, of the bolometer housings when the detector is in operation. There are, however, two methods of determining these parameters by analysing the V-I curves. The first method is to assume the functional form of the thermal conductance, and fit the resulting V-I equations given by Equations (2.21) to the experimental data by varying G_0, T_0, and the thermal power loading. The second method is to determine the actual temperature dependence of G_d, and the zero-load temperature of the bolometers, and use these quantities in the theoretical equations to determine the difference in power loading between the various V-I curves.

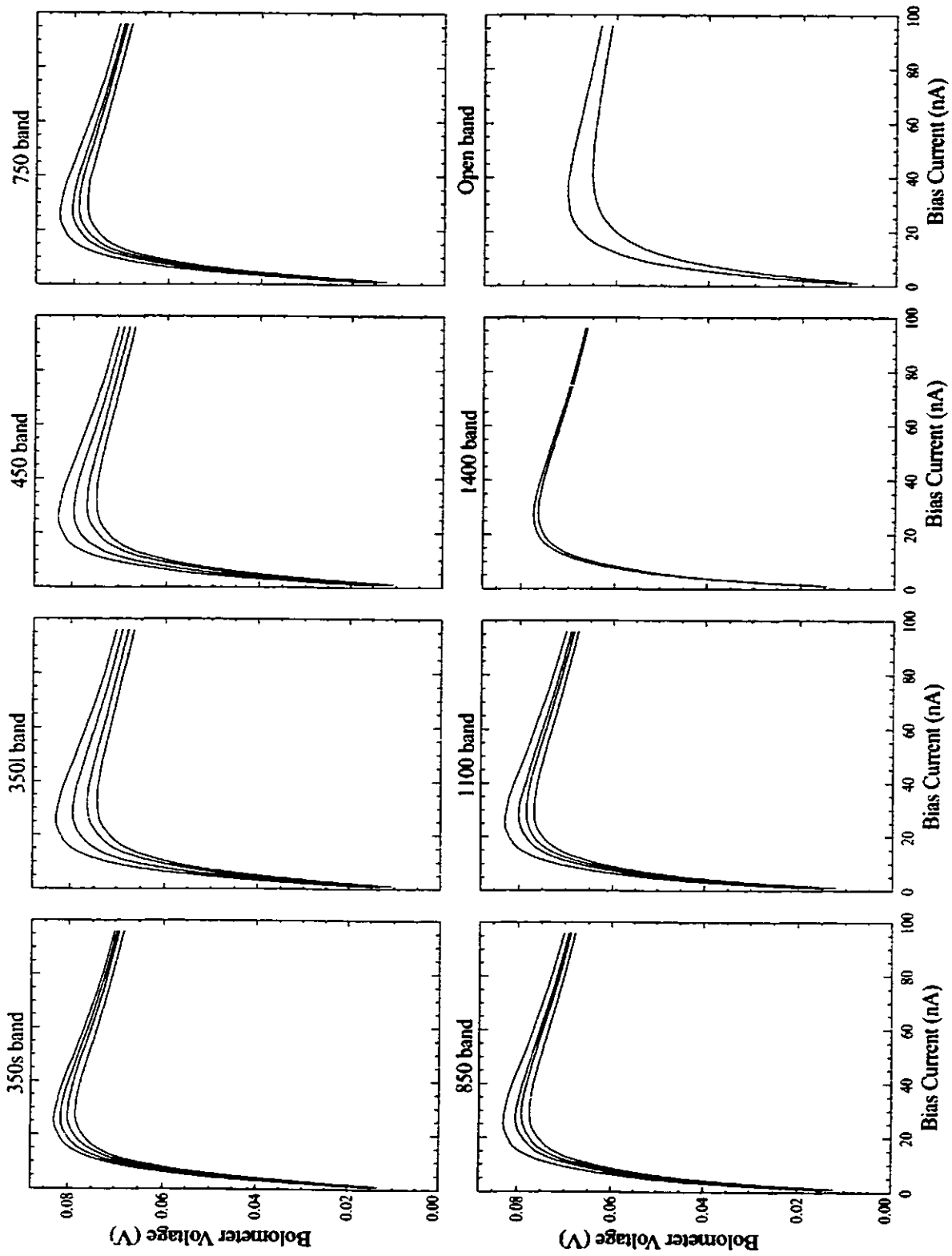

Figure 5.10 : V-I curves for detector 1 and all filters. In each plot, the curves in order from top to bottom are for the blanked off, liquid nitrogen, ambient, and hot black body sources. The 1400 and open bands only have curves for liquid nitrogen and ambient sources.

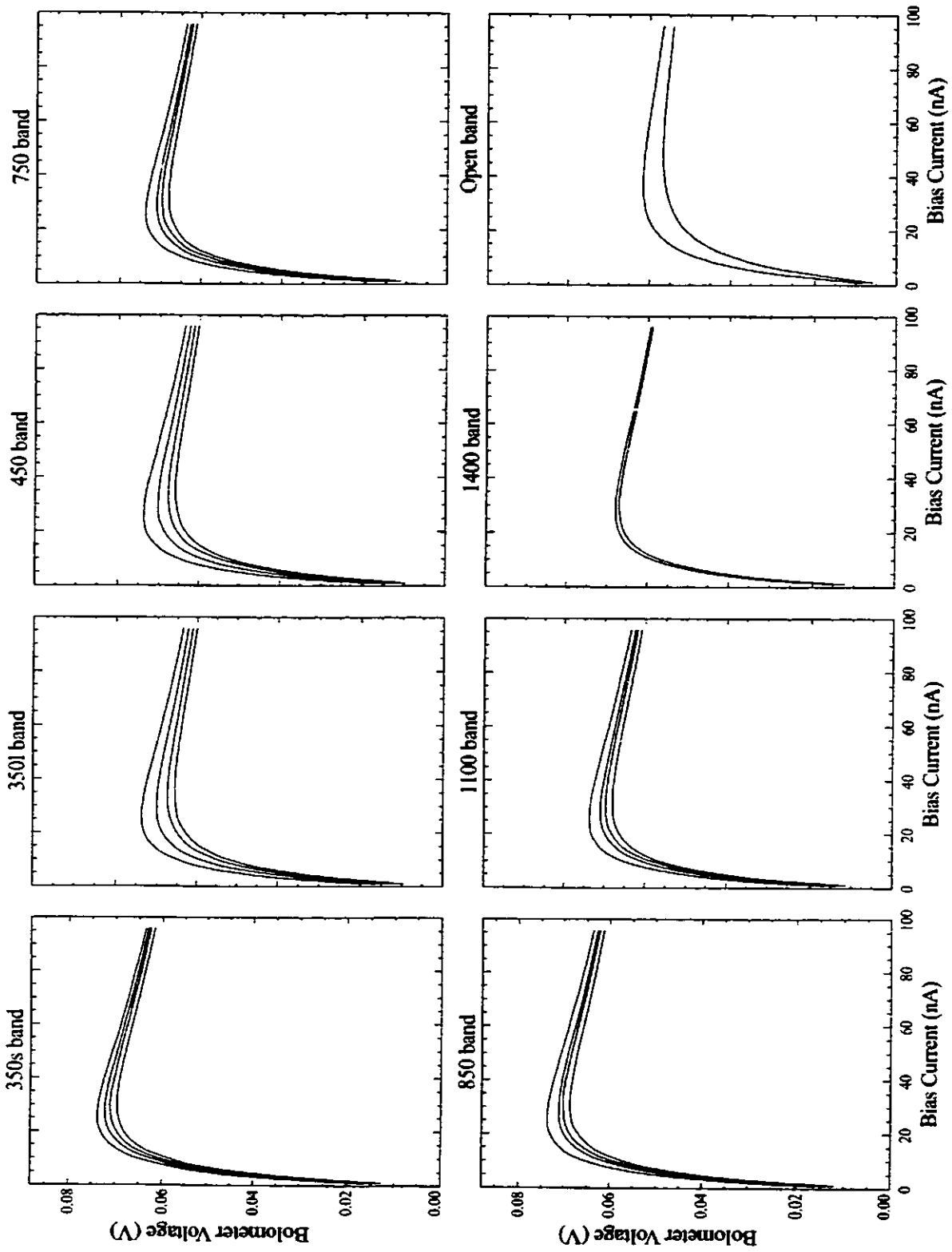

Figure 5.11 : V-I curves for detector 2 and all filters. In each plot, the curves in order from top to bottom are for the blanked off, liquid nitrogen, ambient, and hot black body sources. The 1400 and open bands only have curves for liquid nitrogen and ambient sources.

The nearest to ideal (zero radiant loading) behaviour is achieved by blocking off all radiation as close as possible to the bolometer feed horns. Since all six filters were required for astronomical observations during the observing runs in 1997 and 1998, and since replacing a filter involves warming up and disassembling the dewar (a process that takes at least 24 hours), the detector field of view was blocked by carefully positioning the filter assembly between the detents that define the 350s and 350l filter positions. In this way, the bolometer loading was limited to the background radiation in the bolometer cavity and radiation from the ~ 4 K copper filter wheel. The position between the 350s and 350l filters was chosen since these filters have low transmission, minimizing the amount of any leaked radiation. Least squares fitting of the data to the theoretical V-I equations given in Section 2.3 was performed using IDL code (Appendix 6.5.5). The bath temperature T_0, thermal conductance G_0, and background radiant power loading Q, were free parameters, and the software generated theoretical curves at intervals spanning the three-dimensional variable space for both detectors. After the best fit was found, the radiant loading was determined for the liquid nitrogen and ambient sources by least squares fitting holding the other parameters fixed.

5.4.2 Results

Figures 5.12 and 5.13 show the theoretical V-I curves for detectors 1 and 2, respectively. It can be seen that the theory provides a better fit to the data for detector 1 than for detector 2. This is possibly due to the excess power loading experienced by detector 2, or to a deviation from the theoretical thermal coefficient of resistance for that detector. A summary of the parameters whose values were determined by the fitting procedure is given below in Table 5.4. The uncertainties are defined as the step size in the array of parameter values used in the fitting routine, and indicate the relative sensitivity of the theoretical fit to variation in the corresponding parameters.

Table 5.4 : Parameters Determined by Theoretical V-I Fits

	Detector 1		Detector 2	
Parameter	Value	Uncertainty (+/-)	Value	Uncertainty (+/-)
G_0 (nW/K)	24.55	0.1	20.43	0.04
T_0 (K)	0.3000	0.0003	0.2991	0.0001
Loading Q (pW)	89.2	1.5	157.1	0.5

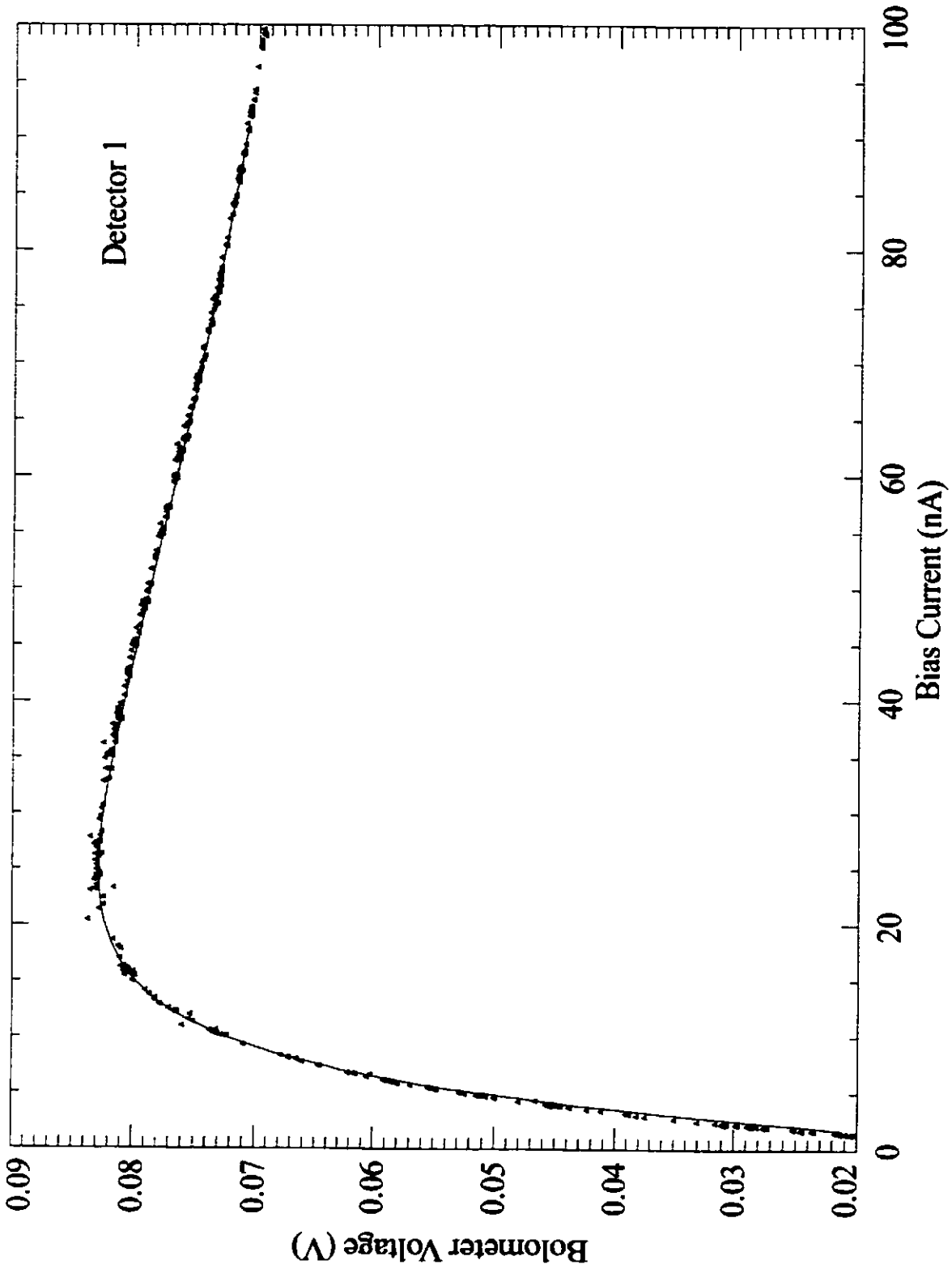

Figure 5.12 : Theoretical V-I curve (lines) fitted to raw data (symbols) for detector 1 and the blanked off position.

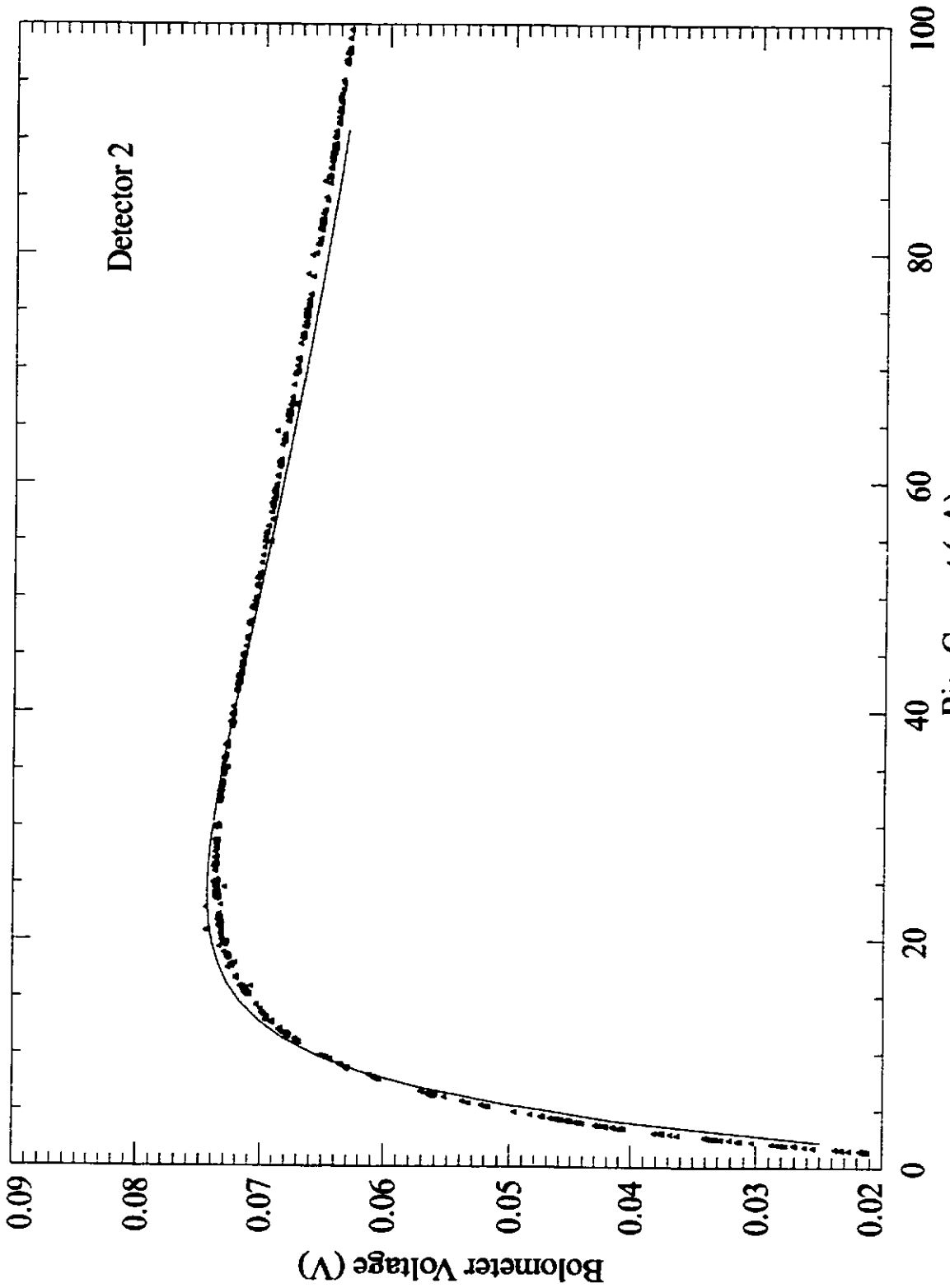

Figure 5.13 : Theoretical V-I curve (lines) fitted to raw data (symbols) for detector 2 and the blanked off position.

Theoretical values for the radiant power falling on the bolometers for the various filters are given in Table 5.5. It can be seen that, in general, detector 2 is more loaded than detector 1. The loading for the 1400 and Open bands was obtained by fitting to the 1997 V-I data, as is therefore less reliable since there were no blanked off measurements in that year. The values in this table will be used in Section 5.5 for calculation of the optical responsivity. It should be noted that comparing the power loading calculated using the Planck function with the data in the table is not a reliable way of obtaining the filter efficiencies since it is difficult to calculate the theoretical background loading on the bolometers. An alternative method of determining the filter efficiencies is presented in Section 5.5.

Table 5.5 : Radiant Power Loading Determined by V-I Fits

Filter Band	Power from 73 K Source (pW)		Power from 290 K Source (pW)	
	Detector 1	Detector 2	Detector 1	Detector 2
350s	152	225	225	284
350l	256	337	438	495
450	253	331	405	490
750	212	282	283	378
850	212	278	273	341
1100	230	295	319	376
1400	272	389	341	458
Open	655	849	963	1170

Even though the theoretical modelling of the V-I curve for detector 1 is particularly good (see [4] for comparison), the fit is still less than perfect; the theoretical curve for detector 1 has the same curvature problem as the curve for detector 2 (it crosses the experimental curve three times), although to a much lesser extent. There are two principal reasons why the theoretical model differs from the experimental data: either the sink temperature changes as a function of bias current, or the functional form of G_d is not adequate (we assume that the resistivity of the bolometer elements is known exactly, and there is no electric field effect in the bolometer crystal, which was considered by Holland [4]). It is further assumed that since the thermal conductance of the stage and heat capacity of the ^{3}He bath are both large relative to the thermal power loading from the bolometers, the temperatures of the bolometer housings do not change significantly. In any case, modelling the thermal fluctuations in the stage would be extremely difficult.

The bolometer resistance as a function of temperature was determined in Chapter 2, so we can use Equation (2.9) with the measured V-I data to produce a plot of the bolometer temperature as a function of bias current. Figure 5.14 shows the corresponding plot for detector 1 viewing the blanked off filter position. When the bias current is zero, the bolometer experiences the minimum possible power loading, and the temperature of the bolometer at this point sets an upper limit on the bath temperature. By calculating the temperature axis intercept for Figure 5.14 and the similar plot for detector 2, we find minimum temperatures of 0.293 K and 0.290 K for detectors 1 and 2 respectively. We assume that the sink temperature, T_0, does not differ significantly from these values, which are consistent with the temperature of ~0.3 K measured by the GR100 Ge stage temperature sensor.

By using Equation (2.5), and the interpolation routines given in Appendix 6.5, we can calculate G_d as the derivative of the $P=I^2R$ vs. T curve. Plots of this derivative for both detectors viewing the blanked off filter position are shown in Figure 5.15. The solid lines represent the best fits of the thermal conductance, calculated in Equation (5.14) by taking the derivative of Equation (2.3) with respect to T using the assumed form of G in Equation (2.6). It can be seen that the resulting form of G_d fits the experimental derivative curve well except at low temperatures (ie: at low bias currents), where the actual thermal conductance drops off more rapidly. Although the experimental curve is noisy, the general shape of the curve is the same for all filters, indicating that the change in slope at low bias current is not due to mathematical propagation of the random jitter inherent in the V-I data. Since a thermal conductivity of zero at $T=T_0$ is clearly nonphysical, we assume that the drop in thermal conductance is due to some increase in resistance to phonon flow for small thermal gradients, ΔT. There is, however, no compiled data for the thermal conductance of our link components with such small thermal gradients ($\Delta T < 40$ mK). Without a true functional form for the thermal conductance of our links, we can not go any further to improve the theoretical fit; we can only point out the deficiencies of the current model. We can, however, fit Equation (5.14) to the experimental G_d data to obtain values for G_0 more directly. Using this method, we obtain values of 23.5 and 19.4 nW/K for detector 1 and 2 respectively.

$$G_d = \frac{d}{dT}\left(G_0\left(\frac{T}{T_0}\right)^{\beta}(T-T_0)\right)$$
$$= G_0\left(\frac{2T}{T_0}-1\right) \quad , \quad \text{using } \beta = 1 \text{ for a metal link.} \tag{5.14}$$

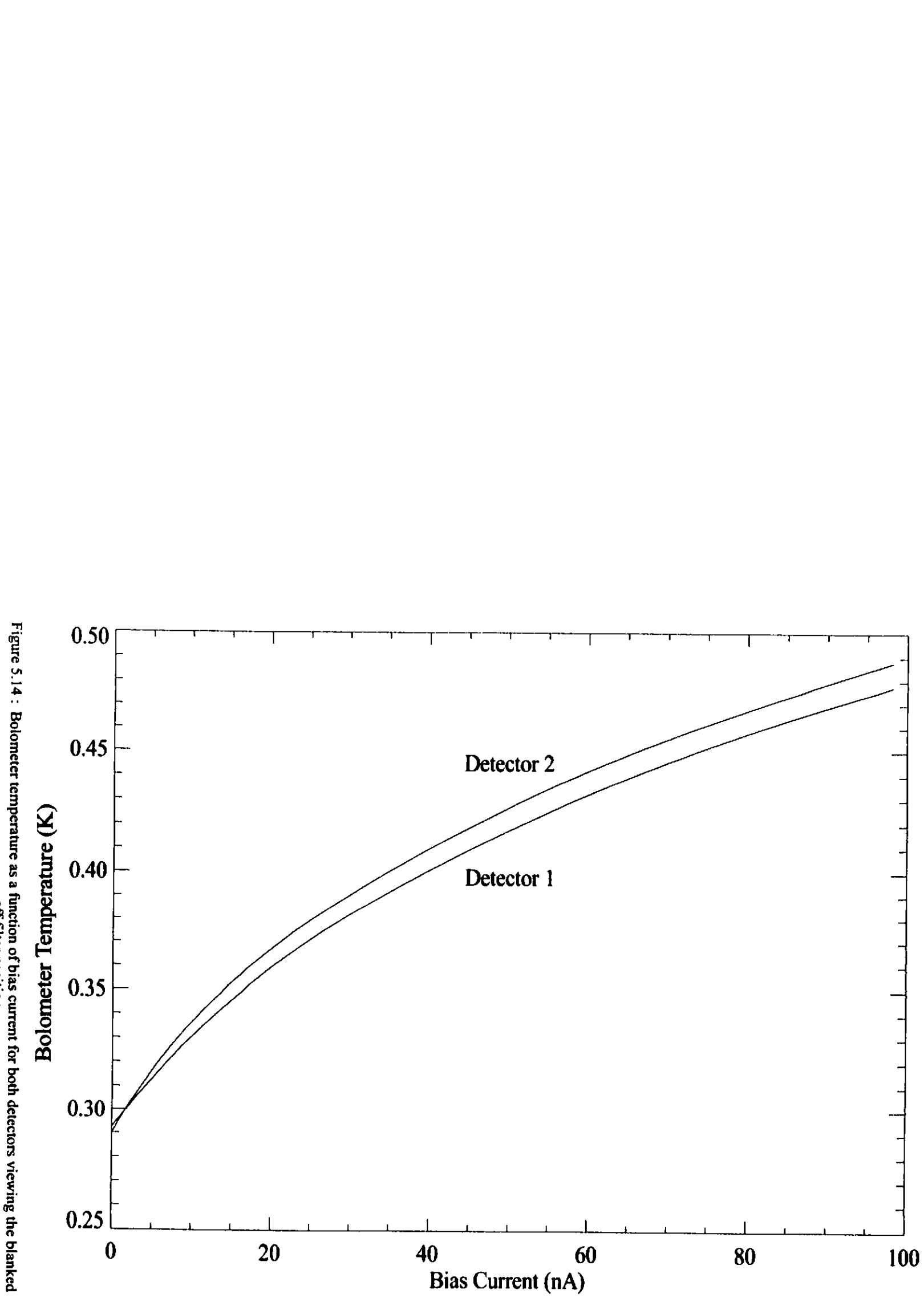

Figure 5.14 : Bolometer temperature as a function of bias current for both detectors viewing the blanked off filter position.

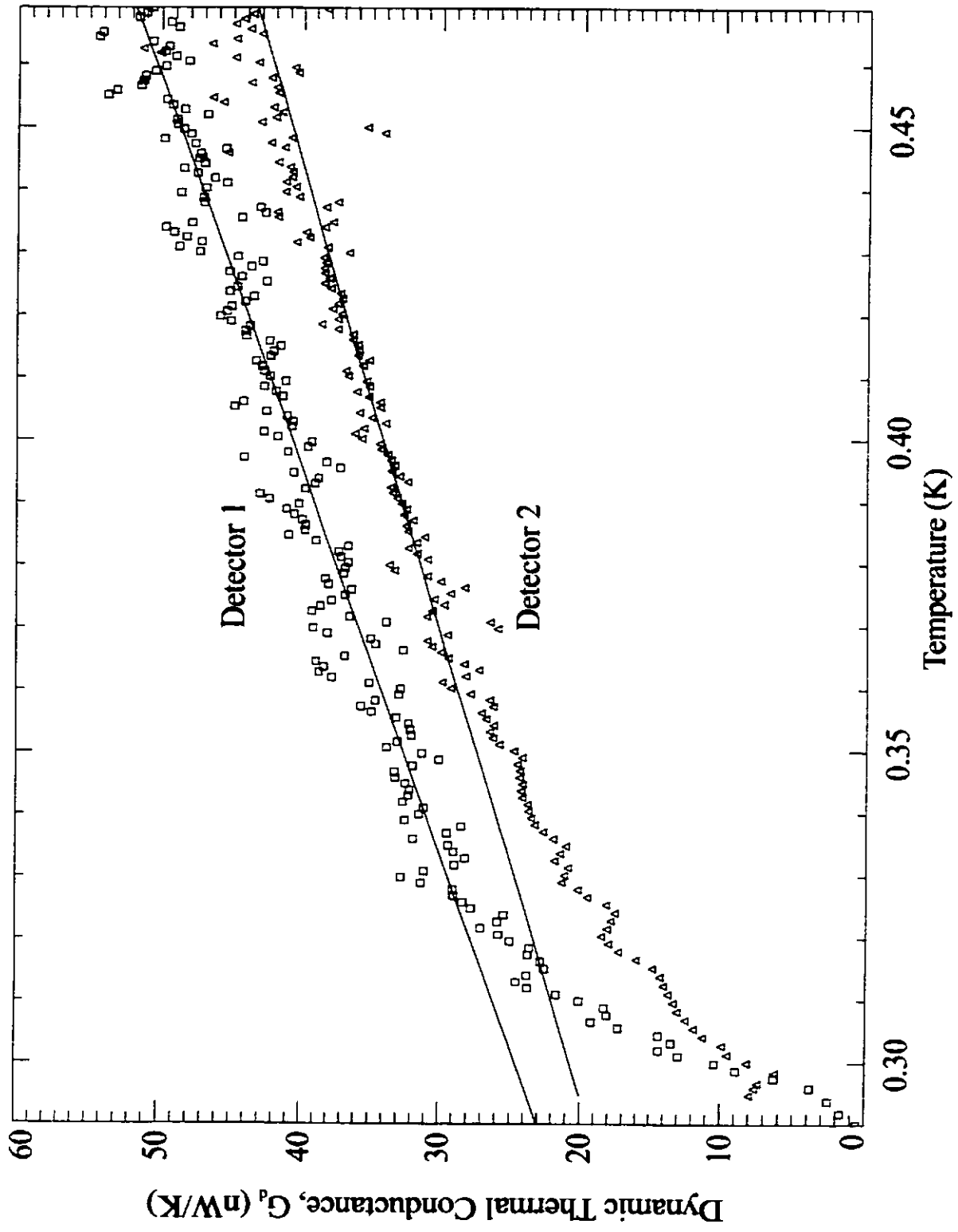

Figure 5.15 : Thermal conductance, G_d, as a function of bolometer temperature. Symbols represent the experimental data, lines represent best theoretical fits. The upper curves are for detector 1, the lower curves are for detector 2.

We are now able to verify the bolometer heat capacities as given in Table 2.1. Since we now know the thermal conductances of the two detectors, we can solve Equation (5.7) for the heat capacity, C, using the time constants from the previous section. We must first convert the measured effective time constant to the physical time constant, τ. The frequency response tests were performed with the detector bias voltage set at 0.75 V. Using Equation (5.13), this bias voltage corresponds to bias currents of 35.5 and 35.7 nA for detectors 1 and 2, respectively. The ratio of the measured time constant to the physical time constant is given by Equation (2.16), and at the given bias currents, the ratios are 0.501 and 0.503, respectively. This leads to physical time constants of 6.08 and 2.92 ms. Finally, the thermal conductance at $T=T_0$ for each bolometer is simply G_0, so the heat capacities at $T=T_0$ are calculated from Equation (5.7) as 143 and 56.9 pJ/K for detectors 1 and 2, respectively. Although 143 pJ/K for detector 1 is significantly larger than the estimated value of 35 pJ/K, the range set by manufacturing tolerances, particularly of the epoxy droplets, is large enough to account for the discrepancy.

5.5 Responsivity

The responsivity of the detector, defined as the detector output voltage produced by a given radiant power input, is useful for determining the optimum operating bias current, NEP, optical efficiency, and thermal conductance of the system. It also provides a method to verify some of the parameter values obtained from the V-I analysis in the previous section. In this section, the responsivity will be determined as a function of bias current using purely electrical measurements from the V-I curves, as well as from electrical/optical measurements. A comparison of the two methods will then be used to determine the optical efficiency of the detector.

5.5.1 Analysis

The responsivity of a detector is defined as $S = \frac{dV}{dQ}$ where V is the bolometer voltage and Q is the radiant power loading on the element. This derivative can be evaluated directly using the Equations (2.21) to give the zero frequency electrical responsivity in Equation (5.15), assuming the parameter β is unity.

$$S_0 = -\frac{1}{2}\sqrt{\frac{T_0 R^*}{G_0 T(T-T_0)-QT_0}}\cdot e^{\sqrt{T_s/4T}} \quad . \tag{5.15}$$

For a detector with a single time constant, the zero frequency responsivity, S_0, is attenuated with increasing frequency [6] according to Equation (5.16).

$$S_{(\omega)} = S_0 \cdot \left(1+\omega^2\tau_e^2\right)^{-1/2} = -\frac{1}{2}\sqrt{\frac{T_0 R^*}{G_0 T(T-T_0)-QT_0}} \cdot e^{\sqrt{T_g/4T}} \cdot \left(1+\omega^2\tau_e^2\right)^{-1/2} \quad . \tag{5.16}$$

Alternatively, Jones [7] gives the following equation for the frequency dependent electrical responsivity:

$$S_{(\omega)} = \frac{R_L}{2IR_{Bol}} \cdot \frac{Z_{Bol(\omega)} - R_{Bol}}{Z_{Bol(\omega)} + R_L} \quad . \tag{5.17}$$

If we take into account the shunting effect of the bias network [6], Equation (5.17) can be rewritten as Equation (5.18), where R_{Amp} is the amplifier input impedance and the other terms have the usual meaning.

$$S_{(\omega)} = \frac{R_L R_{Amp}}{R_L R_{Amp} + Z_{Bol(\omega)} R_{Amp} + R_L Z_{Bol(\omega)}} \cdot \frac{Z_{Bol(\omega)} - R_{Bol}}{2V_{Bol}} \quad . \tag{5.18}$$

For our JFET input amplifiers (IFN146, see Chapter 3), with input impedances of $\sim 10^{12}\,\Omega$, Equation (5.18) reduces to Equation (5.17) in the limit of high R_{amp}. If the bolometer parameters used in Equation (5.16) are correct, then these two methods should give the same responsivity as a function of bias.

The optical responsivity, $S = \frac{\Delta V}{\Delta Q}$, can be determined directly from the voltage difference between two V-I curves if the difference in radiant power loading on the bolometer, ΔQ, is known (implying that the filter efficiencies are also known). Since the measured optical and electrical responsivities should be equal, we can compare the electrical responsivity with the optical responsivity, calculated using the theoretical ΔQ from the Planck function, to determine the optical efficiencies for the various filters.

5.5.2 Results

Figure 5.16 shows the electrical responsivity for detector 1 using the 350s band, calculated using Equations (5.15) and (5.17). The fact that the theoretical curve (represented by the solid line in the figure) deviates from the experimental curve (represented by symbols) emphasises that the theoretical model used to determine the bolometer parameters in the V-I fitting routines is inadequate. However, above 20 nA, the

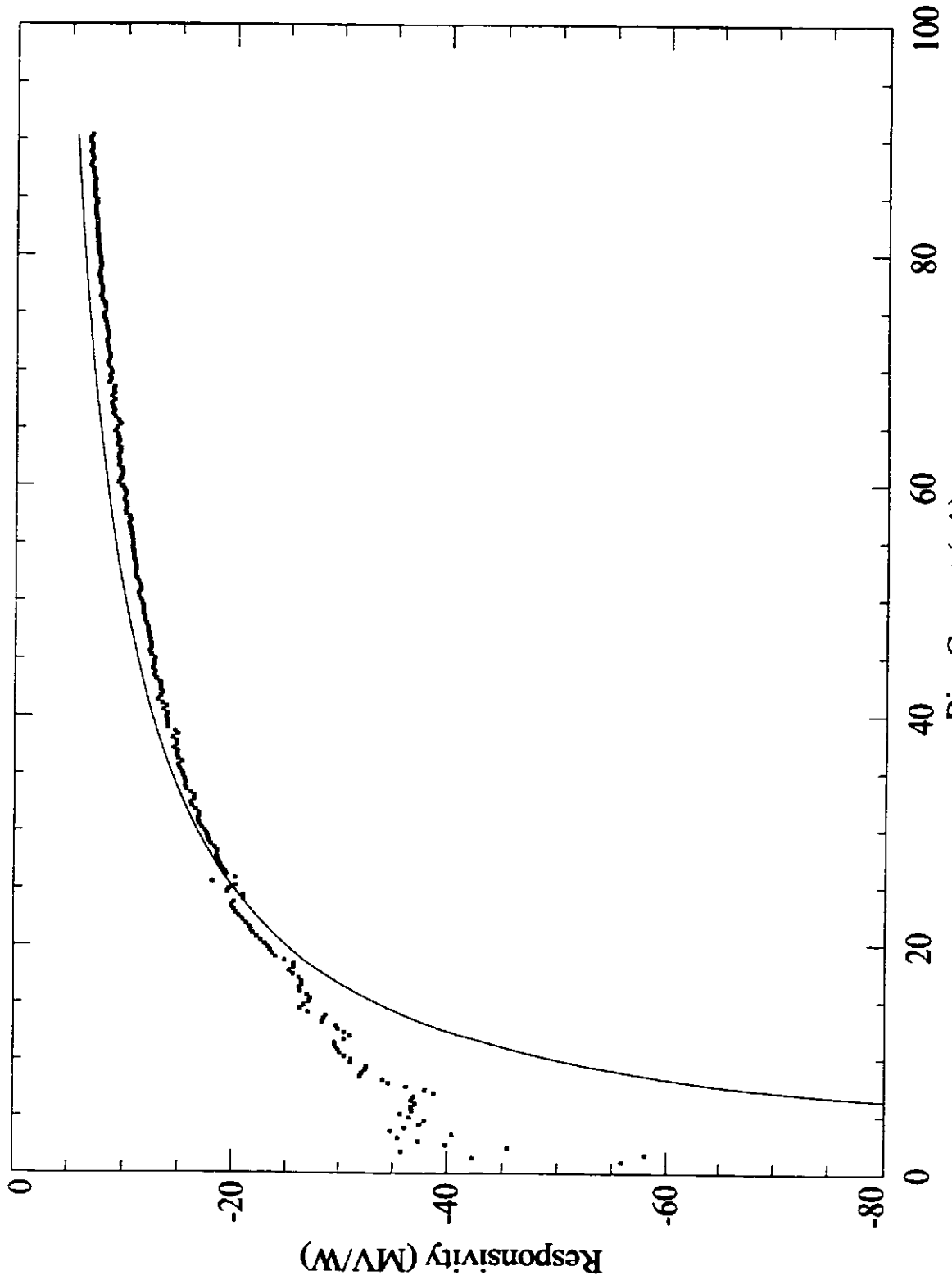

Figure 5.16 : Electrical responsivity as a function of bias current for detector 1. The symbols represent the experimental responsivity calculated from Equation (5.17), the line represents Equation (5.15).

theoretical model is reasonably close to the theoretical curve. Although the responsivity is better (ie. more negative for a negative bolometer) at lower bias currents, the optimum operating bias point is determined from the noise analysis in the following section.

Table 5.6 gives the optical efficiencies, η_{opt}, of the various filters obtained by fitting $S = \frac{\Delta V}{\eta_{opt} \cdot \Delta Q}$ to Equation (5.15). ΔQ was calculated using the Planck function for a blackbody that fills the field of view (see Table 5.3), and integrating over the filter passbands (determined by the spectral analysis carried out in Section 5.7). The quality of the fits obtained is excellent; a typical example is given in Figure 5.17. In addition, the fitted efficiencies agree with the values obtained by analysis of the filter spectral profiles, which is discussed later in Section 5.7.

Table 5.6 : Fit Optical Efficiencies

Filter Band Designation	Efficiency (η_{opt})
350s	0.108
350l	0.101
450	0.122
750	0.134
850	0.160
1100	0.130

5.6 Noise Performance

In this section, the noise performance of the detector is compared to the theoretical noise levels. Noise in the detector signal is the result of several phenomena which can be grouped in the following categories: optical, electrical, and environmental. Since the noise contributions from each source are not correlated, they can be added in quadrature to determine the total detector noise, which is done at the end of this section.

Optical or photon noise is the direct result of the random nature of the arrival rate of photons on a detector. From statistical mechanics, the probability P of n photons being emitted in a time T for time independent coherent light is described by the Poisson probability density function in Equation (5.19). The variance of the probability is denoted by σ^2.

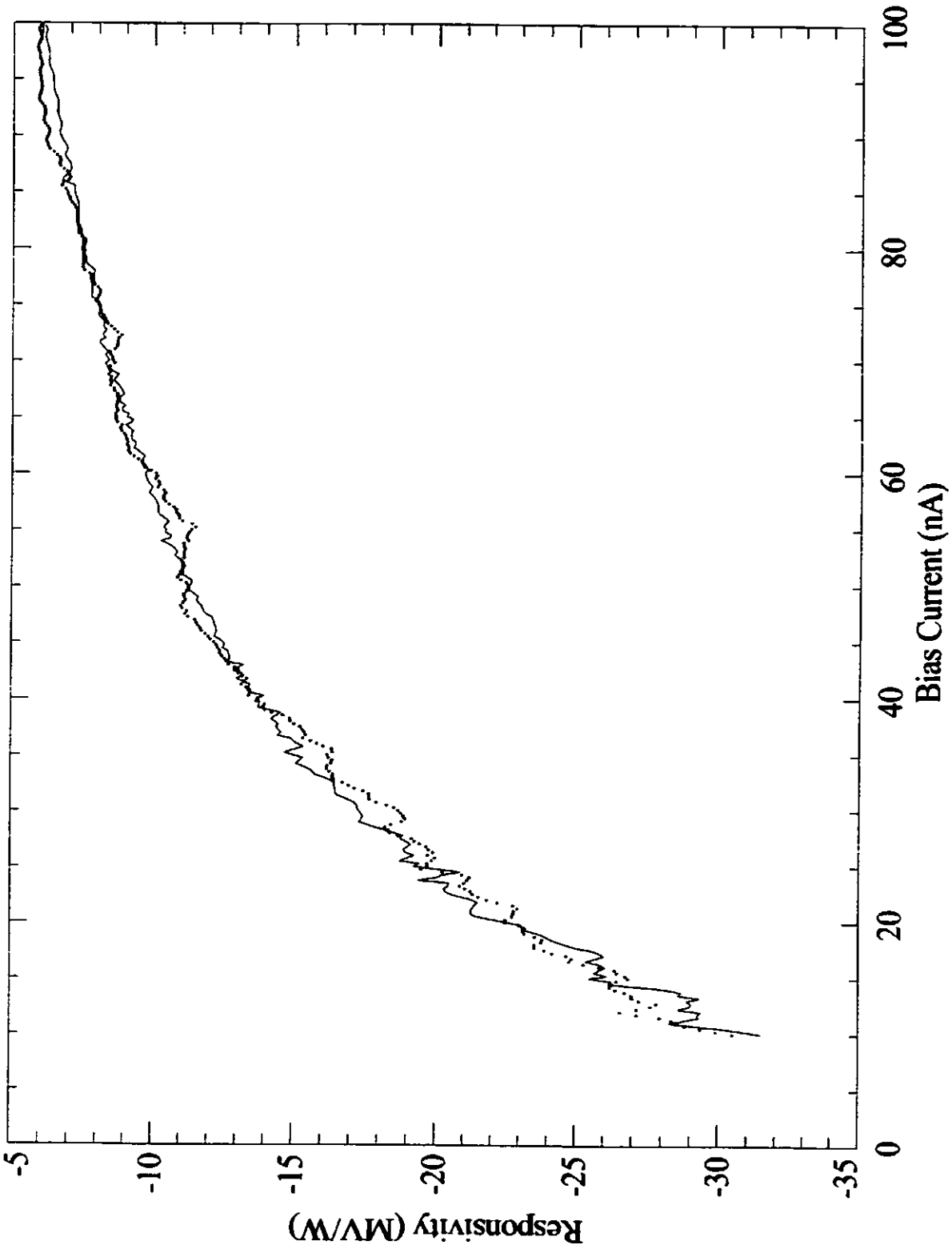

Figure 5.17 : Typical fit of the optical responsivity (symbols) to the electrical responsivity (solid line) calculated from the V-I data.

$$P_{T(n)} = \frac{\bar{n}^2}{n!e^{\bar{n}}} \quad . \tag{5.19}$$
$$\sigma^2 = \overline{n^2} - \bar{n}^2 \quad .$$

For blackbody radiation, the probability distribution for particles of energy u is given by the Bose-Einstein expression, where k is Boltzmann's constant:

$$P_{(u)} = \frac{e^{-u/kT}}{\int_0^\infty e^{-u/kT}} \quad . \tag{5.20}$$

The most probable value for u is the mean, which for photons can be expressed in terms of v:

$$\bar{u} = \frac{\int_0^\infty u e^{-u/kT}\, du}{\int_0^\infty e^{-u/kT}\, du} = \frac{h\nu e^{-h\nu/kT}}{1-e^{-h\nu/kT}} \quad . \tag{5.21}$$

By dividing by the energy per photon, we obtain the mean and mean square number of photons emitted.

$$\bar{n} = \frac{\bar{u}}{h\nu} = \frac{e^{-h\nu/kT}}{1-e^{-h\nu/kT}} \quad . \tag{5.22}$$
$$\overline{n^2} = \frac{\overline{u^2}}{(h\nu)^2} = \frac{e^{-h\nu/kT} + e^{-2h\nu/kT}}{\left(1-e^{-h\nu/kT}\right)^2} \quad .$$

Finally, the variance can be calculated in Equation (5.23) which can be interpreted as the standard Poisson variance multiplied by the Boson factor.

$$\begin{aligned} \sigma^2 &= \overline{n^2} - \bar{n}^2 \\ &= \frac{e^{-h\nu/kT}}{(1-e^{-h\nu/kT})^2} \\ &= \bar{n} \cdot \frac{e^{-h\nu/kT}}{e^{-h\nu/kT} - 1} \\ &= \bar{n} \cdot (\bar{n} + 1) \quad . \end{aligned} \tag{5.23}$$

To get the photon noise, the mean, $\bar{n}$, in Equation (5.23) is replaced by the Planck function:

$$\bar{n} = \frac{B_\nu(T)}{h\nu} \ ,$$

$$\textit{where} \quad B_\nu(T) = \int_\nu \frac{2\nu^2}{c^2}\left(\frac{a\varepsilon f}{e^{-h\nu/kT}-1}\right)d\nu \ .$$

$$\therefore \quad \sigma^2 = \frac{B_\nu(T)}{h\nu}\left(\frac{B_\nu(T)}{h\nu}+1\right)$$

$$= \int_x \frac{4k^3T^3x^2}{h^3c^2}\left(\frac{a\varepsilon f}{e^x-1}\right)\left(\frac{a\varepsilon f}{e^x-1}+1\right)dx \ , \qquad (5.24)$$

$$\textit{where} \quad x = \frac{h\nu}{kT} \ .$$

Equation (5.24) gives the variance in the photon arrival rate from a blackbody source given the following efficiency terms: a is the absorptivity of the detector, ϵ is the emissivity of the background, and f is the transmissivity of the optics. Multiplying by the photon energy hν=xkT, and accounting for the system throughput, AΩ, gives the photon NEP in Equation (5.25).

$$NEP^2_{Photon} = (\sigma \cdot h\nu)^2 = A\Omega \cdot a\varepsilon f \cdot \frac{4k^5T^5}{h^3c^2}\int_x \frac{x^4}{e^x-1}\left(\frac{a\varepsilon f}{e^x-1}+1\right)dx \quad \left(W/\sqrt{Hz}\right)^2 \ . \qquad (5.25)$$

Electrical noise represents the largest category of noise sources. The noise contributions from the various noise generators in the bolometer, bias network, and preamp circuitry were presented in Chapter 3. Using the notation from that Chapter, the Johnson NEP from the bolometer is labelled $NEP_{Johnson}$, the Johnson NEP from the load resistors is labelled NEP_{Load}, the NEP from thermal fluctuations in the bolometer thermal links is labelled NEP_{Phonon}, the NEP from the preamp is labelled NEP_{Preamp}.

When using the detector for astronomical observations, environmental factors provide another source of excess noise. Electrical pickup, while virtually eliminated by the differential design, still must be taken into account and noise from surrounding equipment must be minimized. Atmospheric conditions have a much greater effect on the detector NEP. Turbulence and water vapour levels affect the atmosphere transmission, increasing photon noise and producing modulations in the interferogram. Cosmic ray collisions produce sporadic spikes in the detector signal. All of these noise sources must be compensated for during the analysis of the interferograms as they cannot be completely removed from the signal. Extreme humidity can

even cause frosting of the dewar window which reduces the window efficiency and acts as a blackbody source, preventing serious observing.

The total detector NEP is modelled by adding the contributions from the various noise sources in quadrature, as shown in Equation (5.26). Figures 5.18 and 5.19 show plots of the total NEP for detectors 1 and 2 respectively. Both plots are for the 350s band and a signal frequency of 50 Hz. Excess system and environmental noise is not included in the model.

$$NEP_{Total}^2 = NEP_{Photon}^2 + NEP_{Johnson}^2 + NEP_{Phonon}^2 + NEP_{Preamp}^2 + NEP_{Load}^2 + NEP_{Excess}^2 \quad \left(W/\sqrt{Hz}\right)^2 . \quad (5.26)$$

5.6.1 Analysis

A commonly used method of determining the experimental NEP is dividing the incident power by the signal to noise ratio (S/N). For this test the detector alternately viewed liquid nitrogen and ambient sources at a chopping frequency of ~ 40 Hz. An oscilloscope was used to measure the chopped signal amplitude. The noise was measured with a spectrum analyser [8] as the detector viewed each source individually. The power incident on the bolometers was calculated from theory for a blackbody source filling the field of view. The spectrum analyser was configured to compute the noise power spectrum in rms $nV/\sqrt{Hz}$ using a FFT with a Hanning filter [9]. Since the spectrum analyser could not produce a hard copy of the results, noise values were determined by averaging the noise spectrum over a range of 70 to 110 Hz. This range was chosen to provide a reasonable estimate of the detector noise voltage at the signal frequencies of the FTS, while avoiding including the low frequency 1/f and 60 Hz noise in the average. Measurements were taken for a range of bias currents for both detectors and all filters.

5.6.2 Results

Since the detector signal and noise data sets are sparse, exponentials were fitted to both data sets in order to allow interpolation for the S/N calculation (and not to imply any physical meaning). The noise as a function of bias for both detectors is shown in Figures 5.20 and 5.21. In these figures, the symbols represent the bolometer noise voltage averaged over the 6 filter bands, the curves show the best exponential fits, and the vertical lines represent 1 σ error bars for each bias point. It can be seen that the noise does not differ significantly when the detector is viewing ambient or LN_2 sources, however, detector 1 is approximately twice

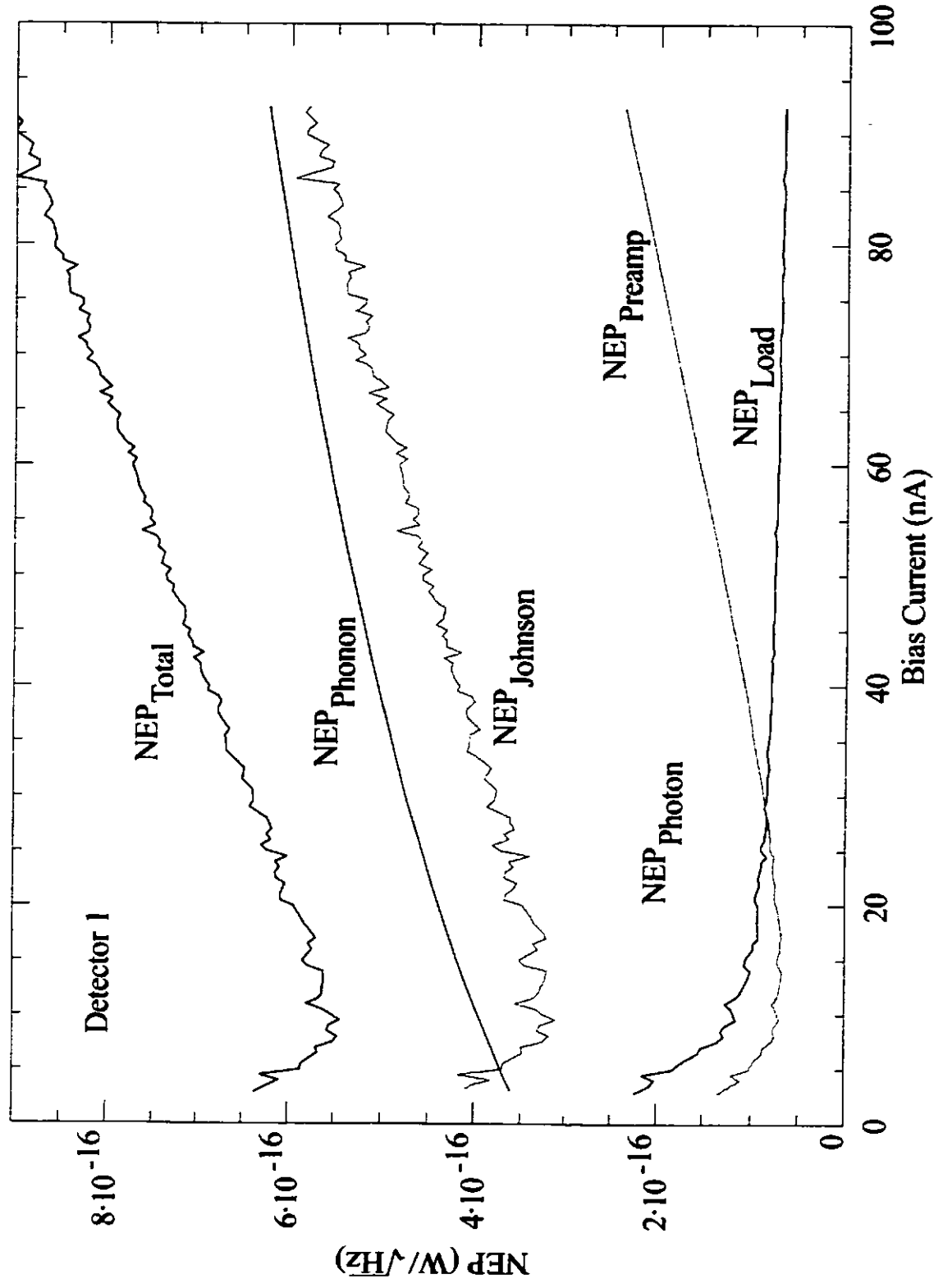

Figure 5.18 : Total system NEP model (neglecting excess noise) for detector 1 and the 350s band, with an operating frequency of 50 Hz. The photon noise limit is for a 73 K source filling the field of view.

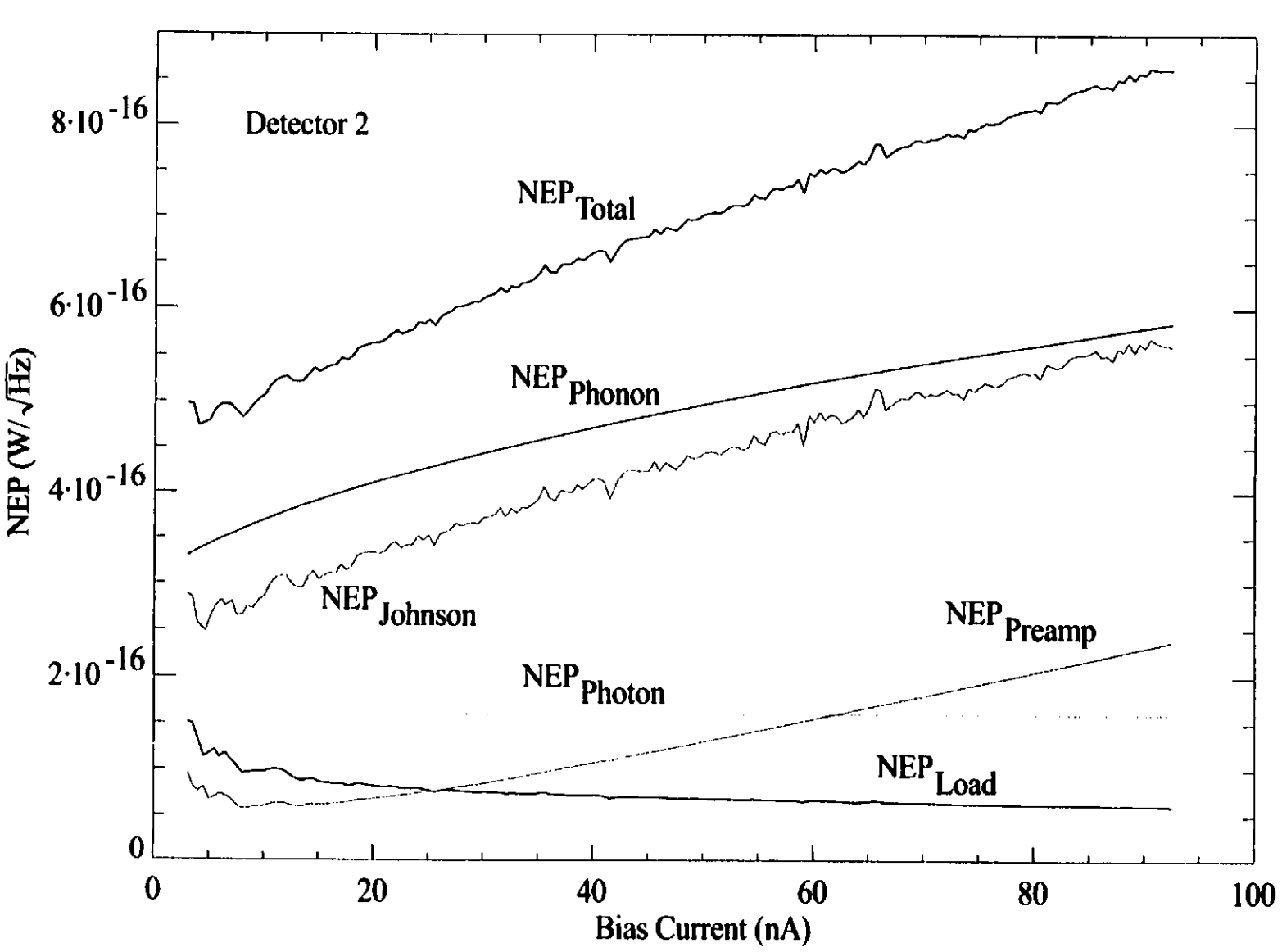

Figure 5.19 : Total system NEP model (neglecting excess noise) for detector 2 and the 350s band, with an operating frequency of 50 Hz. The photon noise limit is for a 73 K source filling the field of view.

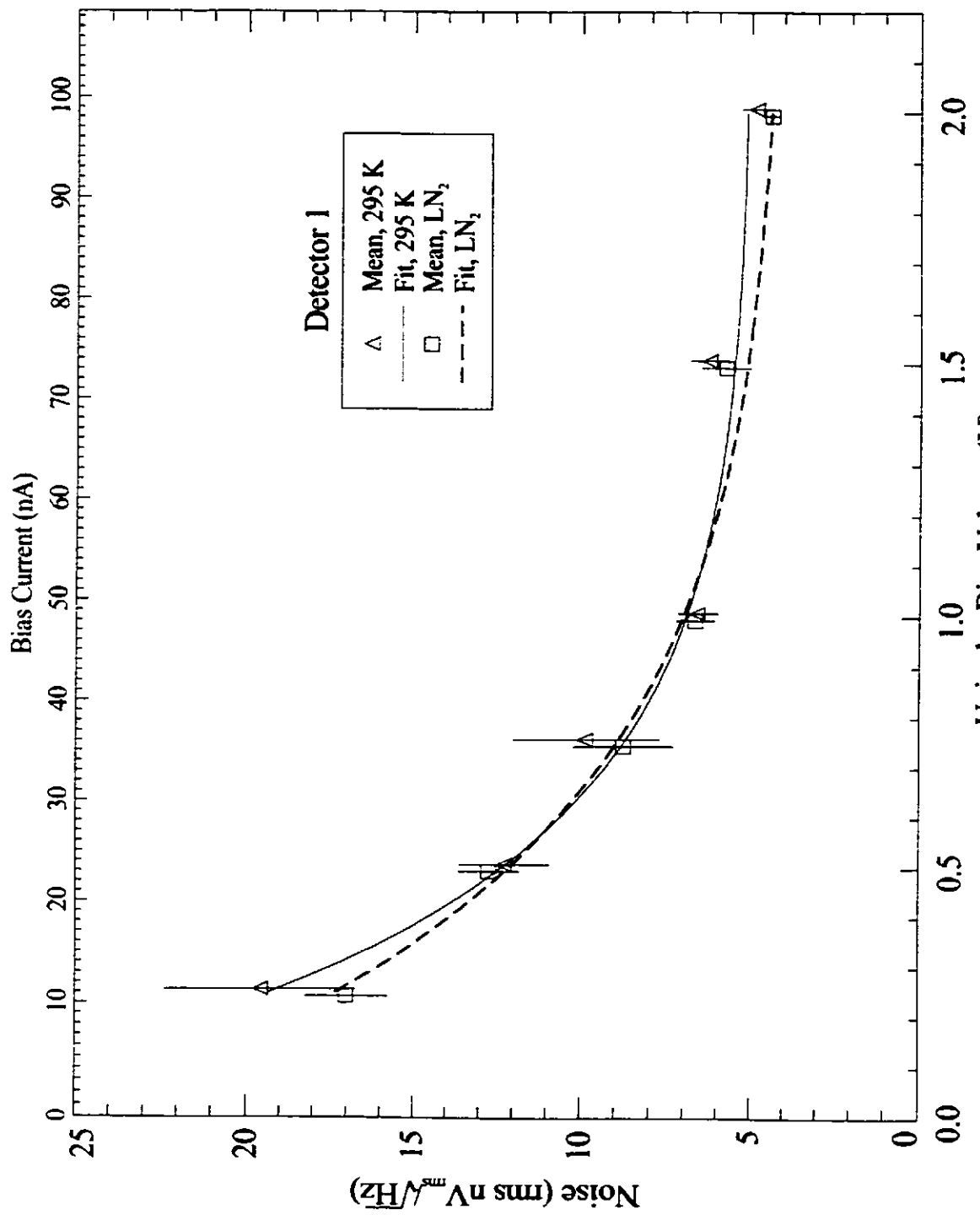

Figure 5.20 : Noise as a function of unipolar bias voltage averaged over the filter bands for detector 1 viewing ambient and LN_2 sources. Symbols represent the mean values, vertical lines represent 1-σ error bars, and curves represent the best fits.

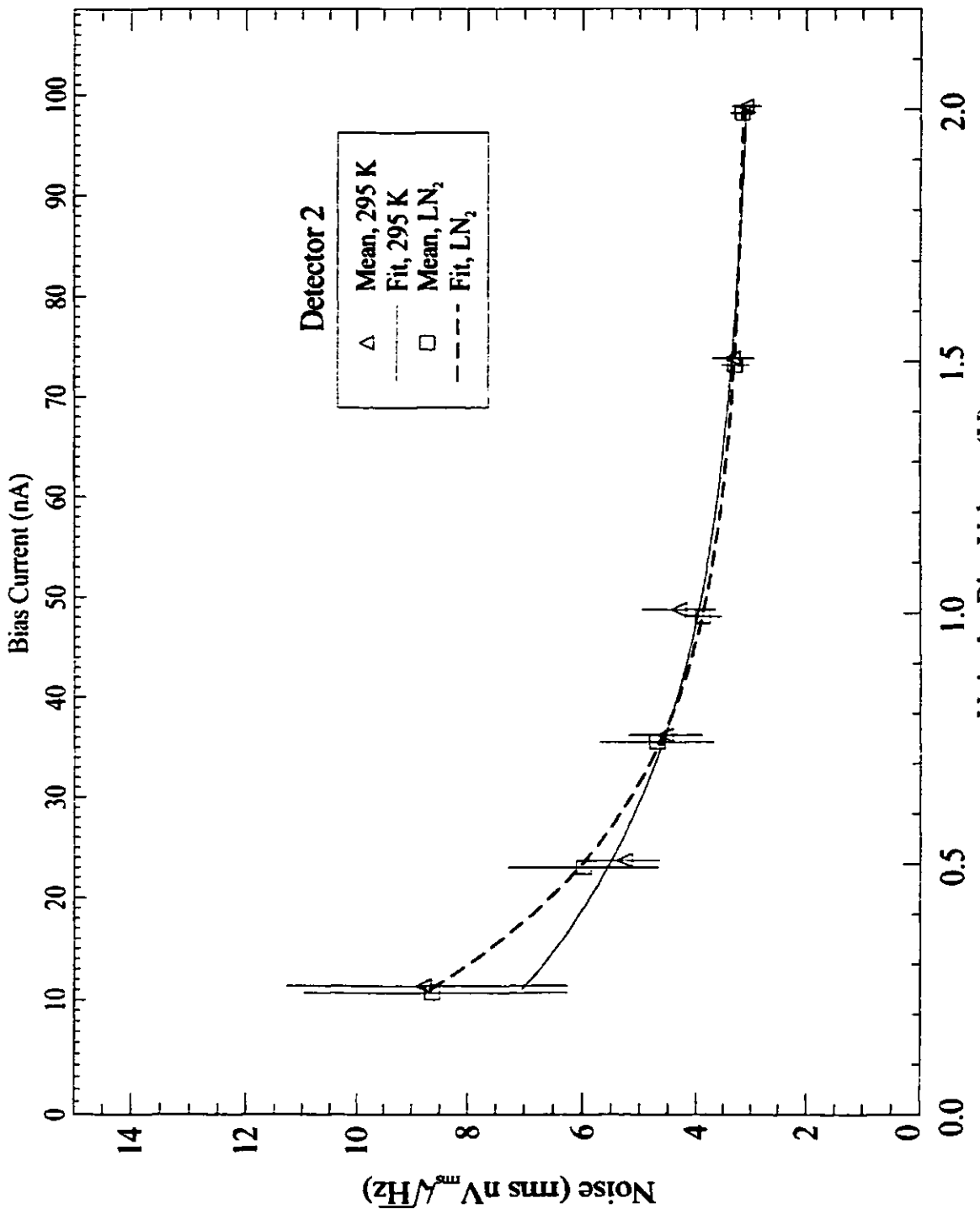

Figure 5.21 : Noise as a function of unipolar bias voltage averaged over the filter bands for detector 2 viewing ambient and LN_2 sources. Symbols represent the mean values, vertical lines represent 1-σ error bars, and curves represent the best fits.

as noisy as detector 2. The calculated power difference incident on the bolometer element was given previously in Table 5.4.

The chopped detector signal as a function of bias voltage for both detectors, and the fitted exponentials, are shown in Figure 5.22. This figure is for the 350s band, but the quality of the fit is typical for all bands. By dividing the fitted signal by the fitted noise, the S/N as a function of bias voltage is determined. Typical curves for both detectors are shown in Figure 5.23. The detector NEP is then calculated by dividing the calculated rms power difference incident on the bolometer by the S/N. Table 5.7 gives the maximum s/n (when viewing a 73 K source), minimum NEP , and optimum operating bias voltage (corresponding to maximum S/N) for both detectors and all filters except the 750 and 1100 filters which were not tested.

Table 5.7 : Optimum S/N, NEP, and Operating Bias Voltage

Filter Band	Maximum S/N		Min. NEP ($W_{rms}/\sqrt{Hz}$)		Optimum Bias Voltage	
	Detector 1	Detector 2	Detector 1	Detector 2	Detector 1	Detector 2
350s	$1.6 \cdot 10^{4}$	$3.0 \cdot 10^{4}$	$13.2 \cdot 10^{-16}$	$7.0 \cdot 10^{-16}$	1.031	0.856
350l	$4.1 \cdot 10^{4}$	$7.5 \cdot 10^{4}$	$14.2 \cdot 10^{-16}$	$7.7 \cdot 10^{-16}$	1.055	0.874
450	$3.7 \cdot 10^{4}$	$6.7 \cdot 10^{4}$	$15.1 \cdot 10^{-16}$	$8.3 \cdot 10^{-16}$	1.037	0.862
850	$1.8 \cdot 10^{4}$	$3.6 \cdot 10^{4}$	$10.8 \cdot 10^{-16}$	$5.4 \cdot 10^{-16}$	1.049	0.874
1400	$2.7 \cdot 10^{4}$	$5.2 \cdot 10^{4}$	$14.3 \cdot 10^{-16}$	$7.4 \cdot 10^{-16}$	1.049	0.880

An alternate method of determining the NEP is to divide the detector noise voltage by the responsivity of the detector. If we use the noise voltages given in Figures 5.20 and 5.21 with the responsivity given by Equation (5.17), we obtain Figure 5.24, which is typical for all the filters. This method produces NEPs in the same range as the other methods (see below), but produces optimum operating bias currents that are slightly smaller than those in Table 5.7.

5.6.3 Noise Summary

The theoretical minimum NEP for a bolometer is given by Equation (5.27) [10].

$$NEP_{min} = aT_0\sqrt{kG_0} + bQ\sqrt{k/G_0} \qquad \left(W/\sqrt{Hz}\right) . \tag{5.27}$$

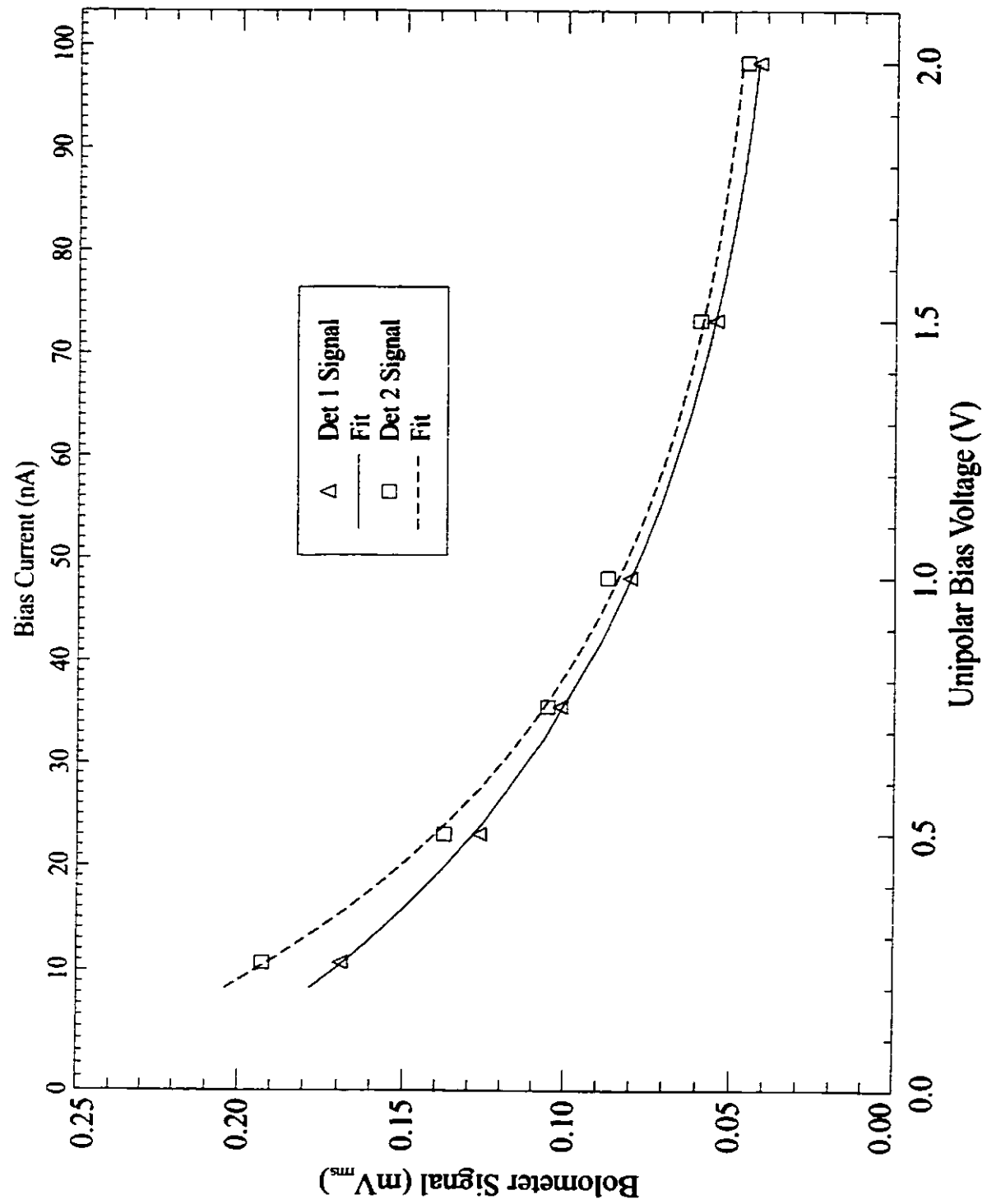

Figure 5.22 : Typical chopped bolometer signal as a function of bias voltage for both detectors. The symbols represent the raw data, the lines are best fits to exponentials.

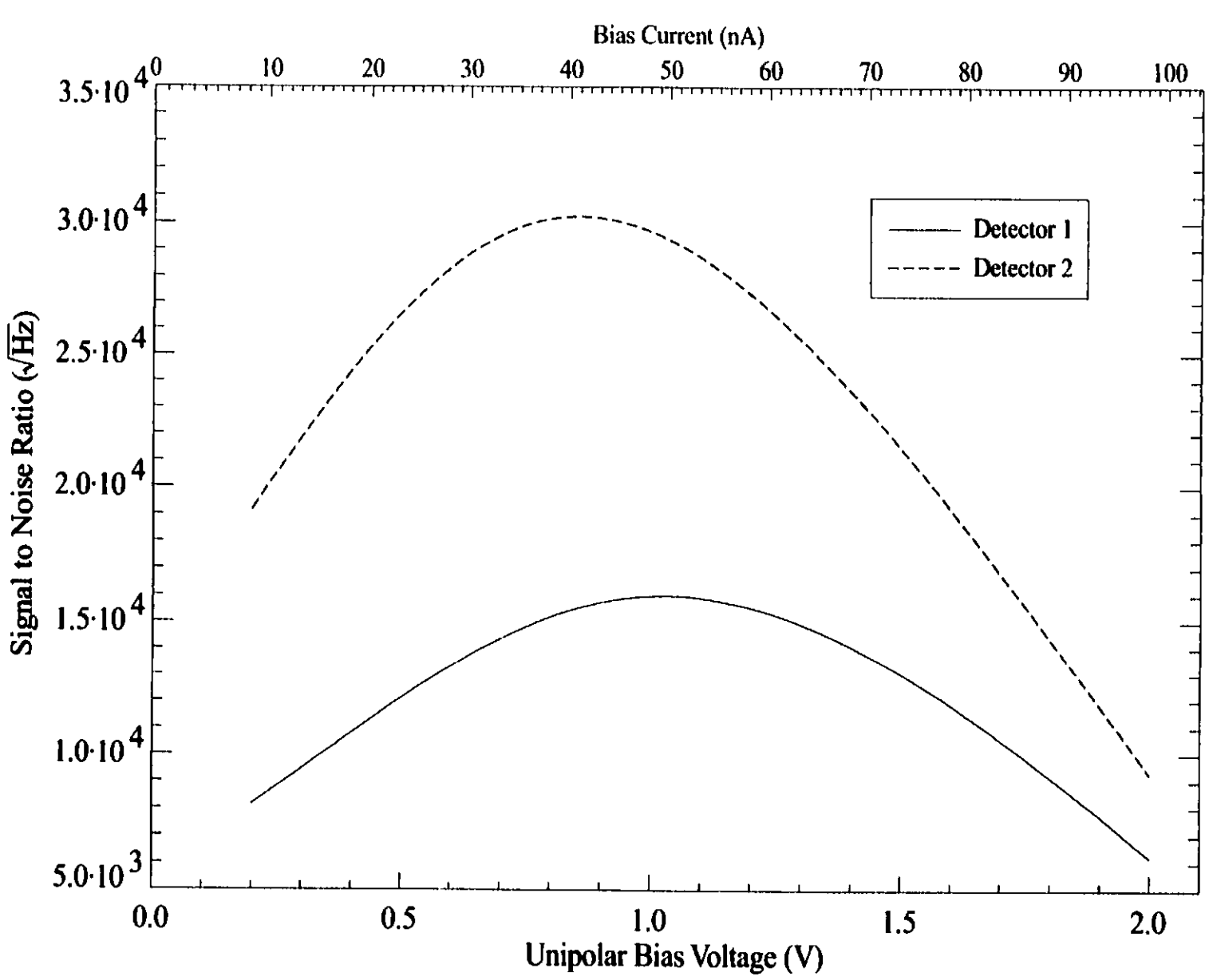

Figure 5.23 : Typical chopped signal-to-noise ratios for both detectors. The lines represent the exponential fitted to the average noise divided by the exponential fitted to the chopped signal.

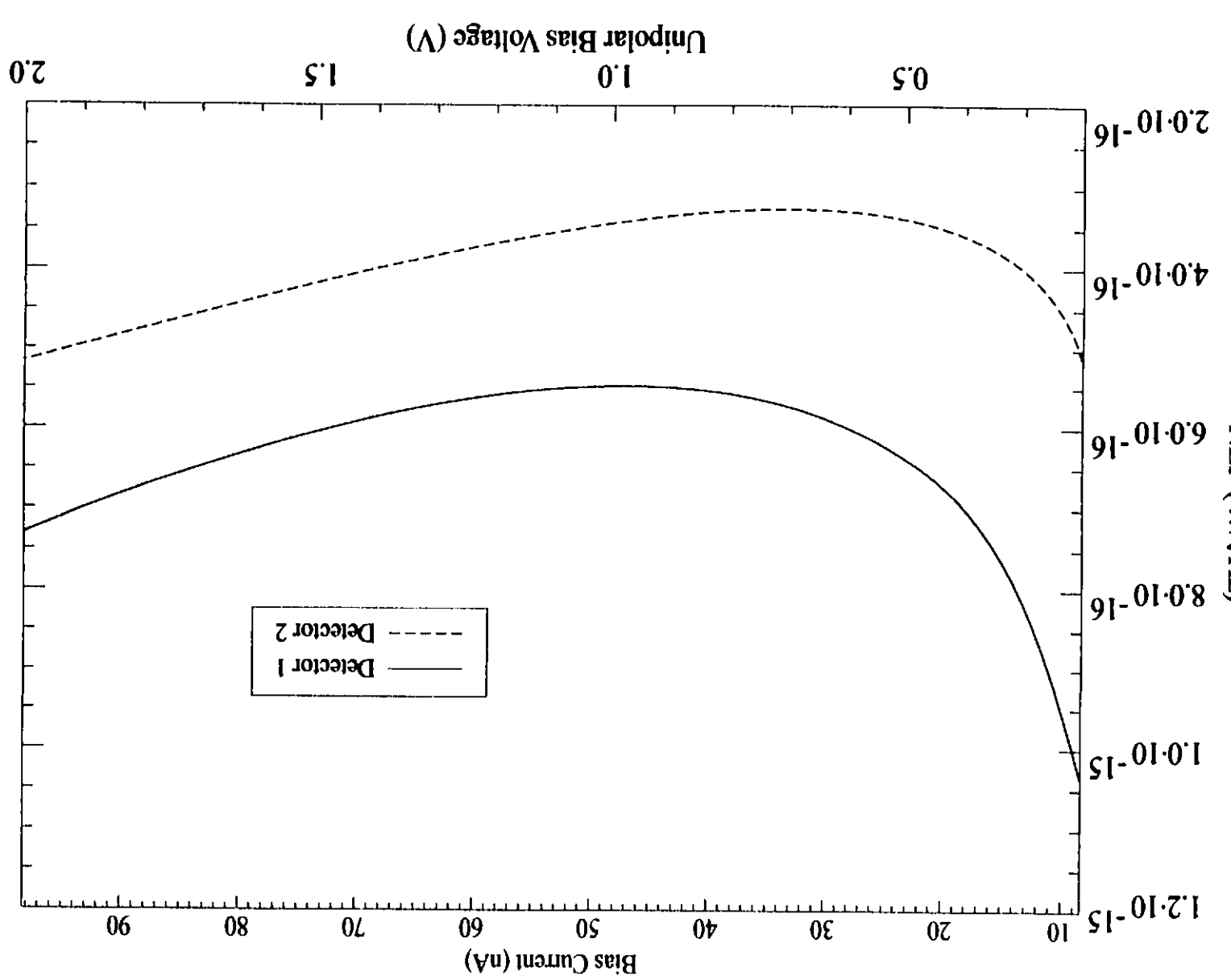

Figure 5.24 : Detector NEP obtained by dividing the chopped source noise voltage by the detector responsivity.

In this equation, a and b are dependant on the bolometer material and temperature. For our detector, $a = 2.52$ and $b = 3.31$ [10]. Using the values for G_0, T_0, and Q determined by the V-I fitting procedure (Section 5.4), the theoretical minimum NEP is consistent with the other NEP values we have calculated. Table 5.8 lists the NEPs determined by the four methods described in this chapter. From the table it can be seen that there is good agreement in the results, despite the dissimilarity of the methods used to derive them. The typical minimum NEP is $\sim 5 \cdot 10^{-16}$ $W/\sqrt{Hz}$, although the Power/Signal-to-Noise calculation provides a higher NEP (this discrepancy is likely due to the uncertainty in the incident power calculation). For every test, detector 2 is shown to have a lower NEP than detector 1, due in part to the lower temperature of the bolometer element. For comparison, the predecessor of this detector, UKT14, and SCUBA, a bolometric array operating at 100 mK, have theoretical minimum NEPs at the bolometer element of $5 \cdot 10^{-16}$ and $6 \cdot 10^{-17}$ $W/\sqrt{Hz}$, respectively. A more significant comparison of these detectors is presented in the next section, where the spectroscopic performance is discussed.

Table 5.8 : Minimum Detector NEP

Calculation Method	Minimum NEP ($W/\sqrt{Hz}$)	
	Detector 1	Detector 2
V-I Analysis (Equation (5.26))	$6.5 \cdot 10^{-16}$	$6.2 \cdot 10^{-16}$
Noise/Responsivity (Figure 5.24)	$5.6 \cdot 10^{-16}$	$3.5 \cdot 10^{-16}$
Power/Signal-to-Noise (Table 5.7)	$10.8 \cdot 10^{-16}$	$5.4 \cdot 10^{-16}$
Theoretical Minimum (Equation (5.27))	$4.5 \cdot 10^{-16}$	$4.1 \cdot 10^{-16}$

5.7 Spectral Analysis

The detector described in this thesis was designed specifically for use with a dual input port, polarizing FTS. In previous sections we have quantified the performance of the detector when used in photometric applications. However, it is more important to know what noise performance can be achieved when the detector is used spectroscopically. In this section, spectra obtained with the detector in conjunction with a polarizing FTS are analysed to determine the bandwidths and efficiencies of the various filters. The spectral noise is also analysed to provide a measure of the full system NEP. A detailed analysis of the astronomical spectra obtained with this system, however, is beyond the scope of this thesis.

5.7.1 Filter Characteristics

Spectra obtained when viewing a blackbody source provide the only means of determining the actual filter passbands of the detector system. In addition, they provide a method of verifying the detector efficiencies calculated by the V-I fitting procedures, since the optical throughput of the spectrometer is known.

The filter passbands used for all the incident power calculations in the previous sections were defined by the following process: Spectra for the various filters were obtained using the FTS, with one input port viewing an ambient (280 K) source, and the other viewing a LN_2 bath (73 K). The spectra for each of the filters were averaged, and each average spectrum was integrated as a function of wavenumber. The point at which the integral reached half the maximum value was used as the band centre. The width of the filter band was defined as the spectral area divided by the maximum spectral value, so that for a Gaussian filter profile the band edges coincide with the half-maximum points of the profile (a condition that is not necessarily met for the distinctly non-Gaussian long wavelength filters). All filter efficiencies used in this thesis are relative to these filter passbands. Table 5.9 gives the filter band parameters.

Table 5.9 : Filter Band Parameters

Filter Band	Band Centre (cm^{-1})	Band Width (cm^{-1})	Low Edge (cm^{-1})	High Edge (cm^{-1})
350s	29.36	1.07	28.82	29.89
350l	27.72	2.84	26.30	29.14
450	22.31	2.30	21.16	23.46
750	13.40	0.92	12.94	13.86
850	11.63	0.88	11.19	12.07
1100	9.45	1.57	8.66	10.23
1400	8.04	1.86	7.11	8.97

Profiles for the various filters were measured by QMW before they were installed in the detector, and were shown previously in Figures 3.5 and 3.6. These profiles are only an estimate of the detector system spectral performance; the filter characteristics can change as the filters are cooled to 4 K, and channel fringes

[11] produced by resonant optical cavities within the dewar cannot be modelled accurately. For example, comparison of the 350s profile with the measured spectra reveals that the passband for this filter shifted down by one wavenumber when cooled.

Since there was no opportunity to measure the detector signal with the filters removed, and the power incident on the dewar window is not known precisely, the absolute amplitudes of the spectra measured by our tests are not calibrated (the relative amplitudes of the filter profiles, however, are calibrated). Consequently, we assume that the filter transmission obtained by multiplying the profiles of the 350l filter, associated edge filters, and window given in Figures 3.5 and 3.6, is reasonable. The measured spectra are then normalized so that the amplitude of the measured 350l filter profile matches that calculated from the QMW data, and all the profiles retain their relative amplitudes.

In order to use the measured bandwidths for radiant power calculations, the efficiencies relative to these bandwidths must be calculated. First, the total power from a blackbody filling the field of view is calculated by integrating the Planck function over the filter bandwidth. Next, the power transmitted by a filter is calculated by integrating the filter profile, multiplied by the Planck function, over all available wavelengths. The filter efficiency is then simply the ratio of the transmitted power to the total power. The total system efficiency is calculated by multiplying the theoretical values tabulated in Table 5.10 by the filter efficiency. Thus, the power incident on a bolometer element from a blackbody source is calculated by integrating the Planck function over the given filter band, and multiplying by the total system efficiency.

Table 5.10 : Component Efficiencies

Component	Efficiency
Bolometer Quantum Efficiency	0.9
Winston Horn	0.9
Polarizer	0.5
Field Lens	0.92
Rooftop Mirror	0.94
Total	0.35

A list of filter efficiencies is given in Table 5.11. The values calculated by this method agree well with the efficiencies obtained using the detector responsivity (see Table 5.6).

Table 5.11 : Filter and System Efficiencies

Filter Band	Filter Efficiency	Total System Efficiency
350s	0.297	0.104
350l	0.354	0.124
450	0.389	0.136
750	0.429	0.150
850	0.437	0.153
1100	0.389	0.136

5.7.2 Spectral Noise Analysis

The ultimate measure of the detector system performance is the quality of the spectra obtained when it is used in conjunction with the FTS. SCUBA [12], the bolometric detector array recently commissioned at the JCMT, uses bolometer units similar to those used in this detector, but cooled to 100 mK. SCUBA also uses a 850 μm filter identical to the one in this detector. Although the SCUBA bolometers have a higher intrinsic sensitivity due to their lower operating temperature, they use single-ended electronics. As a result, the SCUBA detectors are highly sensitive to electrical noise from the telescope environment. Figure 5.25 shows a comparison between a single spectrum obtained with the detector system described in this thesis (lower plot), and the average of 20 spectra obtained with one of the pixels of the SCUBA system (upper plot). In this comparison, the operating environment, 850 μm filter, FTS, and source used were identical. The advantage of the fully differential electronics system is clearly seen as the significant electrical noise evident in the SCUBA spectra is virtually nonexistent in the differential system spectrum. The noise for the differential system is white (spectrally flat), with only a small noise feature at 60 Hz (30 cm^{-1}).

The main design goal in the construction of this detector system was to improve on the spectroscopic capabilities of its predecessor, UKT14 [13]. UKT14 is a JCMT facility bolometric detector (recently retired), originally designed for photometric measurements. While UKT14 has an intrinsic NEP of $\sim 5 \cdot 10^{-16}$ $W/\sqrt{Hz}$, this ideal NEP limit was never achieved when the detector was used for spectroscopic measurements with a

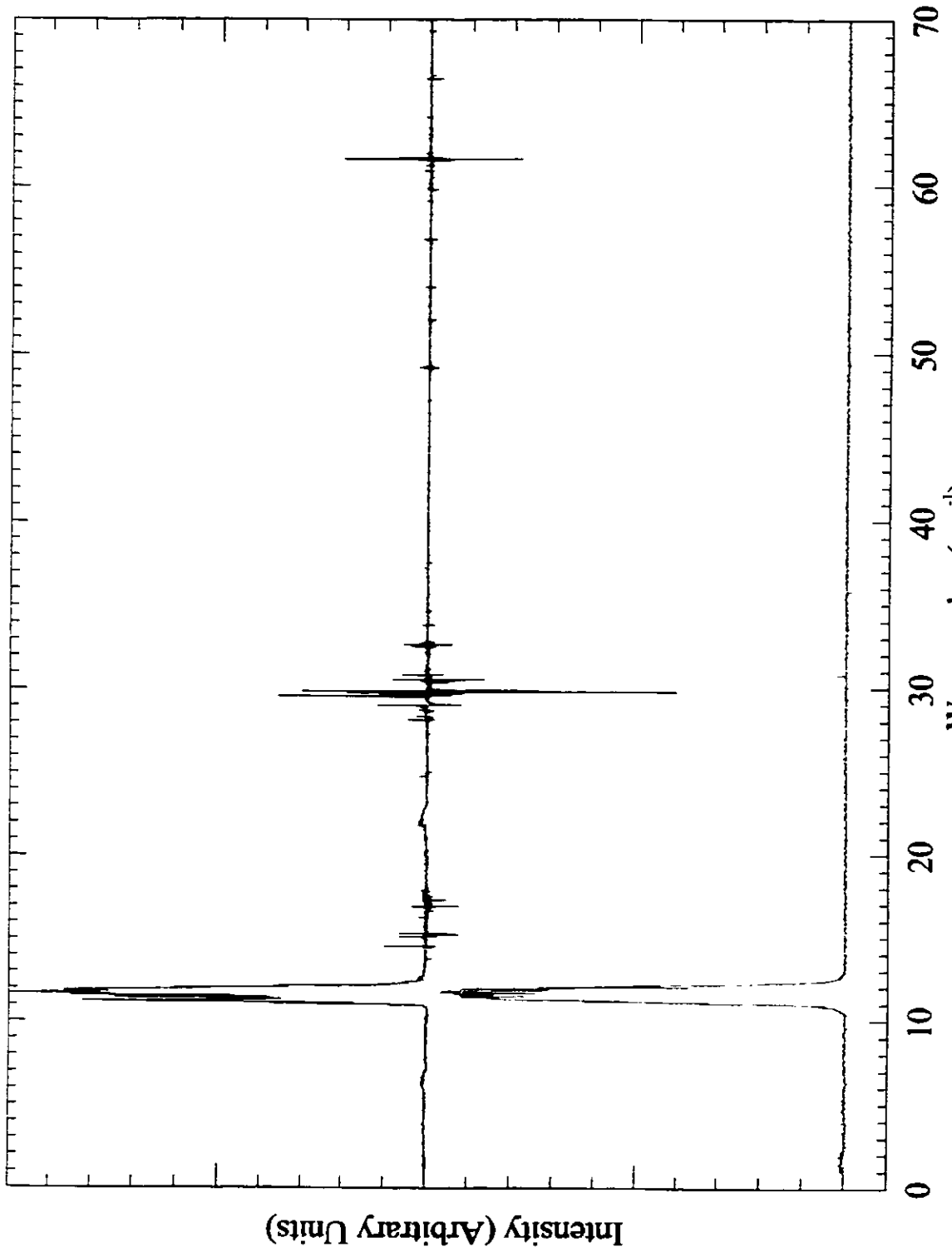

Figure 5.25 : Comparison of a single spectrum obtained with the differential detector system (lower plot), with the average of 20 spectra obtained with a SCUBA detector.

FTS . Figure 5.26a shows spectra obtained with the UKT14 FTS system [14], using the 450 μm filter. In the figure, the top line represents the synthetic atmospheric transmission spectrum (modelled for Mauna Kea with 1 mm precipitable water vapour), the middle line represents the average of four solar spectra (total integration time of 3 minutes), and the bottom line represents the calibration blackbody spectrum. For comparison, Figure 5.26b shows the corresponding single spectrum recorded with the current detector and the same FTS (total integration time of 1 minute), where the top line is the synthetic atmospheric spectrum, and the lower line is a single solar spectrum. Atmospheric conditions were similar for both sets of observations. While the UKT14 spectra and synthesis are of lower resolution (0.0125 cm^{-1}) than the spectrum from the new system (0.004 cm^{-1}), the S/N in the latter spectrum is clearly better. The factors that most adversely affect the quality of the UKT14 spectra are electrical noise inherent to the single-ended electronics design, microphonic pickup, and fringes caused by resonant cavities within the detector optics [11].

The blackbody calibration spectra described in the previous section were analysed to determine the NEP of the detector-FTS system. For a FTS, the S/N in a spectral element is related to the detector NEP by Equation (5.28) [15], where P is the power in a spectral element, and T is the integration time of the interferogram.

$$\frac{S}{N} = \frac{P}{NEP}\sqrt{\frac{T}{4}} \quad . \tag{5.28}$$

Since the power from a blackbody source is related to the temperature through the Planck function, this equation can rewritten in terms of the NEP at the bolometer [15] as Equation (5.29), where N is the number of averaged interferograms, ΔT is the 1 σ rms temperature error in a 150 MHz bandwidth, and ε is the total detector system efficiency (see Table 5.11). This equation assumes a FTS efficiency of 100 %.

$$NEP = 5.67 \cdot 10^{-14} \sqrt{N} \cdot \Delta T \cdot \varepsilon \quad . \tag{5.29}$$

Figure 5.27a shows the average of 6 blackbody calibration spectra for detector 1 with the 850 μm band (thick line), and the standard deviation in each resolution element (thin line). Figure 5.27b shows the corresponding average for detector 2. These graphs are typical of all the filter bands, and indicate that the noise is white in the entire spectral region of each filter. Using the S/N calculated from the maximum spectral

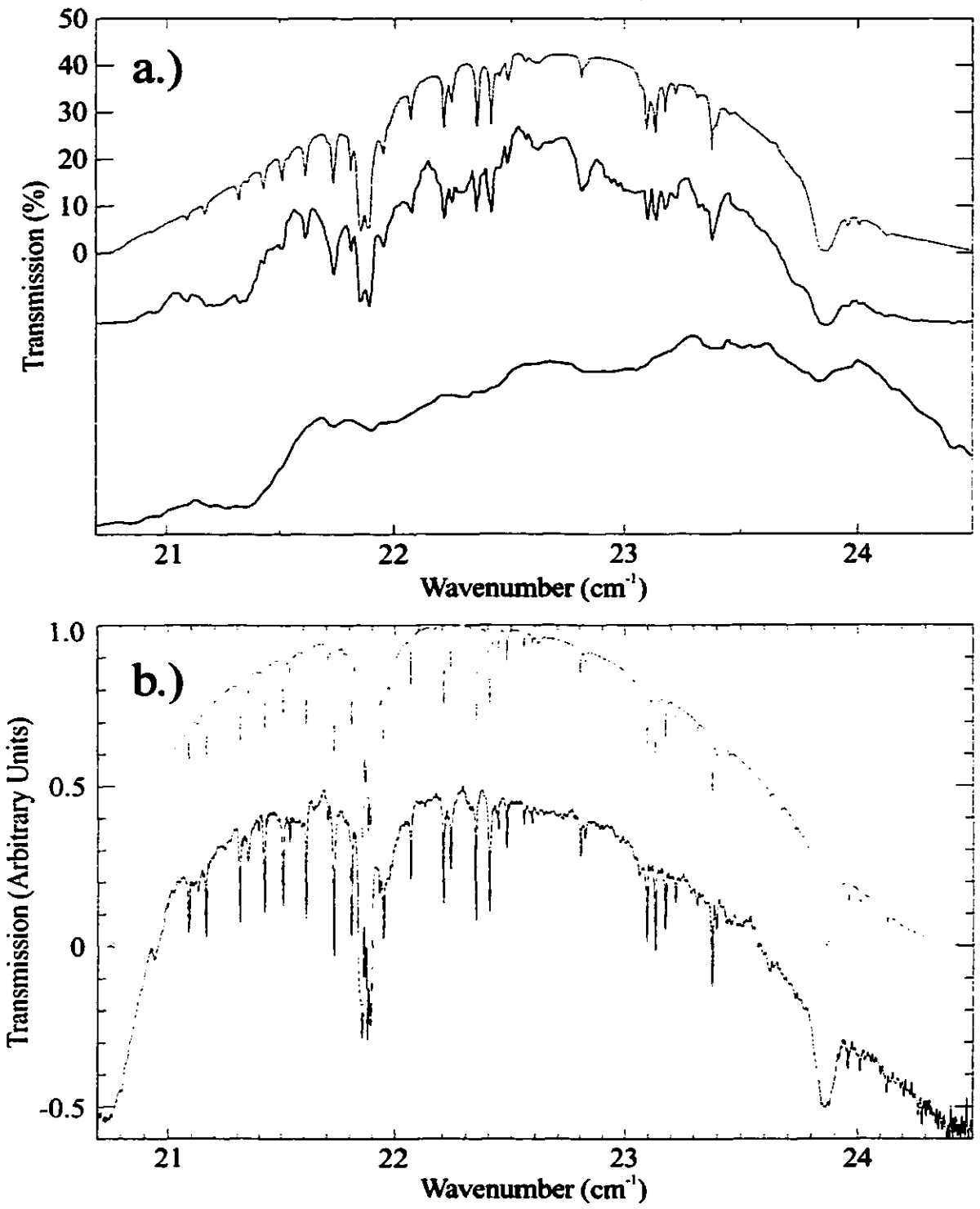

Figure 5.26: a.) UKT14 850 μm spectra, from top to bottom: Synthetic atmospheric transmission, average of 4 solar spectra, blackbody calibration. b.) Spectra for the current system. Top: Synthetic atmospheric transmission spectrum. Bottom: Single solar spectrum.

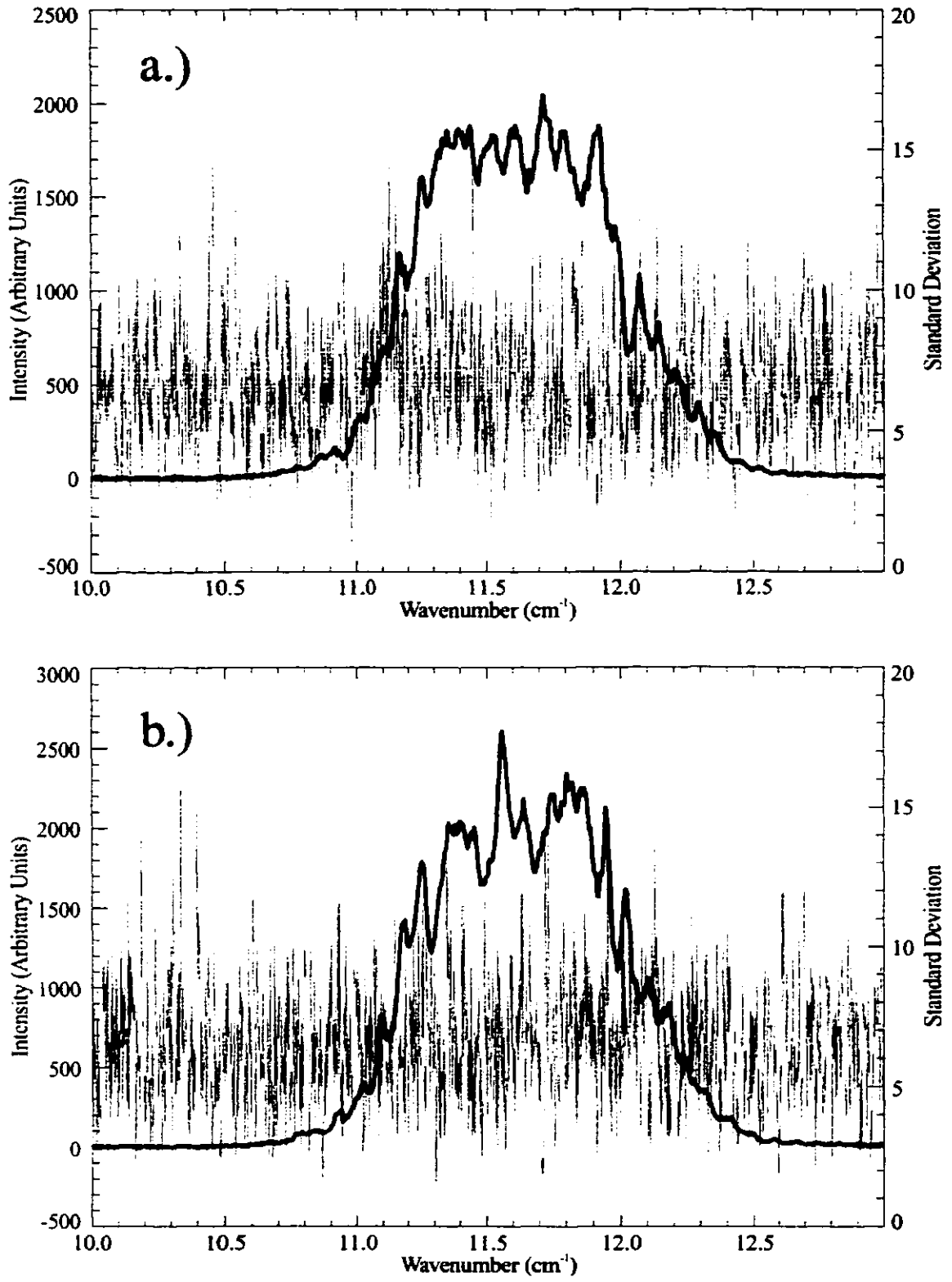

Figure 5.27: Average blackbody calibration spectra obtained with the current system. In each figure, the thick line represents the average of 6 spectra, and the thin line represents the standard deviation error per resolution element. a.) Detector 1, 850 μm. b.) Detector 2 , 850 μm.

intensity and the average noise in the band, we tabulate the NEPs calculated from Equation (5.29) in Table 5.12.

Table 5.12 : FTS System NEP

Filter Band	Detector 1 NEP ($W/\sqrt{Hz}$)	Detector 2 NEP ($W/\sqrt{Hz}$)
350s	$1.02 \cdot 10^{-15}$	$0.72 \cdot 10^{-15}$
350l	$1.38 \cdot 10^{-15}$	$1.02 \cdot 10^{-15}$
750	$1.25 \cdot 10^{-15}$	$1.01 \cdot 10^{-15}$
850	$1.39 \cdot 10^{-15}$	$1.10 \cdot 10^{-15}$
1100	$2.00 \cdot 10^{-15}$	$1.38 \cdot 10^{-15}$

While these values are larger than those predicted in the detector noise analysis section, they represent the total FTS system noise when in operation on the noisy telescope Nasmyth platform. In addition, these values are upper limits since the actual FTS efficiency is less than 100 %.

5.8 Conclusion and Summary of Detector Operating Parameters

The test results described in this chapter have shown that the detector system achieves the design goals of low noise, high sensitivity, and fast frequency response. The advantages of the differential electronics system have been made clear by the low detector noise levels, and elimination of electrical interference features in the measured spectra. The combination of these results indicate that this detector system is currently the most sensitive ^{3}He bolometric detector designed for submillimetre astronomical Fourier Transform Spectroscopy at a ground-based telescope. In addition to the performance features of the detector, the cryogenic system has been proven to be reliable, and has been optimized for cycling efficiency and made easy to operate with the software described in Chapter 4. A list of the detector performance parameters and ideal operating points determined in this chapter are given in Table 5.13.

Table 5.13 : Summary of Detector Parameters

	Detector 1	Detector 2
Minimum Electrical NEP (V-I analysis)	$6.5 \cdot 10^{-16}$ W/$\sqrt{\text{Hz}}$	$6.2 \cdot 10^{-16}$ W/$\sqrt{\text{Hz}}$
Minimum Optical NEP ($^{Q}/_{S/N}$)	$10.8 \cdot 10^{-16}$ W/$\sqrt{\text{Hz}}$	$5.4 \cdot 10^{-16}$ W/$\sqrt{\text{Hz}}$
Minimum NEP (Noise/Responsivity)	$5.6 \cdot 10^{-16}$ W/$\sqrt{\text{Hz}}$	$3.5 \cdot 10^{-16}$ W/$\sqrt{\text{Hz}}$
Minimum NEP (Spectral Analysis)	$10.2 \cdot 10^{-16}$ W/$\sqrt{\text{Hz}}$	$7.2 \cdot 10^{-16}$ W/$\sqrt{\text{Hz}}$
Theoretical Minimum NEP	$4.5 \cdot 10^{-16}$ W/$\sqrt{\text{Hz}}$	$4.1 \cdot 10^{-16}$ W/$\sqrt{\text{Hz}}$
Typical Optimum Bias Point	1.04 V unipolar, ~50 nA	0.86 V unipolar, ~41 nA
Electrical Noise Density at Optimum Bias	8 $nV_{rms}/\sqrt{Hz}$ @ 70 Hz	4.5 $nV_{rms}/\sqrt{Hz}$ @ 70 Hz
Electrical Responsivity at Optimum Bias	-11 MV/W	-13 MV/W
Measured Cutoff Frequency (F_{3dB})	52.2 Hz	108.6 Hz
Thermal Conductivity (G_0)	23.5 nW/K	19.4 nW/K
Zero Loading Bolometer Temperature (T_0)	0.294 K	0.290 K
Bolometer Heat Capacity (C)	143 pJ/K	56.9 pJ/K
Cryogenic System Recycling Time	< 2 Hours	
^{3}He Hold Time	> 39 Hours	
LN_2 Consumption per Cycle	< 0.5 Litre	
L^{4}He Consumption per Cycle	< 1 Litre	

Another significant result of this project, in addition to the quantification of the detector system performance, has been the development of software tools for the analysis and visualization of bolometer V-I curves. While no new theory in bolometer operation has been presented here, to my knowledge no other groups to date have modelled experimental bolometer V-I curves with such high precision. The theoretical V-I analysis performed in this chapter was greatly simplified by the use of a high-level graphical programming language such as IDL.

5.9 Future Considerations

The relatively small amount of data collected for this thesis was the consequence of the extremely limited access to the detector system. An emphasis was therefore placed on making the most use of the limited data set, since it was not feasible to spend more time performing tests on the detector. There are naturally

several areas in which the results of this thesis could be improved, given more detailed experimental data. These areas are discussed in turn below.

The elliptical nature of the detector beam could have consequences when calculating the coupling efficiency between the telescope and detector system. While photometric calculations performed with planetary sources have indicated that the coupling to the telescope is very good, detailed mapping of the beam using astronomical sources is warranted for future observing runs. In addition, more detailed beam mapping in the far-field could help determine the source of the vignetting effects described in Section 5.2.

A significantly better measure of the filter efficiencies could be obtained by measuring the detector signal with and without filters. This procedure would involve a significant amount of time, and it would certainly not be feasible to perform this kind of test during a normal observing run. Alternatively, by using a calibrated blackbody source, more accurate estimates of the power falling on the detector could be made, which would improve the uncertainty in the efficiency values calculated in Section 5.5 by fitting the optical and electrical responsivities.

A calibrated blackbody source would also be useful for determining the power loading during the V-I measurements. This would remove any uncertainty in the loading difference between the V-I curves, and would therefore allow more accurate theoretical fits. Blocking the apertures of the filter horns would also allow the background power in the bolometer housing to be calculated much more accurately, which would in turn improve the theoretical fit for the minimum loading condition, since the power loading would be known. Likewise, fixing any of the parameters in the V-I fitting process would improve the accuracy of the remaining fitted values. Two important values that could not be measured during this project were the bolometer housing temperatures, and the DC gain of the JFETs while the system was at operating temperature. While the fine sampling of the V-I data was necessary for accurate theoretical modelling, as well as for plotting the various bolometer equations as smooth functions of bias current, the jitter in the data proved to be a computational nuisance. For example, the data had to be smoothed (at the cost of precision) before any derivatives could be performed. As a result, complex functions such as those for thermal conductance or bolometer NEP produced jagged graphs when plotted as functions of bias current. This problem could be remedied during data collection by either setting each bias point manually and waiting for the bolometer voltage to settle (at the cost

of an enormous increase in the time required to test all detector, filter and source combinations), or by using a signal generator to ramp the bias voltage smoothly while recording the bolometer voltage (at the cost of modifying the bias voltage generator circuitry).

Despite the jitter in the V-I data, two interesting features remain unexplained from a theoretical point of view: The poor quality of the theoretical fits to the detector 2 V-I curves, relative to those for detector 1, and the behaviour of the thermal conductance curve at low temperature gradients. Since neither of these phenomena adversely affect the performance of the system, the extensive testing of the bolometer components that would be required to elucidate their physical significance is not likely to occur.

In terms of improving the system performance, there are few changes to the system that could be made. In practice, atmospheric conditions have been found to be the greatest limiting factor in astronomical spectroscopic measurements. Nonetheless, for atmospheric conditions that are particularly dry and stable, there are still gains to be made in detector sensitivity before the photon noise limit is reached for this system. The noise analysis of Section 5.6 has shown that the dominant noise sources are the Johnson and phonon noise intrinsic to the bolometer elements (see Figures 5.18 and 5.19). The most practical way to lower these noise contributions is to lower the bolometer operating temperature. This, however, would require a complete redesign of the system to incorporate a ^{3}He dilution refrigerator. A more likely scenario for the advancement of far-infrared Fourier transform spectroscopy would be the retrofitting of 100 mK systems such as SCUBA, with fully differential electronics so that their higher sensitivity could be realized spectroscopically.

[1] Strong, J., Neher, H., Whitford, A., Cartwright, C., and Hayward, R., *Procedures in Experimental Physics*, Prentice-Hall, N.J., 1963, p.530.

[2] Hect, E., *Optics* 2nd Ed, Addison-Wesley Press, Reading, Mass., 1990, p. 419.

[3] Jones, R. C., "The General Theory of Bolometer Performance", *J. Opt. Soc. Am.*, **43**, No. 1, 10, 1953.

[4] Holland, W. S., *Design and Development of Bolometric Detector Systems*, Ph. D. Thesis, QMW, London, UK, 1991.

[5] AD612 DAS module, Accu-Data, Suite C-178 297 Route 72 West, Manahawkin, New Jersey 08050-2890, USA.

[6] Mather, J. C., "Bolometer Noise: Nonequilibrium Theory", *Appl. Opt.*, **21**, No. 6, 1125-1129, 1981.

[7] Jones, R. C., "The General Theory of Bolometer Performance", *J. Opt. Soc. Am.*, **43**, No. 1, 1-14, 1953.

[8] HP 3563A Control Systems Analyzer, Hewlett-Packard Ltd., 6877 Goreway Drive, Mississauga, Ontario, L4V 1M8, Canada.

[9] Blackman, R. B., and Tukey, J. W., *The Measurement of Power Spectra from the Point of View of Communications Engineering*, Dover, New York, 1959.

[10] Griffin, M. J., and Holland, W. S., "The Influence of Background Power on the Performance of an Ideal Bolometer", *Int. J. of Infrared and Millimetre Waves*, **9**, No. 10, 861, 1988.

[11] Naylor, D. A., Schultz, A. A., and Clark, T. A., "Eliminating Channel Spectra in Fourier Transform Spectroscopy", *Appl. Opt.*, **27**, 2603, 1988.

[12] Holland, W. S., Robson, E. I., et al., "SCUBA: A Common-User Submillimetre Camera Operating on the James Clerk Maxwell Telescope", *Mon. Not. R. Astron. Soc.*, In Press.

[13] Duncan, W. D., Robson, E. I., et al., "A Millimetre/Submillimetre Common User Photometer for the James Clerk Maxwell Telescope", *Mon. Not. R. Astron. Soc.*, No. 25, 1989.

[14] Naylor, D. A., Clark, T. A., Davis, G. R., Duncan, W. D., and Tompkins, G. J., "Broad-band Spectroscopy With the James Clerk Maxwell Telescope Using a Polarizing Fourier Transform Spectrometer", *Mon. Not. R. Astron. Soc.*, **260**, 875-882, 1993.

[15] Treffers, R. R., "Signal-to-Noise Ratio in Fourier Transform Spectroscopy", *Appl. Opt.*, **16**, No. 12, 3103-3106, 1977.

Chapter 6

Software Code Appendix

6.1 Introduction

The majority of the work done in this project involved writing software for controlling the detector cryogenic system, controlling the data acquisition system for collecting the V-I data, and for analysing the spectroscopic, noise, and V-I data that was collected. All the control software was written in C++ using Borland C++ 4.5 [1], and the analysis routines were written using IDL 5.0 [2]. Since over 250 individual IDL routines were written for the various data extraction, manipulation, and plotting tasks required for this thesis, only a small set of critical routines are included in this appendix.

6.2 Automatic Cryogen Recycling Software

The C++ code given in this section was written to automate the recycling of the detector cryogens. A detailed description of the program sequence was presented in Chapter 4. The recycling program code (given below) uses standard C routines, as well as some custom-written C++ object oriented code (plots.h) to provide a convenient Graphical User Interface (GUI), and some useful array handling routines. The code to control the AD612 ADC module [3] was modified to allow the use of 8 digital I/O lines. The program uses a text configuration file (given immediately after the program code) to determine the temperature and time setpoints in the recycling process. This configuration file also contains the calibration data for the thermometers.

```
//*********************************************************************
//**         automatic cryogenic detector cycling program
//**                  written by Brad Gom 1997
//**
//**  to change any positions etc, change the #defines below and in plots.h
//**           AUTOCYCL.CFG contains all the user adjustable parameters
//*********************************************************************

//** modified may 19, 97 to reverse command polarity for stage diode (0=on)
//** removed heat switch activation
//** removed ge_diode current change. current now 100nA
//** added diode voltage offset for stage,4p,3p diodes.
//** heat timer start at beginning of heat cycle
//** final pushover of 3He after 3p cycle
   //** modified may 5, 98 to change bit assignments for new AD612 configuration,
   //** takes advantage of power up state of port.
   //**   Bit Function          Port on power up      status
   //**   0      heat sw pol.      0                  low voltage through heaters
   //**   1      Power kill        0                  Off (power on)
   //**   2      4 Pump            1                  Off
   //**   3      Stage diode       0                  On
   //**   4      3 Pump            1                  Off

   //**   modified may 19, 98 to kill power when stg Ge falls below setpoint. Maximum
   //**   time catch added. Data log stop added. Delayed cycle start added.

#include "c:\brad\source\includes\plots.h"    // contains gui routines for plotting data
#include "c:\brad\source\includes\AD612.h"    // contains routines to read analog and
                                             // R/W digital pins of the acqudat

#define mainplotx  2                 // coordinates of the main data plot box
#define mainploty  20
#define mainplotw  636
#define mainploth  350

#define valueboxx  2                 // coordinates of the main data plot box
#define valueboxy  380
#define valueboxw  170
#define valueboxh  90

#define optionboxx 64
#define optionboxy 150
#define optionboxw 510
#define optionboxh 120

#define delimiter "      "      // delimiter to seperate the columns in the saved files

            // bits used to control the electronics
#define heat_sw_polarity 0      // used to set the voltage through the heaters
#define power_kill 1            // final power off

#define _4p_heater 2
#define stg_diode 3
#define _3p_heater 4

#define OPEN 1
#define CLOSED 2
#define DONE 3

//*************************  FUNCTION PROTOTYPES  *************************

void drawmenubar();
void optioninput();
void get_menu_choice();
int Save(int);              // saves one set of data points. returns 0 on file failure
int do_scan();               // performs one single scan, returns 1 on abort or stop
int wait_to_scan();          // delays and checks the abort button between readings
void load_config();
void save_config();
void control_loop();
float volt_to_temp(int, double);
void display_status();
```

```
// ***************************************************************************
//          global objects
//***************************************************************************

Screen screen;

AD612 ADC;            // the acqudata module
Plotwindow mainplot;     // set up a 'plot window' using gui routines for easy data plots
menubar mainmenu;        // set up a gui menubar
ofstream datafile("TEMP.DAT");   // this is the temporary name for the data file. it is
renamed when the program ends

matrix scan_data(2403,5);
// 120 minutes of 3 second samples. the points member holds the total number of points
// the data starts at row 0, [][x] is channel x  (0 to 3 )  [][4] is the time index
matrix dt500(96,2);

//*************************  GLOBAL VARIABLES  *************************
char ch;                        // generic char for keyboard input
int choice;                        // buffer for menu choice
int quit;                  // causes main loop to stop

char far *tempstr;              // generic string for output text

struct textsettingstype prev_settings;     // stores previous text settings
char comment[50];               // comment in file header
char fileprefix[8];            // filename prefix _______.DAT
char filename[12];             // full filename
int check_abort;               // holds value returned from do_scan() to check for abort
int scan_in_progress=0;        // 1 when a scan loop is in progress
int cycle_started=0;
      // used to determine if a cycle can be resumed or if a new scan must be performed
double stepdelay=2;            // # of seconds to wait between readings
float cycle_delay=0;
char* xunits="min.";           // text for the cursor position display
char* yunits="K.";
int current_window=1;
int high_time=20;              // the # of minutes per window
float low_temp=0;              // sets low end of temperature range
float high_temp=300;           // sets high end of temperature range
int chancol[7]={13,GREEN,YELLOW,WHITE,0,0,0};  //holds colors for the different channels
int comment_written=0;
time_t filetime;               // holds the start and finish times for the data file
char * channel_labels[]={"4He pump ","3He pump ","STG Diode","STG Ge    "};

float set_temp[13];                        // the temperature setpoints
float delay_4p,delay_3p,delay_push,total_time; // minutes that the heaters to stay on
unsigned int heat_sw_status;               // the position of the heat switch
time_t heater_on_time,begin_time;          // time the heaters were turned on
unsigned int enable4p=1;       // enables the execution of the 4p cycle procedure
unsigned int enable3p=0;       // enables the execution of the 3p cycle procedure
unsigned int final_push=0;          // enables final pushover
unsigned int heat_cycle=0;          // 1 enables the timed heating of the 4p and 3p
unsigned int enable_kill=0;         // enables power kill after final cooldaown
unsigned int time_set=0;
unsigned int stop_log=0;           // stops the program when power is killed
float current=0.1;                     // Ge current default to 100 nA
float diode_offset=20;
float I_3p, I_4p, I_stg, I_Ge_low, I_Ge_high, R_Ge;   // current corrections
char *control_status="Pre-Cooling";    // text for the status of the control loop
unsigned int manual_cycle=0;           // sets automated or manual cycling
unsigned int status_4p,status_3p,stg_diode_status;    // for the status display
float stg=0;      // initital readings of the stage diode and stage Ge
float Ge=0;

unsigned int _4p_chan=0;          // analog input channels
unsigned int _3p_chan=1;
unsigned int stg_diode_chan=2;
unsigned int stg_Ge_chan=3;

//***************************************************************************
//                          MAIN
//***************************************************************************
```

```
void main()
{
   sprintf(fileprefix,"TEMPDATA");     // default file prefix
//*************************************************************************
//               Initialize graphics driver
//*************************************************************************
 clrscr();

 int graphdrv = VGA;       // vga driver
 int graphmode = VGAHI;    // 640x480 mode  16 color
 int ErrorCode = grOk;

   if (registerbgidriver(EGAVGA_driver) < 0) exit(1);
   initgraph(&graphdrv, &graphmode, "");
   ErrorCode = graphresult();       // Read result of initialization
   if( ErrorCode != grOk ){     // Error occured during init
      printf(" Graphics System Error: %s\n", grapherrormsg( ErrorCode ) );
      delay(1000);
      exit( 1 );
      }
   setbkcolor(BKG);      // sets background
   cleardevice();       // fills screen background

   load_config();  // call load config before mainplot.init and mainplot.get_options
   if(!the_mouse.init()) {
      puts("Unable to detect mouse driver. Program requires mouse.");
      closegraph();
      exit(1);
      }
//*************************************************************************

   the_mouse.arm();          // enable the mouse
   Gtext finding;            // find Acqudat
   finding.init(200,200,"Finding AD612 Device...",WHITE,BLACK,0);
   finding.outline(WHITE,5);
   finding.show();
   current=0.1;          // Ge current is 10 uA
   int status=ADC.find(245);// find the AD612 and initialize all the dio pins neutral.
                            // stage on, 3p off, 4p off, polarity=full voltage
   if(status){
      Gtext found;
      sprintf(tempstr,"AD612 FOUND AT %x",status);
      found.init(220,230,tempstr,RED,BLACK,0,1);
      found.show();
      delay(1000);
      found.hide();
      }
   else {
      messagebox notfound;
      if(notfound.show("AD612 NOT FOUND! Continue?",MB_YESNO)==ID_NO) exit(0);
      }
   finding.hide();

   ADC.SetRange(4.096);    // make the return value range from 0-4.096

   //**********   initialize the electronics to default state
   ADC.setDIO(9,245);
    // set all pins =>  stage on, 3p off, 4p off, polarity=full voltage, power on
   delay(100);             // delay to avoid relay noise
   current=0.1;
   heat_sw_status=OPEN;
   status_4p=0;                 // 4 pump off
   status_3p=0;                 // 3 pump off
   stg_diode_status=1;          // stage diode on

   //**********   get initial temperature to decide status of heat switch

   for(int x=0;x<100;x++) {     // average 100 samples
      stg+=volt_to_temp(stg_diode_chan, ADC.ReadChan(stg_diode_chan));
   // read in stg_diode temperature
      Ge+=volt_to_temp(stg_Ge_chan, ADC.ReadChan(stg_Ge_chan));
      // read in Ge diode temperature
      }
   stg/=100;
```

```
Ge/=100;

if(stg < 0.36) {
    messagebox cold;
    if(cold.show("Stage Cold! O.K. to Re-Cycle?",MB_YESNO)==ID_NO) exit(0);
    }

mainplot.init(mainplotx,mainploty,mainplotw,mainploth,OUT,THICK,0,high_time,
              low_temp,high_temp,chancol,"Minutes","Kelvin",BKG,0);
mainplot.init_vb(valueboxx,valueboxy,4,channel_labels,0,BLACK);
mainplot.show_vb();

drawmenubar();          // draw interface for main prog
optioninput();          // get scan options
mainplot.show();        // draw plot window
mainplot.drawaxis();

    for(int chan=0; chan<4; chan++){          // show starting temperatures
        scan_data.elem(0,chan)=volt_to_temp(chan, ADC.ReadChan(chan));
        mainplot.show_value(chan,scan_data.elem(0,chan));
        }

    the_mouse.hide();
    mainplot.clear();     // redraw plot window
    the_mouse.show();

    display_status();

    last_point=0;
    scan_in_progress=0;

        //****************************************
        //             Main Loop
        //****************************************
while(!quit){
        if(kbhit()) {
            if((ch=getch())==27){
                quit=2;
                break;  // this loop determines what happens while no scan in progress
                }
            flushkeys();
            continue;
            }

        if (mainplot.hit()) {
            the_mouse.changeto(CROSSHAIR);
            if (the_mouse.RBP()){
                if (mainplot.hit()) mainplot.show_cursor_pos(xunits,yunits);
                }
            }
        else {
            the_mouse.changeto(ARROW);
            }

        if(mainmenu.triggered()) {
            get_menu_choice();
            }
        }     // end main loop

    save_config();           // save the current configuration

    time(&filetime);         // write the end time on the file.
    datafile<<"Program Finished on "<<ctime(&filetime)<<endl;
    sprintf(filename,"%s.DAT",fileprefix);
    closegraph();

     /* Rename the file */
    datafile.close();

    if(rename("TEMP.DAT",filename) != 0) {
        perror("Error renaming data file ");
        delay(2000);
        }
    if(quit==1) printf("\n\n\nDetector Controller Shut Down Successfully\n");
```

```
    if(quit==2) {
           printf("\n\n\nUnexpected Exit.\n");
           printf("Controller may not have shut down properly.\n");
           }
    if(quit==3) printf("\n\n\nCycle ended normally.\n");
    exit(0);
}


//*****************************************************************************
void get_menu_choice()
{
char c;
time_t delay_started;
    switch(mainmenu.trackbar()) {
    case 1:
    if(!scan_in_progress) {      // get new options
    optioninput();
    the_mouse.hide();
    mainplot.reset_axis(0,high_time,low_temp,high_temp);
    mainplot.clear();        // redraw plot windows
    the_mouse.show();
    }
    break;
case 2:
    if(!scan_in_progress) {     // reset options
    sprintf(fileprefix,"TEMPDATA");
    stepdelay=1;
    sprintf(comment,"");
    optioninput();
    the_mouse.hide();
    mainplot.reset_axis(0,high_time,low_temp,high_temp);
    mainplot.clear();            // redraw plot windows
    the_mouse.show();
    }
    break;
case 3:
    if(!scan_in_progress) {      // starts automatic sequence
    manual_cycle=0;
    {
    messagebox powerkill;
    powerkill.show("Auto Power-Off enabled. Turn OFF main power.",MB_OK);
    }
    do_scan();
    }
    break;
case 4:
    if(!scan_in_progress) {     // starts manual sequence
    manual_cycle=1;
    do_scan();
    }
    break;
case 45:
    if(!scan_in_progress) {      // starts delayed automatic sequence
    cycle_started=0;      //makes sure the cycle starts no matter what after the delay
    manual_cycle=0;
    {
    messagebox powerkill;
    powerkill.show("Auto Power-Off enabled. Turn OFF main power.",MB_OK);
    }
    ADC.setDIO(stg_diode,1); // turn off stage diode till cycle starts
    stg_diode_status=0;
    display_status();
    delay_started=time(NULL);
    do{                          // wait to start delayed cycle
if(kbhit()) {
    while(kbhit()) c=getch();
    if(c==27) {       // quit when ESC hit
        messagebox confirm;
        if(confirm.show("Abort delay and Exit?",MB_YESNO)==ID_YES) quit=1;
        }
    }
mainplot.status_line("Delaying Cycle start...");
delay(1000);
mainplot.status_line("Hit ESC to abort...");
```

```
        delay(1000);
        }
    while( difftime(time(NULL),delay_started) < cycle_delay*double(3600)  && quit==0);

    ADC.setDIO(stg_diode,0); // turn ON stage diode
    stg_diode_status=1;
    display_status();
    do_scan();
    }
    break;
case 5:
    the_mouse.hide();
    mainplot.get_options();     // get axis scaling options
    mainplot.drawaxis();
    the_mouse.show();
    break;
case 6:
    mainplot.clear();
    break;
case 7:                              // set max y to 300 K
    high_temp=300;
    mainplot.reset_axis((current_window-1)*high_time,current_window*high_time,
          low_temp,high_temp);
    mainplot.set_options(mainplot.ticks[0].spacing,mainplot.ticks[1].spacing,100,
          3,1,0,1,0);
    mainplot.clear();
    mainplot.load_data(scan_data,0,last_point);
    mainplot.drawplot(chancol);
    break;
case 8:                              // set max y to 100 K
    high_temp=100;
    mainplot.reset_axis((current_window-1)*high_time,current_window*high_time,
          low_temp,high_temp);
    mainplot.set_options(mainplot.ticks[0].spacing,mainplot.ticks[1].spacing,
          25,4,1,0,1,0);
    mainplot.clear();
    mainplot.load_data(scan_data,0,last_point);
    mainplot.drawplot(chancol);
    break;
case 9:                              // set max y to 60 K
    high_temp=60;
    mainplot.reset_axis((current_window-1)*high_time,current_window*high_time,
          low_temp,high_temp);
    mainplot.set_options(mainplot.ticks[0].spacing,mainplot.ticks[1].spacing,10,
          4,1,0,1,0);
    mainplot.clear();
    mainplot.load_data(scan_data,0,last_point);
    mainplot.drawplot(chancol);
    break;
case 10:                             // set max y to 10 K
    high_temp=10;
    mainplot.reset_axis((current_window-1)*high_time,current_window*high_time,
          low_temp,high_temp);
    mainplot.set_options(mainplot.ticks[0].spacing,mainplot.ticks[1].spacing,5,
          4,1,0,1,0);
    mainplot.clear();
    mainplot.load_data(scan_data,0,last_point);
    mainplot.drawplot(chancol);
    break;
case 11:                          // set max y to 5 K
    high_temp=5;
    mainplot.reset_axis((current_window-1)*high_time,current_window*high_time,
          low_temp,high_temp);
    mainplot.set_options(mainplot.ticks[0].spacing,mainplot.ticks[1].spacing,
          1,0,1,0,1,0);
    mainplot.clear();
    mainplot.load_data(scan_data,0,last_point);
    mainplot.drawplot(chancol);
    break;
case 12:              // turn 4P ON
    ADC.setDIO(_4p_heater,0);
    status_4p=1;                    // 4 pump on
    display_status();
    break;
case 13:              // turn 4P Off
```

```
    ADC.setDIO(_4p_heater,1);
    status_4p=0;                    // 4 pump off
    display_status();
    break;
case 14:                // turn 3P ON
    ADC.setDIO(_3p_heater,0);
    status_3p=1;                    // 3 pump on
    display_status();
    break;
case 15:                // turn 3P Off
    ADC.setDIO(_3p_heater,1);
    status_3p=0;                    // 3 pump off
    display_status();
    break;
case 16:                // turn stage ON
    ADC.setDIO(stg_diode,0);
    stg_diode_status=1;             // stage on
    display_status();
    break;
case 17:                // turn stage Off
    ADC.setDIO(stg_diode,1);
    stg_diode_status=0;             // stage off
    display_status();
    break;
case 18:                // turn main power Off
    ADC.setDIO(power_kill,1);
    control_status="Done. Power Killed.";
    display_status();
    break;
case 99:                // quit
    if(scan_in_progress) {
        messagebox confirm;
        if(confirm.show("SAVE DATA AND EXIT?",MB_YESNO)==ID_YES) quit=1;
        else quit=0;
        }
    else quit=1;
    break;

default:   outtextxy(100,100,"menu bug"); delay(2000);
}   // end menu choice

//*****************************************************************************

void drawmenubar()
{
    the_mouse.hide();
    pulldown file,options,start,plot,control;  // don't confuse the options pulldown class
                                               // with the options member.
    file.init(BLACK,WHITE,YELLOW,BLUE,0,0);
    file.set_option(0,"&Quit",99);
    file.options[0].self_color(BLACK,WHITE,YELLOW,RED);

    options.init(BLACK,WHITE,YELLOW,BLUE,0,0);
    options.set_option(0,"&New Setup",1);
    options.set_option(1,"&Default Setup",2);

    start.init(BLACK,WHITE,YELLOW,BLUE,0,0);
    start.set_option(0,"&Start Auto Cycle",3);
    start.set_option(1,"Start &Manual Cycle",4);
    start.set_option(2,"Start &Delay Cycle",45);

    plot.init(BLACK,WHITE,YELLOW,BLUE,0,0);
    plot.set_option(0,"&Axis Options",5);
    plot.set_option(1,"&Clear Window",6);
    plot.set_option(2,"-",0);
    plot.set_option(3,"Max temp= &300 K",7);
    plot.set_option(4,"Max temp= &100 K",8);
    plot.set_option(5,"Max temp= &60 K",9);
    plot.set_option(6,"Max temp= 1&0 K",10);
    plot.set_option(7,"Max temp= &5 K",11);

    control.init(BLACK,WHITE,YELLOW,BLUE,0,0);
    control.set_option(0,"&4P on",12);
    control.set_option(1,"&4P off",13);
```

```
    control.set_option(2,"&3P on",14);
    control.set_option(3,"&3P off",15);
    control.set_option(4,"&stage on",16);
    control.set_option(5,"&stage off",17);
    control.set_option(6,"&Kill Power",18);

    mainmenu.init(BLACK,WHITE,YELLOW,BLUE);
    mainmenu.set_title(0,"&File",&file);
    mainmenu.set_title(1,"&Options",&options);
    mainmenu.set_title(2,"&Plot",&plot);
    mainmenu.set_title(3,"&Start",&start);
    mainmenu.set_title(4,"&Control",&control);

    mainmenu.display();
    the_mouse.show();
}

//*****************************************************************************

void optioninput()      // input box for scan options
{
Bevel optionbox;              // the optionbox frame
                              // text inputs
Gstring gs_comment,gs_filename;
                              // text prompts
    optionbox.init(optionboxx,optionboxy,optionboxw,optionboxh,THICK,1);
    optionbox.show();

    setcolor(BLACK);
    settextstyle(SMALL_FONT, HORIZ_DIR, 4);
    settextjustify(LEFT_TEXT,BOTTOM_TEXT);

    gs_comment.init(optionboxx+92,optionboxy+60,50,0,0);
    gs_comment.preset(comment);
    gs_filename.init(optionboxx+92,optionboxy+30,8,1,0);

    gs_comment.show();
    gs_filename.show();
    outtextxy(optionboxx+10,optionboxy+60,"Comments:");
    outtextxy(optionboxx+10,optionboxy+30,"Filename:");
    outtextxy(optionboxx+165,optionboxy+30,".DAT");

    OK.init(optionboxx+optionboxw-40,optionboxy+optionboxh-40,"OK",TEXT,0);
         // OK to exit button
    OK.show();

    int goodname=0;
    int okhit=0;

    gs_filename.reset();
    gs_filename.get_input();
    sprintf(fileprefix,"%s",gs_filename.getstring());
    sprintf(filename,"%s.DAT",fileprefix);
    if(access(filename,0)==0) {
        messagebox confirm;
        if(confirm.show("FILE ALREADY EXISTS! REPLACE?",MB_YESNO)==ID_YES){
            remove(filename);
            goodname=1;
            }
        else goodname=0;
        }
    else goodname=1;

    flushkeys();
while(!goodname || !okhit) {
    if(the_mouse.LBP()) {
        if(gs_comment.clicked()) {
            gs_comment.get_input();
            sprintf(comment,"%s",gs_comment.getstring());
            }

        if(gs_filename.clicked()) {
                gs_filename.reset();
                gs_filename.get_input();
                the_mouse.hide();
```

```
            sprintf(fileprefix,"%s",gs_filename.getstring());
            sprintf(filename,"%s.DAT",fileprefix);
            the_mouse.show();
            if(access(filename,0)==0) {
                messagebox confirm;
                if(confirm.show("FILE ALREADY EXISTS! REPLACE?",MB_YESNO)==ID_YES){
                    remove(filename);
                    goodname=1;
                    }
                else goodname=0;
                }
            else goodname=1;
        }
    if(OK.hit()) {          // quit if OK is pressed
        OK.press();
        while(the_mouse.LBP() && OK.hit());
        OK.show();
        if(OK.hit()) {
            sprintf(filename,"%s.DAT",fileprefix);
            if(access(filename,0)==0) {
                messagebox confirm;
                if(confirm.show("FILE ALREADY EXISTS! REPLACE?",MB_YESNO)==ID_YES){
                    remove(filename);
                    goodname=1;
                    }
                else {
                    goodname=0;
                    okhit=0;
                    }
                }
            else goodname=1;
            okhit=1;
            }
        }// end if the_mouse.LBP
    if(kbhit()) {
        if((ch=getch())==27)
        break;
        }
    }

choice=0;       // reset the menu choice buffer
optionbox.hide();

    // free up memory used by buffer containing
    // underlying graphics

optionbox.elim();
}
//*****************************************************************************

float volt_to_temp(int chan, double volt)
{
    switch( chan )  // performs a binary search on the appropriate voltage-temp data table
    {
        case 0:     // ifn146 table        for 4p
            return ifn146.binary_search(1,0,(volt-diode_offset*0.001)*(10/I_4p));
        case 1:     // ifn146 table        for 3p
            return ifn146.binary_search(1,0,(volt-diode_offset*0.001)*(10/I_3p));
        case 2:      // dt500 table         for stg diode
            return dt500.binary_search(1,0,(volt-diode_offset*0.001)*(10/I_stg));
        case 3:      // gr100 table         Ge diode
            return gr100.binary_search(1,0, (volt/(204.8e-6))-R_Ge );
    }
return 0;
}

//*****************************************************************************

int do_scan()         // sample until 4.5 seconds, then average and save data.
{
int counter,last_saved,avg_count,selected,channel,timebase;

int abort_hit;        // holds the return value for abort or stop etc
int return_value=0;
```

```
float avg_data[5]={0,0,0,0,0};  // temporary buffer to hold un averaged data.
struct dostime_t s,f;
unsigned long h_res_time;           // current time in hundredths of seconds
int c;
time_t time_started;
Gtext gt_time,gt_started;

    scan_in_progress=1;
    timebase=0;
    selected=0;
    counter=0;                // counts from 0 to the number of samples in a window
    last_saved=0;
    current_window=1;
    avg_count=0;

    setcolor(LIGHTBLUE);
    settextjustify(LEFT_TEXT,TOP_TEXT);
    outtextxy(mainplotx,mainploty+mainploth+8,"Started:");
    time(&time_started);
    gt_started.init(mainplotx+70,mainploty+mainploth+8,ctime(&time_started),9,0,0);
    gt_started.show();

    if(cycle_started) {
       messagebox resume;
       if(resume.show("Resume last cycle where it left off?",MB_YESNO)==ID_NO) {
          for(int t=0;t<100;t++) {          // average 100 samples
             stg+=volt_to_temp(stg_diode_chan, ADC.ReadChan(stg_diode_chan));
    // read in stg_diode temperature
             Ge+=volt_to_temp(stg_Ge_chan, ADC.ReadChan(stg_Ge_chan));
   // read in Ge diode temperature
             }
          stg/=100;
          Ge/=100;

          if(Ge < 0.36) {
             messagebox cold;
             if(cold.show("Stage Cold! O.K. to Re-Cycle?",MB_YESNO)==ID_NO) selected=1;
             }

          if (!manual_cycle) {
             enable4p=1;
     // enables the execution of the 4p cycle procedure  ( initially enabled)
             enable3p=0;
     // enables the execution of the 3p cycle procedure  ( initially disabled)
             heat_cycle=0;        // 1 enables the timed heating of the 4p and 3p
             time_set=0;
             control_status="Pre-Cooling";   // text for the status of the control loop

             ADC.setDIO(_4p_heater,1);        // turn OFF heater
             status_4p=0;                  // 4 pump off
             ADC.setDIO(_3p_heater,1);        // turn OFF heater
             status_3p=0;                  // 3 pump off
             }
           else control_status="Manual Cycle";
          }
       }

    cycle_started=1;
    for(int x=0;x<5;x++) scan_data.elem(0,x)=0;
    flushkeys();

    while(!selected && !quit && !stop_log) {
       mainplot.reset_axis((current_window-1)*high_time,current_window*high_time,
             low_temp,high_temp);
       mainplot.clear();
       mainplot.status_line("Scanning...");
    if(kbhit()) {
       while(kbhit()) c=getch();
       if(c==27) {                    // quit when ESC hit
          messagebox confirm;
          if(confirm.show("STOP AND SAVE DATA?",MB_YESNO)==ID_YES) selected=1;
          }
       }
```

```
if(mainmenu.triggered()) {
    get_menu_choice();
    }

while(counter<=high_time*60/stepdelay && !selected && !quit && !stop_log){
// collect data until window is full
    if(kbhit()) {
        while(kbhit()) c=getch();
        if(c==27) {                    // quit when ESC hit
            messagebox confirm;
            if(confirm.show("STOP AND SAVE DATA?",MB_YESNO)==ID_YES) selected=1;
            }
        }
    if(mainmenu.triggered()) {
        get_menu_choice();
        }

                for(channel=0; channel<4; channel++){          // reset average buffer
                    avg_data[channel]=0;
                    }
                avg_count=0;
                _dos_gettime(&s);                  // high res timer
                h_res_time=(s.hour*360000)+(s.minute*6000)+(s.second*100)+(s.hsecond);

                mainplot.status_line("Averaging samples...");
                do{        // sample until out of time
                           // check for abort
                    if(kbhit()) {
                        while(kbhit()) c=getch();
                        if(c==27) {           // quit when ESC hit
                            messagebox confirm;
                            if(confirm.show("STOP AND SAVE DATA?",MB_YESNO)==ID_YES) selected=1;
                            }
                        }
                    if(mainmenu.triggered()) {
                        get_menu_choice();
                        }

                    for(channel=0; channel<4; channel++){     // get data points for average
                                                              // until time expires
                        avg_data[channel]+=volt_to_temp(channel,ADC.ReadChan(channel));
                        }
                    avg_count++;
                    _dos_gettime(&f);
                    }
                    while(((f.hour*360000) + (f.minute*6000) + (f.second*100) + f.hsecond) -
                    h_res_time < (stepdelay-.5)*100 && !selected && !quit && !stop_log);

                mainplot.status_line("Done sampling, waiting for interval...");
                scan_data.elem(counter,4)=(float)timebase/60; // store time index in MINUTES
                timebase+=stepdelay;

                for(channel=0; channel<4; channel++){
                     // store averaged points to array and draw lines
                    scan_data.elem(counter,channel)=avg_data[channel]/avg_count;
                    if(counter>0)
mainplot.plotline(scan_data.elem(counter-1,4),scan_data.elem(counter-1,channel),
                                scan_data.elem(counter,4),scan_data.elem(counter,channel),
chancol[channel]);
                    mainplot.show_value(channel,scan_data.elem(counter,channel));
                    }
                if(scan_data.elem(counter,stg_Ge_chan) >= gr100.elem(0,0) ||
                    scan_data.elem(counter,stg_Ge_chan) <= gr100.elem(10,0)) {
                mainplot.show_value(stg_Ge_chan,scan_data.elem(counter,stg_Ge_chan),"K",1);
                }
if(scan_data.elem(counter,stg_diode_chan) >= dt500.elem(0,0) ||
        scan_data.elem(counter,stg_diode_chan) <= dt500.elem(113,0)) {
    mainplot.show_value(stg_diode_chan,scan_data.elem(counter,stg_diode_chan),
        "K",1);
    }
last_point=counter;

if (!manual_cycle) control_loop(); // do main control sequence for autocycle

if(counter==0) Save(counter);
```

```
if(counter>0) {
    for(channel=0; channel<4; channel++){  // save if changed by more than 1%
        if(fabs((double)(scan_data.elem(counter,channel)-
                scan_data.elem(last_saved,channel))/scan_data.elem(last_saved,
                channel))  > 0.01) {
            last_saved=counter;
            mainplot.status_line(">1% change, saving data...");
            Save(counter);
            break;
            }
        }
    }

do {              // wait till next point
    _dos_gettime(&f);
    }
                while(((f.hour*360000) + (f.minute*6000) + (f.second*100) + f.hsecond) -
                        h_res_time < stepdelay*100 && !selected && !quit && !stop_log) ;
            counter++;
            }
   // after the 1st window, use the last point in the window as the first point
   // in the next window
        for(channel=0; channel<4; channel++){
            scan_data.elem(0,channel)=scan_data.elem(counter-1,channel);
            }
        if(!selected && !quit) {
            counter=1;
            current_window++;
            }
        }

        mainplot.status_line("Done.");
        time(&filetime);              // write the end time on the file.
        datafile<<"Cycle Finished on "<<ctime(&filetime)<<endl;
        scan_in_progress=0;

return(return_value);  //   return 0 if no abort or error
}

//*************************************************************************

int wait_to_scan()        // returns 1 on abort, 2 on stop, 0 if ok
{
struct dostime_t s,f;
unsigned long h_res_time;        // current time in hundredths of seconds
int return_value=0;

  _dos_gettime(&s);
    h_res_time=(s.hour*360000)+(s.minute*6000)+(s.second*100)+(s.hsecond);

        do{      // 0.1 second resolution delays if units are 1/10 seconds
            if(the_mouse.LBP()){    // check for abort
                }
        // check for zoom etc here
            _dos_gettime(&f);
            }
        while(((f.hour*360000) + (f.minute*6000) + (f.second*100) + f.hsecond) -
                h_res_time < stepdelay*100);

return(return_value);
}

//*************************************************************************8
void load_config()
{
ifstream infile("AUTOCYCLE.CFG");
char *tempstring;
char c;
float x_maj_ticks=mainplot.ticks[0].spacing;
float y_maj_ticks=mainplot.ticks[2].spacing;
int x_min_ticks=mainplot.ticks[1].spacing;
int y_min_ticks=mainplot.ticks[3].spacing;
int majxgrid,minxgrid,majygrid,minygrid;
int count;
```

```
if (infile){
    infile.ignore(1000,42);
// ignore up to 1000 characters until asterix (42) is present
    infile>>cycle_delay;
    infile.ignore(1000,42);
    infile>>stepdelay;
    infile.ignore(1000,42);
    infile>>high_time;
    infile.ignore(1000,42);
    infile>>high_temp;
    infile.ignore(1000,42);
    infile >> x_maj_ticks >> x_min_ticks >> y_maj_ticks >> y_min_ticks;
    infile.ignore(1000,42);
    infile >> majxgrid >> minxgrid >> majygrid >> minygrid;
    mainplot.set_options(x_maj_ticks, x_min_ticks, y_maj_ticks, y_min_ticks,
            majxgrid, minxgrid, majygrid, minygrid);
        infile.ignore(1000,42);
        infile >> chancol[0] >> chancol[1] >> chancol[2] >> chancol[3];
        infile.ignore(1000,42);
        infile >> set_temp[1] >> set_temp[2] >> set_temp[3] >> set_temp[4] >>
               set_temp[5] >> set_temp[6] >> set_temp[7] >> set_temp[8] >>
               set_temp[9] >> set_temp[10];
        infile.ignore(1000,42);
        infile >> delay_4p >> delay_3p >> delay_push >> total_time;
        infile.ignore(1000,42);
        infile >> I_3p >> I_4p >> I_stg >> I_Ge_low >> I_Ge_high >> R_Ge>>diode_offset;
        infile.ignore(1000,42);
        for(count=0;count<7;count++){
            infile >> gr100.elem(count,0) >> gr100.elem(count,1);
            }
        infile.ignore(1000,42);
        for(count=0;count<74;count++){
            infile >> ifn146.elem(count,0) >> ifn146.elem(count,1);
            }
        infile.ignore(1000,42);
        for(count=0;count<96;count++){
            infile >> dt500.elem(count,0) >> dt500.elem(count,1);
            }

        scan_data.resize(high_time*70/stepdelay,5);
            // make sure there is enough room in the array

        }
    else {
        outtextxy(100,100,"AUTOCYCLE.CFG not found!!");
        delay(2000);
        }

}

//*****************************************************************************
void save_config()
{
ifstream infile("AUTOCYCLE.CFG");
ofstream outfile("TEMP.CFG");
char *tempstring;
char c;
float x_maj_ticks=mainplot.ticks[0].spacing;
float y_maj_ticks=mainplot.ticks[2].spacing;
int x_min_ticks=mainplot.ticks[1].spacing;
int y_min_ticks=mainplot.ticks[3].spacing;
int count;

    if (outfile){
infile.seekg(0);
do{
    infile.get(c);
    outfile<<c;
    }
    while(c!=42);
infile.getline(tempstring,100);
infile.getline(tempstring,100);
outfile<<endl;
outfile<<cycle_delay<<endl;
do{
```

```
    infile.get(c);
    outfile<<c;
    }
    while(c!=42);
infile.getline(tempstring,100);
infile.getline(tempstring,100);
outfile<<endl;
outfile<<stepdelay<<endl;
do{
    infile.get(c);
    outfile<<c;
    }
    while(c!=42);
infile.getline(tempstring,100);
infile.getline(tempstring,100);
outfile<<endl;
outfile<<high_time<<endl;
do{
    infile.get(c);
    outfile<<c;
    }
    while(c!=42);
infile.getline(tempstring,100);
infile.getline(tempstring,100);
outfile<<endl;
outfile<<high_temp<<endl;
do{
    infile.get(c);
    outfile<<c;
    }
    while(c!=42);
infile.getline(tempstring,100);
infile.getline(tempstring,100);
outfile<<endl;
outfile<<x_maj_ticks<<"\t"<<x_min_ticks<<"\t"<<y_maj_ticks<<"\t"<<
      y_min_ticks<<endl;
do{
    infile.get(c);
    outfile<<c;
    }
    while(c!=42);
infile.getline(tempstring,100);
infile.getline(tempstring,100);
outfile<<endl;
outfile<<mainplot.ticks[0].grid_enabled<<"\t"<<mainplot.ticks[1].grid_enabled<<
      "\t"<<mainplot.ticks[2].grid_enabled<<"\t"<<
      mainplot.ticks[3].grid_enabled<<endl;
do{
    infile.get(c);
    outfile<<c;
    }
    while(c!=42);
infile.getline(tempstring,100);
infile.getline(tempstring,100);
outfile<<endl;
outfile<< chancol[0] <<"\t"<< chancol[1] <<"\t"<< chancol[2] <<"\t"<<
       chancol[3]<<endl;
do{
    infile.get(c);
    outfile<<c;
    }
    while(c!=42);
infile.getline(tempstring,100);
infile.getline(tempstring,100);
outfile<<endl;
outfile << set_temp[1] <<"\t"<< set_temp[2] <<"\t"<< set_temp[3] <<
      "\t"<< set_temp[4] <<"\t"<< set_temp[5] <<"\t"<< set_temp[6] <<
      "\t"<< set_temp[7] <<"\t"<< set_temp[8]<<"\t"<< set_temp[9] <<
      "\t"<< set_temp[10] << endl;
do{
    infile.get(c);
    outfile<<c;
    }
    while(c!=42);
infile.getline(tempstring,100);
```

```
infile.getline(tempstring,100);
outfile<<endl;
outfile << delay_4p <<"\t"<< delay_3p<<"\t"<< delay_push <<"\t"<<
      total_time << endl;
do{
   infile.get(c);
   outfile<<c;
   }
   while(c!=42);
infile.getline(tempstring,100);
infile.getline(tempstring,100);
outfile<<endl;
outfile << I_3p <<"\t" << I_4p <<"\t" << I_stg <<"\t" << I_Ge_low <<"\t"
      << I_Ge_high <<"\t" << R_Ge <<"\t" << diode_offset <<endl;
do{
   infile.get(c);
   outfile<<c;
   }
   while(c!=42);
infile.getline(tempstring,100);
outfile<<endl;
for(count=0;count<7;count++){
   infile.getline(tempstring,100,'\n');
   outfile << gr100.elem(count,0) <<"\t"<< gr100.elem(count,1) << endl;
   }
do{
   infile.get(c);
   outfile<<c;
   }
   while(c!=42);
infile.getline(tempstring,100);
outfile<<endl;
for(count=0;count<74;count++){
   infile.getline(tempstring,100,'\n');
   outfile << ifn146.elem(count,0) <<"\t"<< ifn146.elem(count,1) << endl;
   }
do{
   infile.get(c);
   outfile<<c;
   }
   while(c!=42);
infile.getline(tempstring,100);
outfile<<endl;
for(count=0;count<96;count++){
   infile.getline(tempstring,100);
   outfile << dt500.elem(count,0) <<"\t"<< dt500.elem(count,1) << endl;
   }
}
infile.close();
outfile.close();
remove("AUTOCYCLE.CFG");
rename("TEMP.CFG","AUTOCYCLE.CFG");
//  remove("TEMP.CFG");
}

//*************************************************************************

int Save(int rowindex)
  // returns 0 on file error -> although no error checking is implemented
{
   if(datafile){
      if(!comment_written){            // write the header on the first call to Save()
         datafile<<comment<<endl;
         time(&filetime);
         datafile<<"Started on "<<ctime(&filetime)<<endl;
         datafile<<"seconds"<<delimiter<<channel_labels[0]<<delimiter<<
               channel_labels[1]<<delimiter<<channel_labels[2]<<delimiter<<
               channel_labels[3]<<endl;
         comment_written=1;
         }
     // store the time index in SECONDS, then the channel readings.
   datafile<<scan_data.elem(rowindex,scan_data.x_col)*60<<delimiter<<
         scan_data.elem(rowindex,0)<<delimiter<<scan_data.elem(rowindex,1)<<
         delimiter<<scan_data.elem(rowindex,2)<<delimiter<<
         scan_data.elem(rowindex,3)<<endl;
```

```
        }
    else return(0);

    return(1);
}

//*************************************************************************

void control_loop()
{
    //************* 4P Cycle
    if(!heat_cycle && enable4p) {
        heat_cycle=1;      // enable the heating routine
        ADC.setDIO(_4p_heater,0);        //  turn on 4p heater  - this happens only once
        status_4p=1;
        heater_on_time=time(NULL);      // record 4p start time  - this happens only once
        begin_time=time(NULL);           // record time cycle started
        time_set=1;
        control_status="4 Pump Cycling";
        }

    if(heat_cycle && enable4p) {       // 4p is cycling
        if(time_set) {      // ie. heated to lower boundary
            if(scan_data.elem(last_point,_4p_chan) < set_temp[1]) {
                ADC.setDIO(_4p_heater,0);        // turn ON heater below hysterisis
                status_4p=1;
                }
            else if(scan_data.elem(last_point,_4p_chan) > set_temp[2]) {
                ADC.setDIO(_4p_heater,1);        // turn OFF heater above hysterisis
                status_4p=0;
                }

            if(difftime(time(NULL),heater_on_time) > delay_4p*60  ) {
                ADC.setDIO(_4p_heater,1);        // turn OFF heater
                status_4p=0;
                enable4p=0;                      // 4p cycle is done.
                enable3p=1;
                heat_cycle=0;
                time_set=0;
                control_status="4 P done, waiting...";
                }
            }
        }

//************* 3P Cycle
    if(scan_data.elem(last_point,stg_diode_chan) < set_temp[3] && !heat_cycle &&
          !enable4p && enable3p) {    // check stg diode heat when 4p cycle is done
        heat_cycle=1;      // enable the heating routine
        ADC.setDIO(_3p_heater,0);        //  turn on 3p heater  - this happens only once
        status_3p=1;
        heater_on_time=time(NULL);      // record 3p start time  - this happens only once
        time_set=1;
        control_status="3 Pump Cycling";
        }

    if(heat_cycle && enable3p) {       // 3p heater is ON        4p cycle is done
        if(time_set) {      // ie. heated to lower boundary
            if(scan_data.elem(last_point,_3p_chan) < set_temp[4]) {
                ADC.setDIO(_3p_heater,0);        // turn ON heater below hysterisis
                status_3p=1;
                }
            else if(scan_data.elem(last_point,_3p_chan) > set_temp[5]) {
                ADC.setDIO(_3p_heater,1);        // turn OFF heater above hysterisis
                status_3p=0;
    }

if(difftime(time(NULL),heater_on_time) > delay_3p*60 ||
        scan_data.elem(last_point,_4p_chan) < set_temp[9]) {
    ADC.setDIO(_3p_heater,1);        // turn OFF heater
    status_3p=0;
    enable3p=0;
    heat_cycle=0;
    heater_on_time=time(NULL);
       // record final push start time  - this happens only once
    time_set=1;
```

```
            final_push=1;                       // start final pushover
            control_status="Final Pushover";
            }
        }
    }

if(final_push==1 && time_set){
        if(scan_data.elem(last_point,_3p_chan) < set_temp[7]) {
            ADC.setDIO(_3p_heater,0);       // turn ON heater below hysterisis
            status_3p=1;
            }
        else if(scan_data.elem(last_point,_3p_chan) > set_temp[8]) {
            ADC.setDIO(_3p_heater,1);       // turn OFF heater above hysterisis
            status_3p=0;
            }
            if((difftime(time(NULL),heater_on_time) > delay_push*60 ||
                    scan_data.elem(last_point,_4p_chan) < set_temp[9]) &&
                    stg_diode_status==0) {
                ADC.setDIO(_3p_heater,1);       // turn OFF heater
                status_3p=0;
                enable3p=0;
                heat_cycle=0;
                time_set=0;
                final_push=0;                       // disable final pushover
                control_status="Final Cooldown";
                enable_kill=1;
                }
        }
    //************ check final cooling
    if(scan_data.elem(last_point,stg_diode_chan) < set_temp[6] &&
            (enable3p || final_push) && stg_diode_status==1) {
        ADC.setDIO(stg_diode,1);
            // turn OFF stg diode if in 3p cycle or final push, and stg < set temp
        stg_diode_status=0;
        }

    if(enable_kill && stg_diode_status==0 && scan_data.elem(last_point,stg_Ge_chan) <
            set_temp[10]) {
        ADC.setDIO(power_kill,1);
    // turn OFF main power after 3p cycle, final push, Ge < .34 and kill enabled
        control_status="Done. Power Killed.";
        stop_log=1;                         // stop cycle
        }
    if(difftime(time(NULL),begin_time) > total_time*60  ) {
        ADC.setDIO(_4p_heater,1);
        status_4p=0;
        ADC.setDIO(_3p_heater,1);
        status_3p=0;
        ADC.setDIO(stg_diode,1);
        stg_diode_status=0;
        ADC.setDIO(power_kill,1);
            // turn OFF main power if max time exceeded, no matter what.
        control_status="Time exceeded.";
        stop_log=1;
        }

    display_status();
}

void display_status()
{
    //************ display status of pumps and temperatures

    struct viewporttype viewinfo;
getviewsettings(&viewinfo);      // store previous viewport settings

setviewport(300,372,638,475,1);

setfillstyle(SOLID_FILL,BLACK);
bar(0,0,335,105);

settextstyle(SMALL_FONT, HORIZ_DIR, 4);
settextjustify(LEFT_TEXT,BOTTOM_TEXT);

    if(cycle_started) {
```

```
    setcolor(YELLOW);
    if(manual_cycle) control_status="Manual Cycle";
    sprintf(tempstr,"STATUS:   %s",control_status);
    outtextxy(10, 15, tempstr);
    }

setcolor(11);
outtextxy(10, 30, "Heat Switch");
outtextxy(10, 45, "4 Pump heater");
outtextxy(10, 60, "3 Pump heater");
outtextxy(10, 75, "Stage Diode");

if(heat_sw_status==CLOSED) {
    setcolor(RED);
    outtextxy(140, 30, "CLOSED");
    }
    else if(heat_sw_status==OPEN) {
        setcolor(LIGHTGREEN);
        outtextxy(140, 30, "OPEN");
        }

    if(status_4p==1) {
        setcolor(RED);
        outtextxy(140, 45, "ON");
        }
    else {
        setcolor(LIGHTGREEN);
        outtextxy(140, 45, "OFF");
        }

    if(status_3p==1) {
        setcolor(RED);
        outtextxy(140, 60, "ON");
        }
    else {
        setcolor(LIGHTGREEN);
        outtextxy(140, 60, "OFF");
        }

    if(stg_diode_status==1) {
        setcolor(RED);
        outtextxy(140, 75, "ON");
        }
    else {
        setcolor(LIGHTGREEN);
        outtextxy(140, 75, "OFF");
        }
setviewport(viewinfo.left,viewinfo.top,viewinfo.right,viewinfo.bottom,viewinfo.clip );
// restore previous viewport

}
```

The following text is the configuration file used to modify the of the automatic cycling program.

```
                configuration file for the AUTOCYCLER program.
                -end each comment block with an asterix
                -don't leave blank lines unless inside a comment
                -seperate numbers with a TAB

// cycle start delay (hours)*
11
// sample delay (seconds  typical minimum is 3)*
3
// minutes per window (max is 120)*
120
// maximum temperature*
60
// major  space(float),  #minor xticks(int), major ytick space(float), # minor
yticks(int)*
30  5   20  3
// major x grid, minor x grid, major y grid, minor y grid   0=disabled *
1   0   1   0
// channel colors (0,1,2,3)*
12  10  14  15
// temperature :  1) 4P chamber lower temp, 2) 4P chamber upper temp,
       3) 3P cycle start temp, 4) 3P chamber lower temp, 5) 3P chamber upper temp,
       6) temp to turn of Stg diode, 7) Final push lower temp,
       8) Final push  temp,  9) Final push kill 4p-temp,  10) Power kill Ge temp.
       NOTE: 3p and 4p never get below 4 K *
50  50.1    2.1 52  52.1    1.5 40  40.1    6   0.35
// 4P heater on-time,  3P heater on-time, Final pushover time, Max. total time
in MINUTES *
16  35  25  120
//  Current corrections:
3P diode current(10uA), 4P diode current(10uA), stage diode current(10uA),
Ge diode current(1uA), Ge diode current(10uA), Ge diode resistance offset,
diode voltage offset (mV) *
10  10  10  1   10  255 0
// gr100.dat (7 entries)          for Ge diode
temp    volt*
2   372
1.4 693
1   1444
0.8 2228
0.5 5863
0.4 10000
0.3 18850
// ifn146.dat  (74 entries)        for 4p and 3p
temp    volt*
300 0.573
290 0.597
190 0.808667
180 0.828667
170 0.849667
160 0.869
150 0.889
140 0.906
130 0.927
120 0.944
110 0.962667
100 0.978667
95  0.990333
90  0.998667
85  1.007
80  1.01567
75  1.02433
70  1.03233
65  1.041
60  1.05
55  1.05833
50  1.067
```

```
48  1.07
46  1.074
44  1.077
42  1.081
40  1.08333
38  1.087
36  1.09033
34  1.095
32  1.101
30  1.11033
29  1.11467
28  1.12167
27  1.13533
26  1.15733
25  1.19167
24  1.24167
23  1.29633
22  1.33467
21  1.36433
20  1.393
19.5    1.41
19  1.42933
18.5    1.44867
18  1.46667
17.5    1.48167
17  1.49567
16.5    1.50767
16  1.519
15.5    1.52867
15  1.53867
14.5    1.54767
14  1.55633
13.5    1.56433
13  1.57267
12.5    1.581
12  1.58967
11.5    1.59867
11  1.609
10.5    1.62
10  1.63233
9.5 1.64567
9   1.66067
8.5 1.67633
8   1.69467
7.5 1.718
7   1.74867
6.5 1.78533
6   1.823
5.5 1.85967
5   1.89533
4.5 1.92833
4   1.957
// dt500.dat  (96 entries)          for stage diode
temp    volt*
300 0.51892
290 0.54294
280 0.5669
270 0.5908
260 0.61465
250 0.63841
240 0.66208
230 0.68564
220 0.70908
210 0.73238
200 0.75554
190 0.77855
180 0.80138
170 0.82404
160 0.8465
150 0.86873
140 0.89072
130 0.91243
120 0.93383
110 0.95487
100 0.9755
```

95	0.98564
90	0.99565
85	1.00552
80	1.01525
75	1.02482
70	1.03425
65	1.04353
60	1.05267
55	1.0617
50	1.07053
48	1.07402
46	1.07748
44	1.08093
42	1.08436
40	1.08781
38	1.09131
36	1.0949
34	1.09864
32	1.10263
30	1.10702
29	1.10945
28	1.11212
27	1.11517
26	1.11896
25	1.12463
24	1.13598
23	1.15558
22	1.17705
21	1.19645
20	1.2144
19.5	1.22314
19	1.23184
18.5	1.24053
18	1.24928
17.5	1.2581
17	1.26702
16.5	1.27607
16	1.28527
15.5	1.29464
15	1.30422
14.5	1.31403
14	1.32412
13.5	1.33453
13	1.3453
12.5	1.35647
12	1.36809
11.5	1.38021
11	1.39287
10.5	1.40615
10	1.42013
9.5	1.43488
9	1.45048
8.5	1.467
8	1.48443
7.5	1.50272
7	1.52166
6.5	1.54097
6	1.56027
5.5	1.57928
5	1.59782
4.5	1.6157
4	1.63263
3.8	1.63905
3.6	1.64529
3.4	1.65134
3.2	1.65721
3	1.66292
2.8	1.66845
2.6	1.67376
2.4	1.6788
2.2	1.68352
2	1.68786
1.8	1.69177
1.6	1.69521
1.4	1.69812

6.3 Cosmic Ray Frequency Response

Analysis of the time decay of an interferogram spike caused by a cosmic ray event provides information about the frequency response of the bolometers. Results of this analysis were presented in Chapter 5. The IDL 5.0 code given below was written to perform a Fourier Transform on a group of recorded cosmic ray spikes, and plot the average frequency response for each detector. Figure 5.8 was produced by this program.

```
;*****************************************************************
PRO COSMIC_TIME_CONSTANT
;*****************************************************************
; PURPOSE: Reads in cosmic ray spikes from a set of interferograms, applies
;          a Fourier Transform, and plots the frequency response. Overplots
;          the measured chopped frequency response
;
; REQUIRED PARAMETERS    none
;
; VERSION 1.0     1.8.98 (BGG)
;*****************************************************************
    !p.multi=0
    SET_FIG
    ;indices for the various interferograms
    ;det1index=[1,2,3,4,6,7,8,9,11,15,16,18,19,21]        ;all hits
    ;det2index=[0,5,10,12,13,14,17,20,22]
    det1index=[1,2,3,4,6,7,8,9,11,21]                  ;good hits
    det2index=[5,10,13,14,20,22]
    check=0
    CD,'c:\idl\brad\cosmic rays'
    RESTORE, FILENAME = 'hits.var'
    RESTORE, 'lengths.var'
    hitindex=det1index

    L$Start:

    numhits=N_ELEMENTS(hitindex)
    hitlengths=INTARR(numhits)
    hitlengths[*]=lengths[hitindex]
    xcoords=FLTARR(numhits,MAX(hitlengths))
    ;get coordinates of spikes
    FOR i=0,numhits-1 DO BEGIN
        xcoords[i,0:(hitlengths[i])-1]=FINDGEN(hitlengths[i])*500/(hitlengths[i])
        xcoords[i,0]=.1
        END
    ;make a symmetric array for the FFT
    symdata=FLTARR(numhits,2*MAX(hitlengths))
    WINDOW,0
    FOR r=0,numhits-1 DO BEGIN
        i=hitindex[r]
        temp=FLTARR(lengths[i]-1)
        symdata[r,0:lengths[i]-1]=hits[i,0:lengths[i]-1]
        symdata[r,lengths[i]]=hits[i,lengths[i]-1]
        temp[*]=hits[i,1:lengths[i]-1]
        symdata[r,lengths[i]+1:(2*lengths[i])-1]=REVERSE(temp)
        IF r EQ 0 THEN PLOT,symdata[r,0:(2*lengths[i])-1]/ $
            MAX(symdata[r,0:  (2*lengths[i])-1]),/nodata,xrange =[0,2*MAX(hitlengths)]
        OPLOT,symdata[r,0:(2*lengths[i])-1]/MAX(symdata[r,0:(2*lengths[i])-1]),$
            color=(i MOD 9)+1
        ENDFOR
SAVE,,filename='temp.var'
;apply  to spikes
fftdata=symdata
fftdata[0,0:(2*hitlengths[0])-1]=ABS(FLOAT(FFT(symdata[0,0:(2*hitlengths[0])-1])))
fftdata[0,0:(2*hitlengths[0])-1]=fftdata[0,0:(2*hitlengths[0])-1]/fftdata[0,1]
interpfft=FLTARR(numhits,MAX(hitlengths))
xinterp=FINDGEN(MAX(hitlengths))*500/(MAX(hitlengths))
xinterp[0]=0.1
```

```
;plot the frequency response for all the spikes
WINDOW,1
PLOT,xcoords[0:hitlengths[0]-1],fftdata[0,0:(2*hitlengths[0])-1],/nodata,/xlog,$
      xrange=[0.1,1000],xstyle=1,/ylog,yrange=[.01,1.5],ystyle=1
FOR r=0,numhits-1 DO BEGIN
    i=hitindex[r]
    fftdata[r,0:(2*lengths[i])-1]=ABS(FLOAT(FFT(symdata[r,0:(2*lengths[i])-1])))
    interpfft[r,*]=INTERPOL(fftdata[r,0:lengths[i]-1],xcoords[r,0:lengths[i]-1],$
       xinterp)
    interpfft[r,*]=interpfft[r,*]/interpfft[r,1]
    OPLOT,xinterp,interpfft[r,*],color=i MOD 9 +1
    END
OPLOT,[0.1,1000],[.707,.707],color=9
;average the
avefft=FLTARR(MAX(hitlengths))
FOR i=0,MAX(hitlengths)-1 DO BEGIN
    av=MOMENT(ROTATE(interpfft[*,i],1))
    avefft[i]=av[0]
    END
avefft[0]=avefft[1]
avefft=avefft/avefft[0]
=avefft/( (1/(1+(xinterp/1280)^2)^.5) * (1/(1+(xinterp/2340)^2)^.5)*$
(1/(1+(xinterp/3000)^2)^.5) )
avefft=avefft/avefft[0]
;fit a 2-pole filter to the average freq. response
weights = REPLICATE(1.0,MAX(hitlengths)-1) ;Define a vector of weights.
A = [1,30.0]  ;Provide an initial guess of the function's parameters.
its=1
fit = CURVEFIT(xinterp[1:*],detectorcurve[1:*],weights,A,ITMAX=30,ITER=Its,tol=1e-9,$
    chisq=chi, SIGMA, FUNCTION_NAME='filter2')
PRINT
PRINT,'2 parameter Fit'
PRINT,'iterations',its
PRINT,'amplitude ',a[0]
PRINT,'f3dB ',a[1]
PRINT,'Chi Squared ',chi
PRINT,'sigma ',sigma
FOR =0,MAX(hitlengths)-1 DO BEGIN
    av=MOMENT(ROTATE(interpfft[*,i],1))
    avefft[i]=av[0]
    END
avefft[0]=A[0]
avefft=avefft/avefft[0]

detectorcurve=avefft/( (1/(1+(xinterp/1280)^2)^.5) * (1/(1+(xinterp/2340)^2)^.5)*$
(1/(1+(xinterp/3000)^2)^.5) )

;fit a single pole filter to the average freq. response
weights = REPLICATE(1.0,MAX(hitlengths))   ;Define a vector of weights.
B = [A[1]] ;Provide an initial guess of the function's parameters.
its=1
fit = CURVEFIT(xinterp,detectorcurve,weights,B,ITMAX=30,ITER=Its,tol=1e-9,$
      chisq=chi1, SIGMA1, FUNCTION_NAME='filter1')
PRINT
PRINT,'1 parameter Fit'
PRINT,'iterations',its
PRINT,'f3dB ',B
PRINT,'Chi Squared ',chi1
PRINT,'sigma ',sigma1

fitplot=FLTARR(1000)
xinthr=FINDGEN(1000)*500/(1000)
xinthr[0]=0.1
filter1,,B,fitplot1      ;1 pole fit
IF check EQ 0 THEN BEGIN ;trap detector 1
    WINDOW,3,xsize=500,ysize=500
    PLOT,xinterp,detectorcurve,/xlog,/ylog,xrange=[0.08,1000],xstyle=1,$
       yrange=[.01,1.5],ystyle=1,color=9,psym=6,symsize=.5
    OPLOT,xinthr,fitplot1,color=2
    xinterp_1=xinterp
    data_1=detectorcurve
    fitcurve_1=fitplot1
ENDIF ELSE BEGIN      ;trap detector 2
    WSET,3
    PLOT,,detectorcurve,/nodata,/noerase,/xlog,/ylog,xrange=[0.08,1000],$
```

```
        xstyle=1,yrange=[.01,1.5],ystyle=1,color=9
    OPLOT,xinterp,detectorcurve,color=2,psym=4,symsize=.5
    OPLOT,xinthr,fitplot1,color=3
    xinterp_2=xinterp
    data_2=detectorcurve
    fitcurve_2=fitplot1
ENDELSE
;plot -3dB line
OPLOT,[0.1,1000],[.707,.707],color=9
IF check EQ 0 THEN BEGIN     ;set trap for detector 2 and go back to start
    check=1
    hitindex=det2index
    GOTO, L$Start
    ENDIF
;plot the fit frequency response with
    XWINDOW,'finalplot',/Output,WXSIZE=600,WYSIZE=500,xinterp1=xinterp_1,$
        xinterp2=xinterp_2,data1=data_1,data2=data_2,fitcurve1=fitcurve_1,$
        fitcurve2=fitcurve_2,filename='c:\idl\brad\cosmic rays\freq_response.eps'
    L$END:
END

;*****************************
;plotting routine
;*****************************
PRO ,_extra=ex
    =FINDGEN(1000)*500/(1000)
    xinthr[0]=0.1
    set_fig
        PLOT,ex.xinterp1,ex.data1,/xlog,/ylog,yrange=[.01,1.5],ystyle=1,color=9,psym=6,$
            symsize=.5,xrange=[0.08,1000],xstyle=1,xtitle='Frequency (Hz)',$
            ytitle='Normalized Amplitude';,title='Frequency Response From Cosmic Ray Hits'
        OPLOT,xinthr,ex.fitcurve1,color=9
        OPLOT,ex.xinterp2,ex.data2,color=2,psym=5,symsize=.5
        OPLOT,xinthr,ex.fitcurve2,color=2
        OPLOT,[0.08,1000],[.707,.707],color=9

    ;draw legend
    LEG,psym=[-6,-5,-4,-2],linestyle=[0,0,0,0],scolor=[9,2,4,5],color=[9,2,4,5],$
        label=['Detector 1!Cf!I3dB!N-23.1 Hz','Detector 2!Cf!I3dB!N=40.9 Hz',$
        'Det 1 chopped!Cf!I3dB!N=52.2 Hz','Det 2 chopped!Cf!I3dB!N=108.6 Hz'],$
        position=[0.376929,0.247395,0.456392,0.561844];,box=[0,9,2,.02,.06,1]
    xl=.43
    xh=.693
    yl=.27
    yh=.616
    PLOTS,[xl,xl,xh,xh,xl],[yl,yh,yh,yl,yl],color=9,thick=1.5,/normal

    ;98 chopped data
    f=[2,4,7.5,11,14,18,21,25,31,35,42,52,58,62,68,75,81,86,90,103,109]
    d1=normalize([110,110,110,108,104,102,99,96,89,88,85,77,74,72,68,64,62,57,56,51,50])
    d2=normalize([110,110,110,110,110,110,110,110,108,107,106,102,99,97,91,90,89,85,$
           83,78,77])

    weights = REPLICATE(1.0,N_ELEMENTS(f)) ;Define a vector of weights.
    A = [50.0] ;Provide an initial guess of the function's parameters.
    its=1

    ;fit the detector 1 data
    fit = CURVEFIT(f,d1, weights, A, ITMAX=500,ITER=Its,tol=1e-5,$
        SIGMA, FUNCTION_NAME='filter1')

    PRINT,'det 1 chopped 3dB freq: ',a[0]
    PRINT,'sigma ',sigma
    PRINT,'iterations ',its
freq=FINDGEN(50)*10+1
OPLOT,freq,1/((1+(freq/a[0])^2)^.5),color=4
OPLOT,f,d1,psym=4,color=4,symsize=.5

;fit the detector 2 data
fit2 = CURVEFIT(f,d2, weights, A, ITMAX=500,ITER=Its,tol=1e-5,SIGMA,$
          FUNCTION_NAME='filter1')

PRINT,'det 2 chopped 3dB freq: ',a[0]
PRINT,'sigma ',sigma
PRINT,'iterations ',its
```

```
   OPLOT,freq,1/((1+(freq/a[0])^2)^.5),color=5;,linestyle=3
   OPLOT,f,d2,psym=2,color=5,symsize=.5
END

;*****************************
;single pole filter
;*****************************
PRO filter1, f, A, g, pder   ;   returns g(f) , uses only the f3db parameter
  g=1/((1+(f/a[0])^2)^.5)
  IF N_PARAMS() GE 4 THEN BEGIN ;If the procedure is called with four parameters,
                          ; calculate the partial derivatives.
    pder= [ f^2/((f^2+a[0]^2)^1.5)]
    ENDIF
END

;*****************************
;double pole filter
;*****************************
PRO filter2, f, A, g, pder   ;   returns g(f)
  g=a[0]/((1+(f/a[1])^2)^.5)
  IF N_PARAMS() GE 4 THEN BEGIN ;If the procedure is called with four parameters,
                          ; calculate the partial derivatives.
    pder= [ [1/((1+(f/a[1])^2)^.5)],[ a[0]*f^2/((f^2+a[1]^2)^1.5)] ]
    ENDIF
END
```

6.4 V-I Data Acquisition Software

Due to the time constraints during the observing runs, a quick method was needed for collecting the V-I data for the two detectors, six filters, and various loading conditions. C++ code was written to control the simple data acquisition module referenced in Chapter 5, and rapidly sample the detector voltage as a function of the applied bias voltage. During a reading, the bias voltage is varied by manually turning an adjustment potentiometer on the pre-amp/bias-supply unit. As the bias voltage increases, the program samples the detector voltage at a set frequency. In this way, the finely sampled V-I data is collected in 'real time', and the operator does not have to stop at each desired bias value to measure the corresponding detector voltage.

```
#include "c:\brad\source\includes\AD612.h"
// contains routines to read analog and R/W digital pins of the acqudat
#include <conio.h>
#include <stdio.h>
#include <stdlib.h>
#include <time.h>
#include <fstream.h>
#include <dos.h>
#include <math.h>
#include <except.h>
#include <mem.h>
#include <stdio.h>
#include <except.h>
#include <string.h>
#include <direct.h>
#include <fcntl.h>
#include <io.h>
#include <sys\stat.h>

float stepdelay=30;          // seconds between readings
```

```
AD612 ADC;                    // the acqudata module object routines
double current,voltage;
char* filename,filenm;
unsigned long h_res_time;     // current time in hundredths of seconds
struct dostime_t s,f;
int address;

void main()
{
    (filename,"V-I_curve.dat");      // default file prefix
    clrscr();
    address=ADC.find();
    if(address){
        cout<<"AD612 found at: ";
        printf("%x\n",address);
        }
    else {
        cout<<"AD612 NOT FOUND!";
        exit(0);
        }

    ADC.SetRange(4.096);      // set the returned value range to 0-4.096; true voltage
    int stop=0;

    cout<<"Put bias CURRENT into channel 0, put bias VOLTAGE into channel 1\n\n";
    cout<<"Filename = "<<filename;
    cout<<"Enter sample delay in seconds: ";
    cin>>stepdelay;
    _setcursortype(_NOCURSOR);

    ofstream outfile(filename);
        outfile<<"V-I data"<<endl;
        time_t filetime;
        time(&filetime);
        outfile<<"Started on "<<ctime(&filetime)<<endl;
        outfile<<stepdelay<<" seconds between samples\n"<<endl;
        outfile<<"current\tvoltage"<<endl;

    long num=0;

    while(!stop){
        _dos_gettime(&s);                  // high res timer  hundredths of seconds
        h_res_time=(s.hour*3600001)+(s.minute*6000)+(s.second*100)+(s.hsecond);
        current= ADC.ReadChan(0);
        voltage= ADC.ReadChan(1);
        cout<<"Sample #"<<num;
        outfile<<current<<"\t"<<voltage<<endl;
        gotoxy(10,10);
        cout<<"last I value:"<<current<<"\tlast V value:"<<voltage<<
            "    Hit CTRL-C to end          "<<endl;
        _dos_gettime(&f);
        while(long((f.hour*3600001) + (f.minute*6000) + (f.second*100) + f.hsecond) -
            long(h_res_time) < long(stepdelay*100)){
            delay(100);
            gotoxy(1,15);
            cout<<"port 0: "<<ADC.ReadChan(0)<<"    port 0: "<<ADC.ReadChan(1)<<
                  "    port 2: "<<ADC.ReadChan(2)<<"    port 3: "<<ADC.ReadChan(3)<<
                  "  "<<endl;
            _dos_gettime(&f);
            }
    num+=1;
        }
exit(0);
}
```

6.5 Theoretical V-I Fitting Routines

The IDL code given below was written to perform the theoretical modelling of the V-I curves as described in Section 5.4. In order to compute the least squares deviation of the theoretical fit, the raw data must be interpolated onto the same bias current grid as the theoretical curve. This detail proved to be a significant challenge due to the nature of the sampling performed by the software presented in the previous section. Since the bias supply circuit was not designed to provide a finely adjustable bias voltage, low quality potentiometers were used in its construction. As a result, when the pots are turned slowly, there is a certain amount of jitter produced in the bias voltage. This jitter in the bias voltage produces an irregularly sampled data set when sampled at a high frequency. In addition, the slight time delays involved in the sampling software, and the rise time of the bolometers, produce a jitter in the recorded detector voltage. These two factors produce an effective noise in the V-I data (although there is negligible noise in the steady state bias current or detector voltage). The interpolation routines included with the IDL 5.0 package cannot be used with this type of data set, so new routines were written to smooth the jitter in the data (without destroying any structure of the underlying V-I curve) and return a data set interpolated onto a given grid.

6.5.1 Bolometer Voltage Interpolation

The following routine returns the bolometer voltage interpolated onto an arbitrary bias current grid, allowing the bolometer voltages calculated from the theoretical equations to be compared directly with the corresponding measured values.

```
;*************************************************************************
FUNCTION v_bol,det,filter,temp,i_bias,gain=gn,year=yr,error=err,smooth=sm
;*************************************************************************
;Interpolates the bolometer voltage from the V-I curve
;for the specified filter, detector, temperature, and bias currents
;det - 0 or 1
;filter - 0 to 5
;temp - 0(amb) or 1(LN2)
;i_bias in nA
;gain=bias v gain. default=8.9
;NOTE: don't use high resolution i for values near zero.
;possible interpolation problems under 2 nA
;*************************************************************************
IF (NOT KEYWORD_SET(gn)) THEN BEGIN
    load_vi_parms,det,yr,g_o=g_o,tg=tg,r=r,n=n,t_o=t_o,gain=gain,loading=loading
    PRINT,'no gain in v_bol, using saved parameters: ',gain
    ENDIF ELSE gain=gn
IF (NOT KEYWORD_SET(yr)) THEN BEGIN
    PRINT,'set year keyword in v_bol'
    yr=97
    ENDIF
r_load=40e6
vi_pointers,vipointers,year=yr
vi_offsets,offsets,year=yr
```

```
IF yr EQ 98 THEN linearity=([1.002766,1.002155])[det] ELSE linearity=1.
IF KEYWORD_SET(err) THEN er=err ELSE er=0
vdet=(*vipointers[filter,det,temp])[*,1]+er
vbi=(*vipointers[filter,det,temp])[*,0]+er

v_bolom=(vdet-offsets[filter,det,temp])/gain ;volts
v_bias=vbi*2*linearity
i=(2*linearity*gain*vbi + offsets[filter,det,temp] - vdet) /(gain * r_load) *1e9

PTR_FREE,vipointers

;**********
;smooth data
;fit smooth spline to data
is=i(UNIQ(i, SORT(i)))
   vs=v_bolom(UNIQ(i, SORT(i)))

   IF NOT (KEYWORD_SET(sm)) THEN sm=20
   IF sm LT 3 THEN BEGIN
   PRINT,'No Smoothing in v_bol'
   ism=is
   vsm=vs
   ENDIF ELSE BEGIN
   ism=SMOOTH(is,sm)
   vsm=SMOOTH(vs,sm)
   ENDELSE
   vspline=SPL_INIT(ism,vsm)
   v_interp=SPL_INTERP(ism,vsm,vspline,i_bias)
   RETURN,v_interp
END
```

6.5.2 Bolometer Resistance Interpolation

The actual bolometer resistance is calculated by the following routine as a function of bias current.

```
;*************************************************************************
FUNCTION r_bol,det,filter,temp,i_bias,gain=gn,year=yr,error=err,smooth=sm
;*************************************************************************
;calculates the bolometer resistance (in Ohms) from the V-I curve
;for the specified filter, detector, temperature, and bias currents
;det = 0 or 1
;filter = 0 to 5
;temp = 0(amb) or 1(lN2)
;i_bias in nA
;gain is the bias voltage gain. default=8.9
;*************************************************************************
   IF (NOT KEYWORD_SET(gn)) THEN BEGIN
       load_vi_parms,det,yr,g_o=g_o,tg=tg,r=r,n=n,t_o=t_o,gain=gain,loading=loading
       PRINT,'no gain in r_bol, using saved parameters: ',gain
       ENDIF ELSE gain=gn
   IF (NOT KEYWORD_SET(yr)) THEN BEGIN
       PRINT,'set year keyword'
       yr=97
       ENDIF
   r_load=40e6
   vi_pointers,vipointers,year=yr
   vi_offsets,offsets,year=yr

   IF yr EQ 98 THEN linearity=([1.002766,1.002155])[det] ELSE linearity=1.
   IF KEYWORD_SET(err) THEN er=err ELSE er=0;
   vdet=(*vipointers[filter,det,temp])[*,1]+er
   vbi=(*vipointers[filter,det,temp])[*,0]+er
   offset=offsets[filter,det,temp]
   v_bolom=(vdet-offset)/gain ;volts
   v_bias=vbi*2*linearity
   i=(2*linearity*gain*vbi + offset - vdet) /(gain * r_load) *1e9

   PTR_FREE,vipointers
```

```
;***********
;smooth data
;fit smooth spline to data
is=i(UNIQ(i, SORT(i)))
vs=v_bolom(UNIQ(i, SORT(i)))

IF NOT (KEYWORD_SET(sm)) THEN sm=20
IF sm LT 3 THEN BEGIN
    PRINT,'No Smoothing in v_bol'
    ism=is
    vsm=vs
    ENDIF ELSE BEGIN
    ism=SMOOTH(is,sm)
    vsm=SMOOTH(vs,sm)
    ENDELSE
    vspline=SPL_INIT(ism,vsm)
    v_interp=SPL_INTERP(ism,vsm,vspline,i_bias)

    r_bol_int=v_interp/(i_bias*1e-9)    ;smoothed interpolated bolometer resistance at I

    RETURN,r_bol_int
END
```

6.5.3 Bolometer Impedance Interpolation

In order to calculate the responsivity, thermal conductivity, and noise equivalent power of the bolometers using the analysis presented in Chapter 5, the bolometer impedance must be calculated as a function of bias current.

```
;*****************************************************************************
FUNCTION z_bol,det,filter,temp,i_bias,final_smooth=zsm,gain=gn,year=yr,error=err,smooth=sm
;*****************************************************************************
;calculates the dynamic impedance (in V/A or Ohms) from the V-I curve
;for the specified filter, detector, temperature, and bias currents
;det = 0 or 1
;filter = 0 to 5
;temp = 0(amb) or 1(lN2)
;i_bias in nA
;smoothness is the final smoothing width of the z curve. Should be an odd
;number. 3 is good for ~100 element array
;gain= bias v gain. default=8.9
;*****************************************************************************
    IF (NOT KEYWORD_SET(gn)) THEN BEGIN
        load_vi_parms,det,yr,g_o=g_o,tg=tg,r=r,n=n,t_o=t_o,gain=gain,loading=loading
        PRINT,'no gain in z_bol, using saved parameters: ',gain
        ENDIF ELSE gain=gn
    IF (NOT KEYWORD_SET(yr)) THEN BEGIN
        PRINT,'set year keyword in z_bol'
        yr=97
        ENDIF
    r_load=40e6
    vi_pointers,vipointers,year=yr
    vi_offsets,offsets,year=yr

    IF yr EQ 98 THEN linearity=([1.002766,1.002155])[det] ELSE linearity=1.
    IF KEYWORD_SET(err) THEN er=err ELSE er=0
    vdet=(*vipointers[filter,det,temp])[*,1]+er
    vbi=(*vipointers[filter,det,temp])[*,0]+er

    v_bolom=(vdet-offsets[filter,det,temp])/gain ;volts
    v_bias=vbi*2*linearity
    i=(2*linearity*gain*vbi + offsets[filter,det,temp] - vdet) /(gain * r_load) *1e9

    PTR_FREE,vipointers

    ;***********
    ;smooth data
```

```
;fit smooth spline to data
is=i(UNIQ(i, SORT(i)))
vs=v_bolom(UNIQ(i, SORT(i)))

IF NOT (KEYWORD_SET(sm)) THEN sm=20
IF sm LT 3 THEN BEGIN
    PRINT,'No Smoothing in v_bol'
    ism=is
    vsm=vs
    ENDIF ELSE BEGIN
    ism=SMOOTH(is,sm)
    vsm=SMOOTH(vs,sm)
    ENDELSE

vspline=SPL_INIT(ism,vsm)
v_interp=SPL_INTERP(ism,vsm,vspline,i_bias)
    z=deriv(ism,vsm)
    zspline=SPL_INIT(ism,z)
    z_interp=SPL_INTERP(ism,z,zspline,i_bias)

    IF KEYWORD_SET(zsm) THEN BEGIN
        z_interp=SMOOTH(z_interp,zsm)
        ENDIF
    RETURN,z_interp*1e9
END
```

6.5.4 Bolometer Temperature Interpolation

The thermal conductance of the bolometers was defined in Chapter 2 as the derivative of the dissipated power with respect to temperature. Thus, in order to calculate this derivative, the temperature of the bolometers as a function of bias current, filter, and source temperature must be determined.

```
;*****************************************************************
FUNCTION t_bol,det,filter,temp,i_bias,_extra=ex
;*****************************************************************
;calculates the bolometer temperature from the V-I curve
;for the specified filter, detector, temperature, and bias currents
;det = 0 or 1
;filter = 0 to 5
;temp = 0(amb) or 1(lN2)
;i_bias in nA
;gain keyword sets the bias v gain. default=8.9
;year keyword = 97 or 98
;*****************************************************************

    r=r_bol(det,filter,temp,i_bias,_extra=ex)
    t=62.63116/(ALOG(r/7.5587969))^2
    RETURN,t
END
```

6.5.5 Least Squares Theoretical V-I Fitting Routine

Using the interpolation routines presented in the previous sections, we can generate theoretical V-I curves and compare them to the raw data interpolated onto the proper grid, as a function of G_0, T_0, and loading. The squared difference between the theoretical and experimental curves for each point in the 3-dimensional variable space is recorded. Once the entire variable space is mapped out, the values of the variables corresponding to the least squared difference between the curves can be determined.

```
PRO map_vi_3d
;*******************************************************
;   PURPOSE: used to find Go,T,loading
;   VERSION 1: 20/7/97    (BGG)
;*******************************************************
;setup constants for the theoretical curve
tg=62.631
n=.5
rr=7.5588
;define which experimental curve to fit
det=0
filter=0
temp=3
year=98

;these arrays determine the range for each variable
G_range=DOUBLE([24.e-9,25e-9])
t_range=DOUBLE([.29,.3])
l_range=DOUBLE([10e-11,20e-11])
;these values determine the number of steps for each variable
g_elements=DOUBLE(20)
t_elements=DOUBLE(20)
l_elements=DOUBLE(20)

;estimate running time
seconds=0.039*t_elements*l_elements*g_elements
cont='n'
pr='total time will be '+STRING(FLOOR(seconds/3600),format='(I3)')+' hours '+$
    STRING((seconds MOD 3600)/60,format='(f4.1)')+' minutes. Continue? (y/n)'
READ,cont,prompt=pr

IF ((cont NE 'y') AND (cont NE 'Y')) THEN STOP

time=SYSTIME()
dt_tm_inc,time,seconds,format='W$ d$ n$  h$:m$:s$'
PRINT,'Will finish on ',time

;setup an array to hold the deviation values
map=FLTARR(g_elements,t_elements,l_elements)

G_inc=(G_range[1]-G_range[0])/(g_elements-1)
t_inc=(t_range[1]-t_range[0])/(t_elements-1)
l_inc=(l_range[1]-l_range[0])/(l_elements-1)

G_o=G_range[0]-G_inc
time=SYSTIME(1)       ;get time for future runtime estimation

;find the best fit by brute force
FOR g_test=0,g_elements-1 DO BEGIN
    G_o=G_o+G_inc
    t_o=DOUBLE(t_range[0])-t_inc
    FOR t_test=0,t_elements-1 DO BEGIN
        t_o=t_o+t_inc
        loading=DOUBLE(l_range[0])-l_inc
        FOR l_test=0,l_elements-1 DO BEGIN
            loading=loading+l_inc
```

```
t=DINDGEN(400)/399*.6+t_o
t2=t/t_o
r2=rr*EXP((tg/t)^n)
g2=G_o*(t/t_o)*(t-t_o)-loading
i=(g2/r2)^.5 * 1e9
;take only meaningful points
ind=WHERE(FINITE(i) AND (i LE 90) AND (i GE 3) AND (g2 GT 0))
tmax=MAX(t[ind])
tmin=MIN(t[ind])
t=DINDGEN(400)/399*(tmax-tmin)+tmin
t2=t/t_o
r2=rr*EXP((tg/t)^n)
g2=G_o*(t/t_o)*(t-t_o)-loading
i=(g2/r2)^.5 * 1e9
v=(g2*r2)^.5
          v_raw=v_bol(det,filter,temp,i,year=year,gain=gain)
          map[g_test,t_test,l_test]=SQRT(TOTAL( ((v-v_raw)/(FLOAT(N_ELEMENTS(v))))^2 ))
        ENDFOR
    ENDFOR
ENDFOR

PRINT,(SYSTIME(1)-time)/(t_elements*l_elements*g_elements),' seconds per step'
g_scale=FINDGEN(g_elements)*G_inc+G_range[0]
t_scale=FINDGEN(t_elements)*t_inc+t_range[0]
l_scale=FINDGEN(l_elements)*l_inc+l_range[0]

;find the values that produce the best fit
l_ind=FLOOR((FLOOR(WHERE(map EQ MIN(map))/g_elements))/t_elements)
t_ind=(FLOOR(WHERE(map EQ MIN(map))/g_elements)) MOD t_elements
g_ind=WHERE(map EQ MIN(map)) MOD g_elements

PRINT,'minimum= ',map[g_ind,t_ind,l_ind]/1e-5
PRINT,'G_o: ',g_scale[g_ind]
PRINT,'+/- ',g_inc/2
PRINT,'T_o: ',t_scale[t_ind]
PRINT,'+/- ',t_inc/2
PRINT,'Loading: ',l_scale[l_ind]
PRINT,'+/- ',l_inc/2

;regenerate the best theoretical fit
WINDOW,2,xsize=500,ysize=500
       t_o=DOUBLE(t_scale[t_ind[0]])
       t=DINDGEN(4000)*.3/3999+t_o
       i=t
       G_o=DOUBLE(g_scale[g_ind[0]])
       loading=DOUBLE(l_scale[i_ind[0]])
       t2=t/t_o
       r2=rr*EXP((tg/t)^n)
       g2=G_o*(t/t_o)*(t-t_o)-loading
       i=(g2/r2)^.5 * 1e9
       ind=WHERE((i LE 90) AND (i GE 3))   ;take only meaningful values
       tmax=MAX(t[ind])
       t=DINDGEN(4000)/3999*(tmax-t_o)+t_o
       t2=t/t_o
       r2=rr*EXP((tg/t)^n)
       g2=G_o*(t/t_o)*(t-t_o)-loading
       i=(g2/r2)^.5 * 1e9
       v=(g2*r2)^.5
       v_raw=v_bol(det,filter,temp,i,year=year,gain=gain)

PLOT,i,v_raw,xrange=[0,100],yrange=[0,.1]
OPLOT,i,v,color=5
SAVE,map,g_scale,r_scale,l_scale,filename='map3d.var';save for future analysis
END
```

[1] Inprise Corporation, 100 Enterprise Way, Scotts Valley, California, 95066-3249, USA

[2] Research Systems Inc., 4990 Pearl East Circle, Boulder, Colorado, 80301, USA

[3] AD612 DAS module, Accu-Data, Suite C-178 297 Route 72 West, Manahawkin, New Jersey 08050-2890, USA.